



**UNIVERSIDADE DE BRASÍLIA
INSTITUTO DE GEOCIÊNCIAS
PROGRAMA DE PÓS-GRADUAÇÃO EM GEOLOGIA**

FACIOLOGIA, QUIMIOESTRATIGRAFIA E INTERAÇÃO FLUIDO-ROCHA EM CARBONATOS NEOPROTEROZOICOS DA FORMAÇÃO SALITRE NA REGIÃO DE IRECÊ, BAHIA

Dissertação de mestrado n° 462

Igor Augusto Pureza Taveira

**BRASÍLIA-DF
2020**



**UNIVERSIDADE DE BRASÍLIA
INSTITUTO DE GEOCIÊNCIAS
PROGRAMA DE PÓS-GRADUAÇÃO EM GEOLOGIA**

FACIOLOGIA, QUIMIOESTRATIGRAFIA E INTERAÇÃO FLUIDO-ROCHA EM CARBONATOS NEOPROTEROZOICOS DA FORMAÇÃO SALITRE NA REGIÃO DE IRECÊ, BAHIA

Igor Augusto Pureza Taveira

Orientadora

Profa. Dra. Lucieth Cruz Vieira

Comissão Examinadora

Profa. Dra. Anelize Manuela Bahniuk Rumbelsperger

Prof. Dr. Martino Giorgioni

**BRASÍLIA-DF
2020**

Ficha catalográfica elaborada automaticamente,
com os dados fornecidos pelo(a) autor(a)

TT232f Taveira, Igor Augusto Pureza
FACIOLOGIA, QUIMIOESTRATIGRAFIA E INTERAÇÃO FLUIDO-ROCHA
EM CARBONATOS NEOPROTEROZOICOS DA FORMAÇÃO SALITRE NA
REGIÃO DE IRECÉ, BAHIA / Igor Augusto Pureza Taveira;
orientador Lucieth Cruz Vieira. -- Brasília, 2020.
86 p.

Dissertação (Mestrado - Mestrado em Geologia) --
Universidade de Brasília, 2020.

1. Análise de Facies. 2. Carbonatos. 3. Neoproterozoico.
4. Geoquímica isotópica . 5. Interação fluido-rocha. I.
Vieira, Lucieth Cruz, orient. II. Título.

AGRADECIMENTOS

Aos meus pais: Sônia Gomes Pureza e Francisco Xavier Taveira, pelo apoio, pela compreensão e pelo empenho em todas as etapas da minha vida.

À minha noiva, Diana Vasconcelos, que compreendeu a importância desta etapa na minha vida e suportou minhas crises de ansiedade e ausências durante a realização da presente pesquisa, com seu apoio, tranquilizando-me sempre.

À minha professora orientadora, Dra. Lucieth Vieira, pela confiança e por acreditar no meu potencial para o desenvolvimento do estudo em questão. Meu profundo respeito!

Ao professor Dr. Roberto Ventura, pelo empenho, pela cobrança e pelas inúmeras discussões dos dados de grande valia.

Aos meus parceiros de pesquisa: Cleber Peralta e Diego Couto, pela amizade, prestatividade e por suportarem meus desabafos.

Ao professor Dr. Francisco Hilario Bezerra, pelo profissionalismo, pela prestatividade e pelo empenho para com todos do projeto.

Aos professores Dra. Paola Ferreira e Dr. Elton Dantas, pelo apoio na pesquisa.

À empresa Shell Brasil, pelo auxílio financeiro e financiamento da presente pesquisa via Projeto Porocarste 3D.

Aos bolsistas do Laboratório de Geocronologia do Instituto de Geociências da Universidade de Brasília (IG-UnB): Gabriel Moizinho, Túlio Gabriel, Cintia Stumpf, Rafael Grudka, Giovanna Del Rey e André Alvim, pelas riquíssimas discussões das tardes do laboratório, pelos trabalhos de campo, além dos momentos de cafés e risadas.

Às crianças moradoras do povoado Achado, Irecê, Bahia, pela alegria, pelo entusiasmo e companheirismo durante os dias de campo.

A Universidade Federal do Rio Grande do Norte (UFRN), por todo o suporte durante as campanhas de campo.

Ao Antônio, servidor da UFRN, pela prestatividade e agilidade em tudo resolver durante os trabalhos de campo.

Aos amigos que sempre estiveram comigo: Hygor Viana, Caio Neiva e Fábio Fleury.

Aos meus gatos: Galena e Pírita – “né, mãe!”.

O presente trabalho foi realizado com apoio da Coordenação de Aperfeiçoamento de Pessoal de Nível Superior – Brasil (CAPES) – Código de Financiamento 001

RESUMO

Neste trabalho são apresentados dados de faciologia, petrografia e geoquímica isotópica obtidos em carbonatos Neoproterozoicos da Formação Salitre em afloramento localizado no povoado Achado, localizado 5 km a leste da cidade de Irecê, Bahia. O objetivo principal foi verificar a relação entre as litofácies e a migração de fluidos utilizando dados de $\delta^{13}\text{C}$, $\delta^{18}\text{O}$ e $^{87}\text{Sr}/^{86}\text{Sr}$ dos carbonatos. O levantamento faciológico se deu em uma seção de exposição contínua, com níveis faciológicos bem preservados, resultando na confecção de uma coluna estratigráfica com espessura de 345 metros. As fácies identificadas foram agrupadas em três associações de fácies distribuídas em um sistema de rampa carbonática: rampa carbonática interna dominada por maré e microbialitos (FA1); rampa carbonática interna dominada por ondas (FA2); e, rampa carbonática média dominada por ondas de tempestade (FA3). Apesar da boa preservação das estruturas sedimentares, toda a sequência apresenta feições de deformação, tais como: brechas hidráulicas, veios, fraturas e falhas. Com base na litologia, nas feições sedimentares e nas variações isotópicas, a coluna foi dividida em três seções, a saber: 1) Basal; 2) Intermediária; e, 3) Superior. A seção inferior é caracterizada por calcários com valores de $\delta^{13}\text{C}$ entre -0.46‰ e +3.17‰ que reflete deposição quando da conexão da bacia com oceanos Neoproterozoicos. As seções média e superior são caracterizadas por dolomitos e apresentam valores de $\delta^{13}\text{C}$ variando de -3.41‰ a +13.69‰ representando deposição em bacia restrita. A evolução diagenética da sucessão é caracterizada por seis estágios diagenéticos distintos, sendo eles: diagênese marinha, autigênese, *reflux*, meteórica, soterramento e hidrotermal. As condições paleoambientais e diagenéticas foram fundamentais para o estabelecimento do fluxo de fluidos na sucessão estudada. Os dolomitos da seção média e superior são caracterizados por grandes ocorrências de veios, sugerindo um controle litológico sobre a distribuição de fraturas e falhas - tais estruturas foram os principais condutos para a migração de fluidos, que tiveram espalhamento lateral devido ao controle faciológico. Nos dolomitos, dois grupos de veios foram identificados e que representam diferentes fontes de fluidos. O primeiro é caracterizado por apresentar valores muito negativos de $\delta^{13}\text{C}$ (entre -8.99‰ e +0.61‰) e $\delta^{18}\text{O}$ (-4.24‰ a -9.29‰) e valores radiogênicos de $^{87}\text{Sr}/^{86}\text{Sr}$ (variando de 0.71056 a 0.73854), representando fluidos hidrotermais externos. O segundo grupo foi formado em sistema fechado como resultado da interação fluido-rocha devido aos mecanismos de dissolução por pressão - os valores semelhantes de $\delta^{13}\text{C}$ e $\delta^{18}\text{O}$ para os veios e a rocha encaixante suportam tal interpretação. O estudo multidisciplinar envolvendo a análise de fácies, diagênese e geoquímica isotópica permitiu identificar as prováveis fontes de fluidos que percolaram a bacia, bem como a assinatura isotópica que esses fluidos deixam ao interagir com a rocha encaixante. A identificação de zonas de percolação de fluidos em reservatórios

carbonáticos é de extrema importância, uma vez que estes podem causar modificações na qualidade dos reservatórios, principalmente em relação à porosidade e permeabilidade.

Palavras-chave: análise de fácies; carbonatos; Neoproterozoico; geoquímica isotópica; interação fluido-rocha.

ABSTRACT

In this work, we show our new data, including facies analysis, petrography and isotope geochemistry obtained in Neoproterozoic carbonates of the Salitre Formation, in an outcrop located in the Achado village, 5 km east of the city of Irecê, Bahia. The main objective was to verify the relationship between lithofacies and fluid-rock migration using $\delta^{13}\text{C}$ and $\delta^{18}\text{O}$ carbonate data. Facies analysis was carried out in a section of continuous exposure, with well-preserved facies layers, resulting in a stratigraphic column with 345m. The facies identified were grouped into three facies associations, distributed on a carbonate ramp system: (FA1) inner carbonate ramp dominated by tidal process and microbialites, (FA2) inner carbonate ramp dominated by waves and (FA3) mid carbonate ramp dominated by storm waves. Despite well-preserved sedimentary structures, the entire sequence presents deformation features, such as veins, fractures and faults. Based on lithology, sedimentary features and isotope variations, the column was divided into three sections, namely: 1) lower; 2) middle; and 3) upper. The lower section is characterized by limestones, where $\delta^{13}\text{C}$ ranges from -0.46‰ to +3.17, which reflects deposition when the basin was connected to the Neoproterozoic open ocean. The middle and upper sections are characterized by dolostones, and have $\delta^{13}\text{C}$ values ranging from -3.41‰ to +13.69‰, representing deposition in a restricted basin. The diagenetic evolution of the succession is characterized by six distinct diagenetic stages: marine, authigenic, reflux, meteoric, burial and hydrothermal. The paleoenvironmental and diagenetic conditions were fundamental to establish the fluid flow in the studied carbonate succession. The dolostones of the middle and upper sections are characterized by frequent occurrences of veins, which suggests a lithological control of the distribution of fractures and faults. Such structures were the main conduits for fluid migration, which presented lateral spread due to facies control. In the dolostones, two groups of veins were identified which represent different sources of fluids. The first one is characterized by very negative $\delta^{13}\text{C}$ (ranging from -8.99‰ to +0.61‰) and $\delta^{18}\text{O}$ (ranging from -4.24 ‰ to -9.29‰) values, and radiogenic $^{87}\text{Sr}/^{86}\text{Sr}$ values (ranging from 0.71056 to 0.73854), representing external hydrothermal fluids. The other group was formed in a closed system as a result of the fluid-rock interaction through a pressure-solution mechanism. Similar $\delta^{13}\text{C}$ and $\delta^{18}\text{O}$ values for veins and host rock support this interpretation. The multidisciplinary study involving facies analysis, diagenesis and isotope geochemistry allowed for the identification of the probable sources of fluids that percolated the basin, as well as of the isotopic changes in the host

rock due to fluid-rock interaction. The identification of fluid flow zones in carbonate reservoirs is extremely important, since such fluids may cause changes in the quality of the reservoirs, especially in relation to porosity and permeability.

Keywords: Facies analysis; carbonates; Neoproterozoic; isotope geochemistry; fluid-rock interaction.

SUMÁRIO

CAPÍTULO 1.....	13
1.1 INTRODUÇÃO	13
1.1.1 Objetivos da dissertação	14
1.1.2 Localização da área de estudo	15
1.1.3 Estrutura da dissertação.....	15
1.2 MATERIAIS E MÉTODOS	16
1.2.1 Trabalho de campo e amostragem.....	16
1.2.2 Análise petrográfica	16
1.2.3 Catodoluminescência	16
1.2.4 Geoquímica isotópica.....	17
1.3 CONTEXTO GEOLÓGICO	18
1.3.1 Supergrupo Espinhaço.....	20
1.3.2 Supergrupo São Francisco.....	22
1.3.2.1 Formação Bebedouro	22
1.3.2.2 Formação Salitre	24
1.3.3 Síntese da evolução tectônica.....	29
CAPÍTULO 2.....	30
2 ISOTOPE SIGNATURES AS FINGERPRINTS FOR FACIES AND FLUID-ROCK INTERACTIONS: IMPLICATIONS FOR CARBONATE RESERVOIR FLUID MIGRATION	30
2.1 INTRODUCTION.....	31
2.2 GEOLOGICAL BACKGROUND	32
2.3 MATERIAL AND METHODS	34
2.4 RESULTS	36
2.4.1 Facies and facies associations	36
2.4.2 Isotope geochemistry.....	46
2.4.2.1 C and O isotope signatures	46
2.4.2.2 Sr isotope	47

2.5	DISCUSSION	47
2.5.1	Depositional model	47
2.5.2	Diagenesis	51
2.5.3	Isotopic interpretation	54
2.5.3.1	Carbon and oxygen isotopes	54
2.5.3.2	Sr Isotopes.....	58
2.5.4	Fluid migration and fluid-rock interactions	59
2.6	CONCLUSION	63
2.7	ACKNOWLEDGEMENTS	64
3	REFERÊNCIAS BIBLIOGRÁFICAS.....	65

ANEXO A

ANEXO B

Índice de figura

Figura 1: mapa de localização da área de estudo.....	15
Figura 2: Mapa geológico do Cráton São Francisco, com indicação das bacias Neoproterozoicas e das faixas móveis que bordejam o Cráton (Figura extraída de Trindade et al. (2004). O retângulo indica a localização da bacia de Irecê	19
Figura 3: Mapa geológico simplificado do Aulacógeno do Paramirim. O retângulo vermelho indica a localização da bacia de Irecê (Figura modificada de Cruz e Alkmim, 2006).....	21
Figura 4: Coluna estratigráfica com as sequências do Supergrupo Espinhaço na região da Chapada Diamantina. Figura extraída de Guadagnin et al., (2015).....	23
Figura 5: Unidades informais definidas para a Formação Salitre na Bacia de Irecê. Figura adaptada a partir de Misi e Silva, (1996).	25
Figura 6: Unidades informais propostas para a Formação Salitre por Bomfim et al. (1985) e Pedreira et al. (1987). Figura adaptada a partir de Lagoero (1990) e extraída de Santana (2016).	26
Figura 7: Correlação das unidades definidas por Souza et al. 1993 com trabalhos anteriores. Figura adaptada de Souza et al. (1993).	28
Figure 1: Irecê fold and thrust belt geologic map and NS-oriented cross-section. Based on Alkmim (2004), Kuchenbecker et al. (2011) and Redivo et al. (2019). The Achado quarry (red star) is the focus of this study.....	34
Figure 2: Stratigraphic column of the Achado Quarry with $\delta^{13}\text{C}$, $\delta^{18}\text{O}$ and $^{87}\text{Sr}/^{86}\text{Sr}$ data from host rock samples. Stratigraphic division: LS, Lower section; MS, Middle section; US, Upper section. Carbonate classification: M, Mudstone; W, Wackstone; P, Packstone; G, Grainstone; F, Floastone; R, Rudstone; B, Boundstone; BF, Bafflestone; FR, Framestone; C, Crystalline.....	38
Figure 3: Facies found in Achado quarry. A) F1, flaser-bedded grainstone and lime mudstone; B) F3, laminated boundstone interbedded with laminated siliciclastic mudstone (F4); C) Laminated dolostone extraclast rich interbedded with cross-bedded dolo grainstone (F5); D) Facies F5 showing faults and fractures, near to the major sinistral transpressional fault; E) cross-bedded intraclast rich lime grainstone (F6); E) F7, cross-bedded dolo grainstone with dolo mudstone lenses.....	40
Figure 4: Diagenetic features A) Microcrystalline calcite replaced with planar-s dolomite; B) Nodules constituted of blocky calcite (BC) and length-slow quartz (LSQ) NP; C) Nodules constituted of blocky calcite(BC) and length-slow quartz (LSQ) NX; D) crenulated lamination in F3; E) detrital grains in F3 - SG = siliciclastic grains; F) F5, contact between extraclast-rich laminated dolostone interbedded with cross-bedded dolo grainstone - SG = siliciclastic grains;	

G) blocky calcite (BC) filling vug in F5. H) Ooids (Oo) and peloids replaced with blocky calcite in the core (F6).....	41
Figure 5: A) and B) F8, columnar stromatolites; C) F9, dome-shaped stromatolites); D) F10, rudstone; E) F11, Hummocky cross-stratified grainstone; F) Thrombolite, showing amoeboids, dark gray mesoclot separated by patches of light-colored dolo mudstones and sparry cement (F12).....	42
Figure 6: Diagenetic features: A) ooids with cortical layers, the mineralogy is dolomite; B) zoned dolomite (ZN) and planar-s dolomite (P-s dol) crystals; C) dolomicritic peloids partially recrystallized - red-stained minerals are block calcite; D) porosity filled by calcite. E) stylolite; F) Mesoclot (Ms) with dolomite isopachous bladed rim (IBR); G) PPL photomicrograph of saddle dolomite (SD), quartz (Qtz) and blocky calcite (BC); H) NX photomicrograph of saddle dolomite (SD), quartz (Qtz) and blocky calcite (BC).....	44
Figure 7: Main pore types found in our samples: A) intracrystalline porosity; B) vugs in red-stained blocky calcite; C) intercrystalline pores between dolomite crystals; D) vugs and intercrystalline pores between dolomite crystals.. ..	45
Figure 8: Isotope values for host rock and veins. The green and purple circles represent isotopic values of two groups of veins. The red dots in the green circle represent $\delta^{13}\text{C}$ and $\delta^{18}\text{O}$ values of group 1. The red dots in the purple circle represent $\delta^{13}\text{C}$ and $\delta^{18}\text{O}$ values of group 2.	48
Figure 9: A) Major sinistral transpressional fault with sharp boundary surface; B) Plug sample from sinistral transpressional fault showing the sharp contact between facies and their isotopic values, as well as isotopic values for vugs filled by latter diagenetic mineral phases; C) cataclasite rock that occurs in F7; D) plug sample of cataclasite showing isotopic values of veins and host rock; E) hydraulic breccia that occurs in F7. F) plug sample of hydraulic breccia showing $\delta^{13}\text{C}$, $\delta^{18}\text{O}$ and $^{87}\text{Sr}/^{86}\text{Sr}$ values for the host rock and veins - Sample CARB 0067; G) hydraulic breccia that occurs in facies F12; H) plug sample of hydraulic breccia in F12 showing isotopic values of veins and host rock.....	50
Figure 10: Depositional model for the Achado outcrop. FA1 is constituted of F1, F2, F3, F4 and F5, FA2 is composed of F6, F7, F8, F9 and F10. And FA3 is constituted of F11 and F12. High water mean (HWM) and Low Water Mean (LWM) mark the intertidal environment. Fair-weather base (FWB) marks the transition between the inner ramp and the mid-ramp.....	51
Figure 11: Simplified paragenetic sequence, in diagenetic phases, of the Achado outcrop.	52
Figure 12: A) cloudy-core and limpid-rim zoned dolomite (ZD) PPL (plane polarized light) photomicrograph from Facies F3; B) Cathodoluminescence image of zoned dolomite, showing the alternation between dull red, bright red and dull yellow luminescence - Facies F7; C) ooids replaced with planar-s dolomite PPL photomicrograph - Facies F7; D) Cathodoluminescence	

image of ooids, showing alternation between yellow, dull red and bright red luminescence - Facies F7; E) PPL photomicrograph of the hydraulic breccia, showing on the left the host rock (HR), composed mainly of planar-s dolomite, and on the right the vein filled with saddle dolomite (SD) - sample CARB 0067; F) Cathodoluminescence image of the hydraulic breccia shows the host rock, on the left, displaying dull luminescence, while, on the other hand, saddle dolomite on veins shows very bright red zoned luminescence, saddle dolomite occurs between dull luminescent crystals that composed the host rock - CARB 0067; G) PPL photomicrograph of the host rock clasts from hydraulic breccia that occur in Facies 7 - CARB 0067; H) Cathodoluminescence image of host rock clast from hydraulic breccia showing bright red luminescence saddle dolomite as a cement - CARB 0067.....57

Figure 13: Cross plot of the C and O data shown in Fig. 2: A) all three sections; B) lower section; C) middle section; D) upper section. LS = lower sections, MS = middle section, US = upper section.59

Figure 14: Block diagram showing the fault evolution and vein formation. 1) thrust fault formation (a) and veins of group 2 formed through pressure solution mechanisms (B). 2) Cataclasite formation (c) and fluid migration from the reactivation of basement structures (d). 3) Formation of the hydraulic breccia and group 1 veins due to the fluid migrated through basement structures (e).62

Índice de tabela

Table 1: Summary of facies, sedimentary structures, processes and facies association of the Salitre Formation in the Achado Quarry.37

Table 2: C, O, Sr-isotope ratio for host rock samples. More data in the supplementary material.49

Table 3: C, O, Sr-isotope ratio values for veins. More data in the supplementary material.49

CAPÍTULO 1

1.1 INTRODUÇÃO

A migração de fluidos em rochas carbonáticas está relacionada a uma complexa interação entre fácies, fraturas e falhas (Peacock, 2002; Agosta et al., 2010; Michie et al., 2014; Peacock et al., 2016; 2017; 2018). A predição do comportamento da migração de fluidos nesse tipo de rocha tem se tornado cada vez mais crítica, uma vez que os carbonatos são importantes reservatórios de água, petróleo e gás (Montaron, 2008). Em muitos exemplos, a migração de fluidos em carbonatos é controlada pela diagênese e tectônica - processos que se dão em diferentes estágios durante a evolução dessas rochas (Laubach et al., 2010). Os processos diagenéticos estão normalmente associados às condições mais rasas de soterramento, quando os sedimentos carbonáticos contêm muita água intersticial. Em condições de soterramento mais profundas, fluidos são expelidos por compressão e a permeabilidade tende a diminuir. Sob tais condições, os caminhos que os fluidos podem seguir são extremamente dependentes do arranjo de fraturas e, consequentemente, das propriedades geomecânicas controladas pela mineralogia e pelos processos químicos. (Bjorlykke et al., 1994).

A diagênese envolve a interação de rochas carbonáticas com fluidos de diferentes origens (marinho, meteórico, e hidrotermal), resultando em texturas secundárias e mudanças em suas propriedades petrofísicas (Mazzullo and Harris, 1992; Kaufman and Knoll, 1995; Moore, 2001; Frimmel, 2010). Durante a eodiagenese, a interação com água meteórica e com fluidos em zona de *mixing*, pode afetar significativamente a porosidade primária dessas rochas (Giles and Marshal, 1986). No decorrer da mesodiagênse, fluidos ácidos gerados por processos químicos dentro da bacia são os principais responsáveis pela dissolução e pelas reações de precipitação. Estes fluidos ácidos podem ser formados a partir da interação de H₂O-CO₂ (Giles and Marshal, 1986; Clayton, 1990; Biel et al., 2016), a partir da degradação da matéria orgânica (Giles and Marshal, 1986), por reações minerais em folhelhos (Bjorlykke, 1983; Giles and Marshall, 1986) e por redução termoquímica de sulfato (Machel et al., 1995; Machel, 2001; Jiang et al., 2018). Além desses processos, a porosidade pode ser modificada devido à dolomitização (Weyl, 1960; Chen et al., 1985; Wang et al., 2015).

Em carbonatos profundamente soterrados, falhas e fraturas são importantes condutos de fluidos, onde as propriedades geomecânicas são os principais controles da porosidade e permeabilidade (Bjorlykke et al., 1994). Como evidenciado em Becker e Gross (1996), Hanks et al. (1997), Underwood et al. (2003) e Cooke et al. (2006), a migração de fluidos relacionada às

juntas é melhor controlada pelo arranjo estratigráfico de sucessões sedimentares do que pela tectônica. Com base nessa constatação, a predição de migração de fluidos em seções carbonáticas dependerá de um estudo integrado, envolvendo as relações estratigráficas dessas rochas, sua evolução diagenética, bem como técnicas que possam traçar a interação fluido rocha.

Reconhecer os caminhos pelos quais os fluidos migraram em carbonatos antigos pode ser um desafio devido à sobreposição de processos registrados nessas rochas. Em muitos exemplos, a percolação de fluidos pode ser acompanhada por mudanças em parâmetros geoquímicos (como por exemplo $\delta^{18}\text{O}$, $\delta^{13}\text{C}$, e $^{87}\text{Sr}/^{86}\text{Sr}$) controlados via temperatura, composição primária das rochas e dos fluidos, razão fluido/rocha e se a interação fluido-rocha se deu em sistema aberto ou fechado (Banner e Hanson, 1990). Alguns estudos evidenciaram que em condições de soterramento mais rasas, a migração de fluidos causa pervasiva mudanças na composição isotópica de rochas carbonáticas (Moore, 1989; 2001; Choquette and James, 1990; Swart and Eberli, 2005). Por outro lado, a migração de fluidos em regimes tectônicos é fortemente controlada pelo sistema de falhas ativas (Pili et al., 2002), acarretando em localizadas mudanças isotópicas nos carbonatos. Assim, reconhecer a natureza da interação fluido-rocha e o momento desses eventos é importante para entender os principais controles na circulação atual de fluidos em sucessões carbonáticas profundas. Esse tipo de abordagem requer sucessões bem expostas, onde as relações entre as características diagenéticas e tectônicas podem ser bem estabelecidas.

Este é o caso do afloramento Achado, localizado na região Nordeste do Brasil, onde carbonatos Neoproterozoicos afloram continuamente por cerca de 345 metros. Estes carbonatos, verticalizados por processos tectônicos, apresentam uma complexa história diagenética e hidrotermal comparável com outras sucessões de mesma idade (Shields and Veizer, 2002; Halverson et al., 2005; Misi et al., 2007). Devido à complexa história diagenética e tectônica, essa área é o local ideal para investigação de estratégias e procedimentos para melhor entender a história do fluxo de fluidos em sistemas carbonáticos complexos. Neste trabalho, foi realizada uma investigação detalhada do afloramento Achado, incluindo análise faciológica, petrografia e amostragem para geoquímica isotópica ($\delta^{18}\text{O}$, $\delta^{13}\text{C}$ e $^{87}\text{Sr}/^{86}\text{Sr}$). Com base nesses dados, foram definidos os principais mecanismos para a migração de fluidos, tanto relacionados aos processos primários e diagenéticos quanto aos processos tectônicos.

1.1.1 Objetivos da dissertação

O objetivo central desta pesquisa foi compreender os processos e produtos relacionados à migração de fluidos em rochas carbonáticas da Formação Salitre, por meio do estudo de

isótopos, análise faciológica e petrografia. Para tanto a execução da pesquisa incluiu as seguintes metas:

- i. Determinar a composição isotópica de C, O e Sr dos carbonatos primários e carbonatos de veios e associados a processos diagenéticos;
- ii. Verificar se os fluidos são oriundos do próprio sistema carbonático ou se são fluidos externos;
- iii. Realizar análise faciológica e petrográfica das rochas e verificar as relações de interação com o fluido em função de mudança de fácies;
- iv. Fornecer informações referentes às condições paleoambientais e diagenéticas atuantes durante e após a formação dessas rochas; e
- v. Identificar os principais processos diagenéticos responsáveis pela formação e distribuição vertical da porosidade secundária.

1.1.2 Localização da área de estudo

A área de estudo está localizada no povoado do Achado, localizado no município de Irecê Bahia, que dista de Salvador 476 quilômetros e o acesso à mesma é feito pelas BR 324 e 116 e pela BA-052. O povoado do Achado está localizado a cinco quilômetros a leste da cidade de Irecê, nas margens da rodovia BA-052 (Figura 1). As coordenadas do povoado do Achado são (UTM 196713/8746108) zona 24 L.

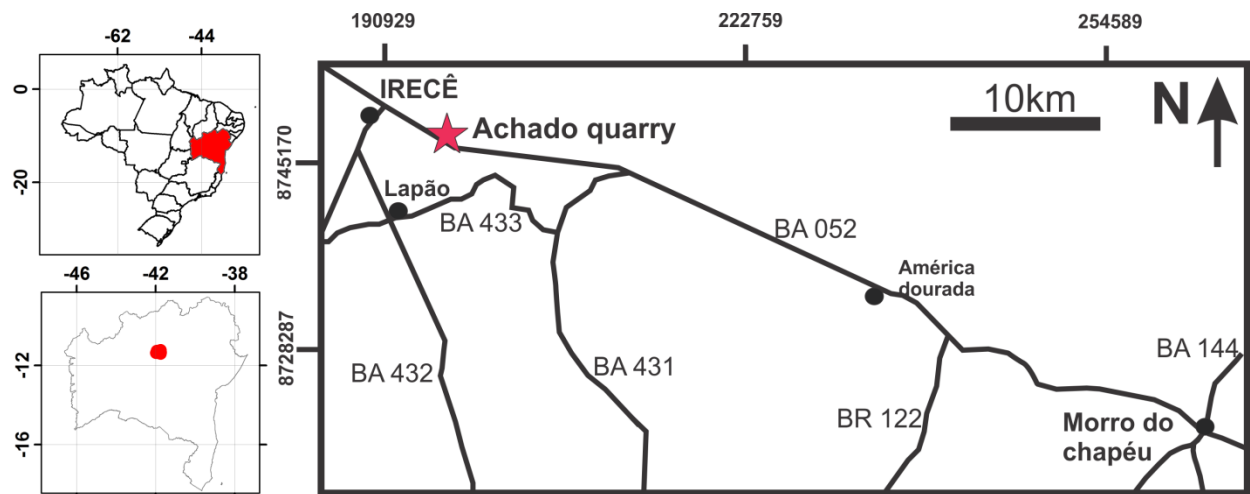


Figura 1: mapa de localização da área de estudo.

1.1.3 Estrutura da dissertação

Esta dissertação de mestrado está organizada em dois capítulos: Capítulo 1 - que inclui uma apresentação geral do objeto de estudo, principais objetivos do trabalho e contextualização da Formação Salitre na bacia de Irecê e; Capítulo II - onde são apresentados e discutidos os

resultados dessa pesquisa, redigido na forma de artigo científico e submetido no periódico *Marine and Petroleum Geology* intitulado: “*Isotope signature as fingerprints for facies and fluid-rock interactions: implications for carbonate reservoir fluid migration*”.

1.2 MATERIAIS E MÉTODOS

1.2.1 Trabalho de campo e amostragem

Após o trabalho de campo regional com reconhecimento das rochas carbonáticas da Formação Salitre na bacia, a sucessão aflorante no povoado do Achado foi escolhida como área de estudo, por apresentar uma sucessão continua e bem preservada. Os trabalhos de campo compreenderam o levantamento de sessões estratigráficas com análise faciológica detalhada e a coleta sistemática de amostras. A individualização de fácies foi feita com base nas características compostionais, texturais e estruturas sedimentares. Também foram mapeadas e descritas as principais feições tectônicas e de dissolução.

Durante as campanhas de campo foi realizada a amostragem de 42 *plugs* de rocha, utilizando uma plugadeira a gasolina, cujos testemunhos coletados apresentam 1,5 polegadas de diâmetro e comprimento variando entre 10 a 25 centímetros. Além dos *plugs*, foram coletadas 374 amostras de mão, com espaçamento amostral de um metro, com o objetivo de contemplar toda a área de trabalho. Os *plugs* foram serrados, sendo uma parte do material utilizada para a confecção de lâminas delgadas e, outra parte, para a amostragem pontual de rochas encaixantes e veios com micro *drill* para as análises de C, O e Sr. As amostras de mão foram pulverizadas para as análises de C, O e Sr.

1.2.2 Análise petrográfica

Amostras representativas de diferentes fácies foram selecionadas para a confecção de lâminas delgadas. O estudo petrográfico consistiu na descrição das feições deposicionais, diagenéticas e microestruturais. Esta análise permitiu重构 a história diagenética das rochas e sua relação com as microestruturas e modificações associadas aos fluídos. Um total de 56 lâminas delgadas foram analisadas ao microscópio óptico, utilizando-se técnicas e critérios tradicionais de petrografia.

1.2.3 Catodoluminescência

As feições diagenéticas não observadas durante a descrição petrográfica foram reveladas através da utilização da catodoluminescência. Foram analisadas 16 lâminas polidas, utilizando o

microscópio de luz polarizada Zeiss Axio Scope.A1, equipado com uma catodoluminescência ótica CITL mk5. As condições analíticas adotadas foram: vácuo entre 40 e 25 mTorr, amperagem de 224 mA; e, voltagem de 11Kv. As análises foram realizadas no centro UNESPetro da Universidade Estadual Paulista (Unesp), Campus Rio Claro.

1.2.4 Geoquímica isotópica

As razões isotópicas de C, O e Sr de rochas encaixantes, veios e preenchimentos foram determinadas a partir de amostragem contínua e com espaçamento variando de milimétrico a poucos centímetros, a fim de obter uma assinatura isotópica de alta resolução. Para tanto, foram coletadas 416 amostras incluindo *plugs* e amostras de mão. A pulverização das amostras para análise isotópica foi feita com a utilização de um micro drill, permitindo a retirada de material pontualmente (cerca de 300 µg). Todas as análises isotópicas foram realizadas no Laboratório de Geocronologia da Universidade de Brasília (IG-UnB).

Os dados isotópicos de C e O foram obtidos no Finnigan Gas Bench II, com a Opção-Carbonato, que conta com um *autosampler* com preparação de amostra assistida e interface com *loop* de injeção, com sistema de fluxo contínuo acoplado ao espectrômetro de massa Fanning DELTA plus Advantage. O Finnigan Gas Bench II, no modo carbonato, faz uso do princípio do banho ácido individual. Ácido fosfórico é adicionado em gotas em cada *vial* com amostra por um sistema de gotejamento completamente automatizado. O CO₂ gerado é passado lentamente através de um loop amostrador em um fluxo de hélio. Injeções repetitivas no loop por uma coluna isotérmica GC cria uma série de pulsos de CO₂ puro em He, o qual entra no IRMS via um *open split*. Esse sistema permite alcançar uma precisão de 0.08 ‰ para δ¹⁸O e de 0.06 ‰ para δ¹³C.

Para os estudos geoquímicos, diferenças relativas nas razões isotópicas são utilizadas para reportar abundâncias e variações de isótopos estáveis. Os valores obtidos para as razões isotópicas são reportados com a notação δ (valores de δ), que tem a seguinte definição:

$$\delta \equiv \left(\frac{R_X - R_{\text{padrão}}}{R_{\text{padrão}}} \right) \times 10^3$$

onde RX é a razão isotópica das amostras (¹³C/¹²C e ¹⁸O/¹⁶O) e R padrão é a razão correspondente a um padrão internacional de referência. O valor de δ é a diferença relativa na razão isotópica (sempre o isótopo pesado e raro versus o isótopo leve e mais abundante) entre a amostra e o padrão, em partes por milhão ou partes por mil (‰).

Para as análises de ⁸⁷Sr/⁸⁶Sr foram selecionadas 28 amostras de rochas encaixantes. A pulverização das amostras se deu evitando veios e preenchimentos secundários. Outras 6

amostras foram pulverizadas contemplando veios e preenchimentos. Um total de 50mg de carbonato pulverizado foi pesado e acondicionado em bêqueres de Teflon, sendo posteriormente atacados com ácido acético (0.5N) para dissolver somente a fração carbonática e evitar a contribuição de ^{87}Sr e Rb de minerais não carbonáticos presentes nas amostras. A razão $^{87}\text{Sr}/^{86}\text{Sr}$ foi obtida utilizando o espectrômetro de massa de termo-ionização (TIMS).

1.3 CONTEXTO GEOLÓGICO

A área de estudo está localizada na bacia de Irecê, inserida na Província Estrutural do São Francisco, que constitui uma das partes da Plataforma sul-americana (Almeida, 1977). Esta província está representada principalmente por uma região cratônica: o Cráton São Francisco (Almeida, 1967), que abrange principalmente os Estados de Minas Gerais e Bahia, e está circundada por faixas móveis neoproterozoicas, assim denominadas: Brasília, limite sul e oeste; Rio Preto, limite noroeste; Riacho do Pontal, limite norte; Sergipana, limite nordeste; e, faixa Araçuaí, limite sudeste (Figura 2) (Alkmin et al., 2001; Cruz e Alkmin, 2006).

O Cráton São Francisco, estável durante a orogenia brasileira, possui uma cobertura formada principalmente por rochas pouco deformadas do Mesoproterozoico, majoritariamente siliciclásticas, e Neoproterozoica, constituída principalmente por rochas carbonáticas, e por sucessões Fanerozoicas. As coberturas do cráton compreendem duas unidades morfotectônicas distintas: O aulacógeno do Paramirim ao norte e a bacia do São Francisco ao sul (Cruz e Alkmin, 2006). O embasamento do cráton, de idade Arquena-Paleoproterozoica, é constituído por rochas de médio a alto grau metamórfico e remanescentes de *Greenstone Belts*, sendo todos intrudidos por granitos, sienitos e, eventualmente, por plutons máficos ultramáficos, sendo essas intrusões Paleoproterozoicas. Quatro unidades geotectônicas compõe o embasamento do Cráton São Francisco, sendo elas o Bloco Gavião, Bloco Serrinha, Bloco Jequié e cinturão Itabuna-Salvador-Curaçá (Barbosa e Sabaté, 2004).

A configuração regional do Cráton São Francisco é definida pelos domínios leste e oeste, separados pelo domínio central, o Aulacógeno do Paramirim (Alkmim e Martins-Neto, 2012). O domínio central, onde está inserida a área de estudo, constitui um sistema de riftes paleo/mesoproterozóicos e neoproterozoicos parcialmente invertidos. As sucessões que preenchem o aulacógeno registram uma série de eventos relacionados à formação, modificação e inversão da bacia, bem como aos eventos climáticos, que ocorreram entre os períodos Estateriano e Ediacarano do Éon Proterozoico.

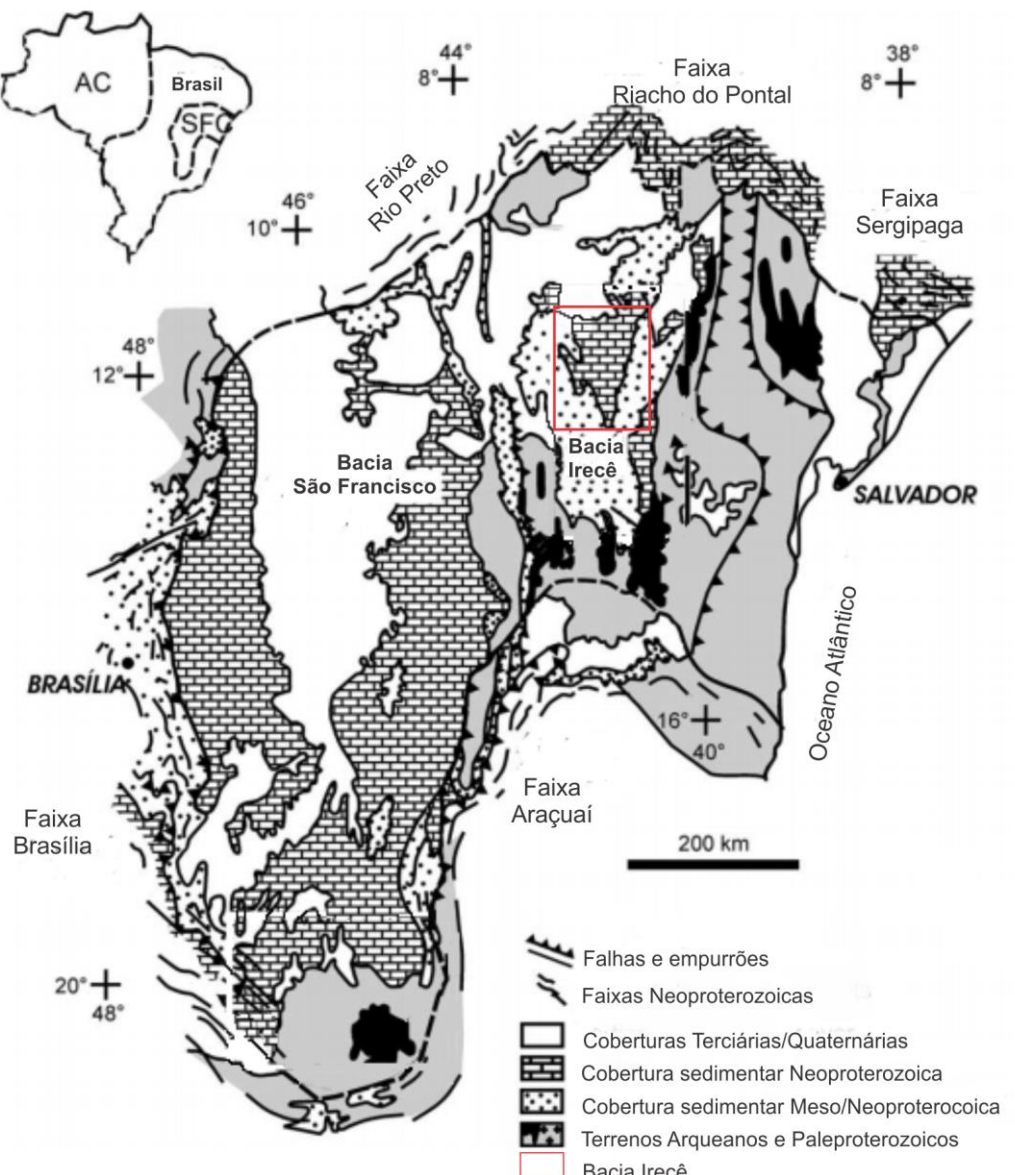


Figura 2: Mapa geológico do Cráton São Francisco, com indicação das bacias Neoproterozoicas e das faixas móveis que bordejam o Cráton (Figura extraída de Trindade et al. (2004). O retângulo indica a localização da bacia de Irecê

O Aulacógeno do Paramirim hospeda e expõe toda a seção da cobertura Pré-Cambriana do Cráton (unidades mais jovens que 1.8 Ga), que compreende duas unidades litoestratigráficas maiores, Os Supergrupos Espinhaço e São Francisco, que compreendem rochas metassedimentares e vulcânicas, depositadas entre o final do Paleoproterozoico e Neoproterozoico (Figura 3). (Schobbenhaus, 1996; Cruz e Alkmim, 2006).

O Aulacógeno Paramirim, localizado no estado da Bahia, compreende a serra do Espinhaço Setentrional, os vales do rio Paramirim e São Francisco, bem como um largo platô conhecido como Chapada Diamantina. Há uma notável diferenciação das fácies entre as unidades que preenchem o aulacógeno ocorrendo na serra do Espinhaço Setentrional, a oeste, e a Chapada Diamantina, a leste. Estas regiões estão separadas pelo vale do rio Paramirim que expõe o bloco do embasamento homônimo. O embasamento Paramirim atuou como um grande *horst*

nos estágios iniciais de evolução do aulacógeno. Sendo assim, duas bacias quase independentes foram individualizadas no final do Proterozoico, e permanecendo assim até o final do Neoproterozoico (Schobbenhaus, 1996; Cruz e Alkmim, 2006; Alkmim e Martins-Neto, 2012; Cruz e Alkmim, 2017).

A porção mais intensamente deformada do aulacógeno corresponde ao corredor do Paramirim, que constitui uma zona de 70-150 km de largura com aproximadamente 500 km de comprimento, e que possui uma direção NNW, delimitada pela Falha de Santo Onofre, a oeste, e pelo lineamento João Correia – Barra do Mendes, a leste. Este corredor engloba tanto o embasamento como as unidades de cobertura e consiste em uma deformação endodérmica. São comuns falhas, inversas e de empurrão, assim como dobras com orientação NNW e vergência para ENE (Cruz e Alkmim, 2006). A área de estudo da presente pesquisa tem sua localização a leste desse corredor (Figura 3).

1.3.1 Supergrupo Espinhaço

Na região da Chapada Diamantina, o Supergrupo Espinhaço apresenta uma sucessão estratigráfica de aproximadamente 5000 metros de espessura, subdivididos em três grupos; Rio dos Remédios, Paraguaçu e Chapada Diamantina, que correspondem a uma sequência dominante siliciclástica, depositadas entre 1.8 e 0.9 Ga (Cruz e Alkmim, 2017). Estas unidades estratigráficas foram divididas em três sequências intracratônicas de primeira ordem por Guadagnin et al. (2015), sendo elas a Sequência Estateriana (Espinhaço Inferior), Sequência Calimiana (Espinhaço intermediário) e Sequência Esteniana-Toniana inferior (Espinhaço Superior) (Figura 4).

Sequência Estateriana (1,8 -1,68 Ga; Espinhaço inferior)

A sequência Estateriana está representada na região da Chapada de Diamantina pelo Grupo Rio dos Remédios (Schobbenhaus e Kaul, 1971; Teixeira, 2005; Loureiro et al., 2009; Guimarães et al., 2012). Este grupo está subdividido em três Formações, Novo Horizonte, Lagoa de Dentro e Formação Oricuri do Ouro (Guimarães et al., 2008; Guimarães et al., 2012), que constituem em uma sucessão de 2000 metros de espessura composta por rochas vulcânicas ácidas, depósitos lacustres e fluviais, respectivamente. Dados geocronológicos obtidos nas rochas vulcânicas ácidas da Formação Novo Horizonte fornecem uma idade de cristalização de 1750 Ma (Schobbenhaus et al., 1994; Babinski et al., 1994).

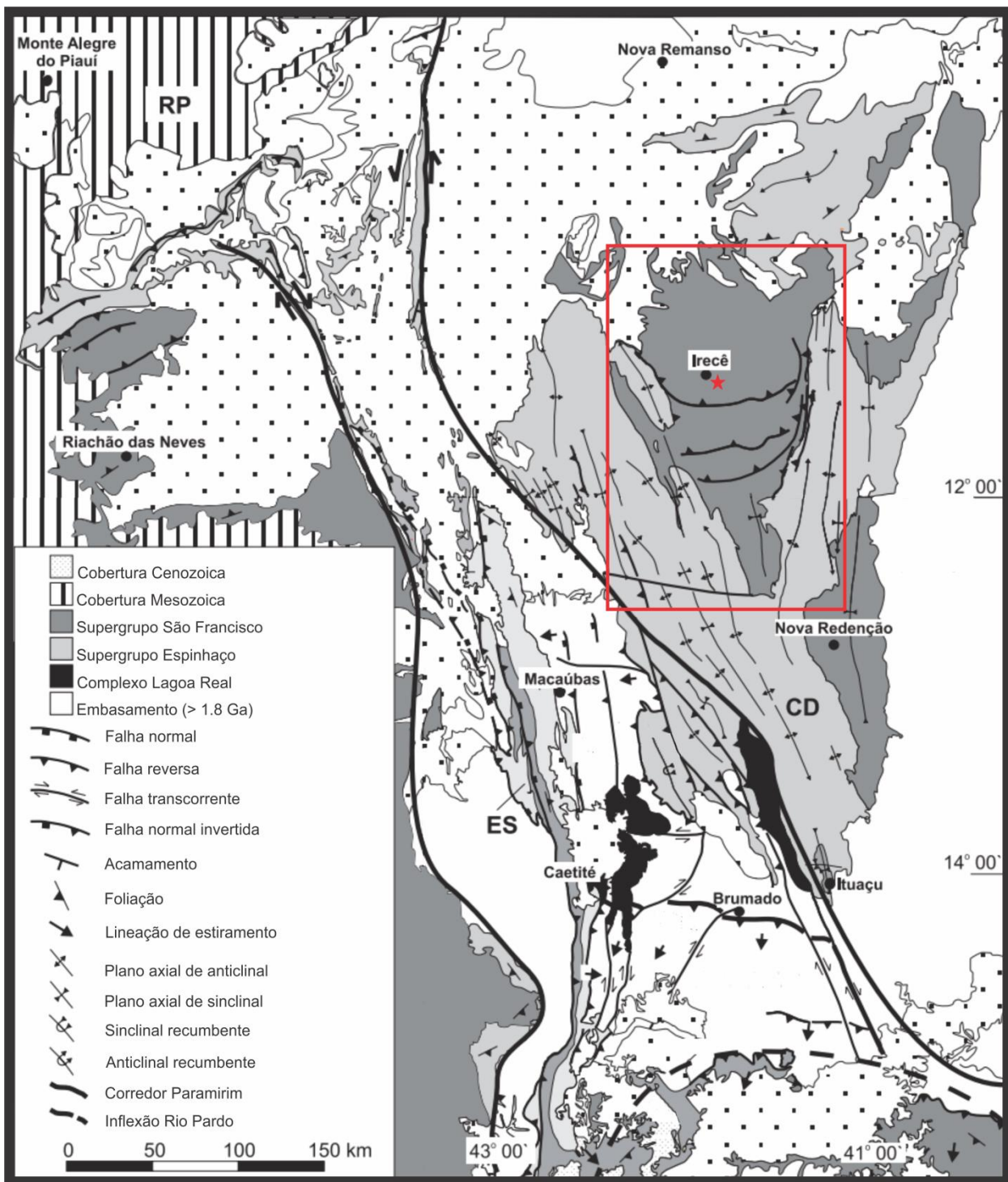


Figura 3: Mapa geológico simplificado do Aulacógeno do Paramirim. O retângulo vermelho indica a localização da bacia de Irecê (Figura modificada de Cruz e Alkmim, 2006).

Sequência Calimiana (1,60 – 1.38Ga; Espinhaço intermediário)

As unidades estratigráficas que compõe o Espinhaço intermediário foram depositadas entre 1.60 e 1.38 Ga em uma bacia *rift-sag*, que constituem o Grupo Paraguaçu e a Formação Tombador (Grupo Chapada Diamantina). O Grupo Paraguaçu é constituído por depósitos aluvio-fluviais e eólicos da Formação Mangabeira, bem como por sedimentos marinhos rasos e deltaicos da Formação Açuá (Guimarães et al., 2005). Enxames de diques máficos toleíticos

estão intrudidos na porção basal da Formação Mangabeira, cuja idade de cristalização consiste em 1515 ± 22 Ma (Babinski et al., 1999) e 1501 ± 9 Ma (Silveira et al., 2013). Tal intrusão define a idade mínima de deposição desta unidade.

A Formação Tombador compreende depósitos fluviais entrelaçados a marinhos rasos, arenitos depositados sob influência de maré, contendo localmente lentes e camadas de conglomerados diamantíferos (Magalhães et al., 2014; 2016). Uma discordância angular separa a Formação Tombador da Formação Açuá. A Formação Tombador possui uma idade de 1436 ± 26 Ma obtidas em rochas vulcanoclásticas e representa uma fase *sag* da bacia (Guadagnin et al., 2015).

Sequência Esteniana-Toniana inferior (1.2-0.9 Ga; Espinhaço Superior)

A Sequência Esteniana-Toniana inferior compreende as Formações Caboclo e Morro do Chapéu. A Formação Caboclo é constituída por arenitos e pelitos, com conglomerados e carbonatos subordinados, interpretados como depósitos flúvio-estuarinos, que gradam, em direção ao topo, para depósitos marinhos rasos. A Formação Morro do Chapéu é limitada na base por uma discordância regional, sendo constituída por arenitos e pelitos flúvio-estuarinos com intercalação de depósitos eólicos (Dominguez, 1993; Loureiro et al., 2009).

1.3.2 Supergrupo São Francisco

Na região de estudo, o Supergrupo São Francisco compreende ao Grupo Una, subdividido nas formações Bebedouro e Salitre. O Grupo Una está depositado sobre uma discordância de caráter regional sobre as rochas do embasamento do Cráton e rochas do Supergrupo Espinhaço.

1.3.2.1 Formação Bebedouro

A Formação Bebedouro compreende a base do Grupo Una, consistindo em uma sucessão glaciogênica Neoproterozoica separada das unidades mais antigas por uma discordância regional (Pedreira et al., 1975; Misi e Souto, 1975; Pedreira, 1997). Essa sequência glaciogênica é composta por diamictitos, pelitos e arenitos com uma variedade de litofácies agrupadas em quatro associações de fácies (Guimarães et al., 2011). Essa formação é correlacionada com a Formação Jequitaí e o Grupo Macaúbas (Alkmim e Martins-Neto, 2012) e está sobreposta por carbonatos platformais da Formação Salitre (Guimarães et al., 2011).

Os diamictitos apresentam clastos angulares, variando de grânulo a bloco, cuja composição inclui granitos, gnaisses, pegmatitos, xistos, filitos, máficas e ultrabásicas, vulcânicas, calcilicásticas, quartzitos, arenitos e *cherts*. Superfícies facetadas e polidas são comuns e há

ocorrências de clastos estriados (Guimarães, 1996). A matriz é composta por grauvacas, arenitos, arcóseos e argilitos (Guimarães, 1996).

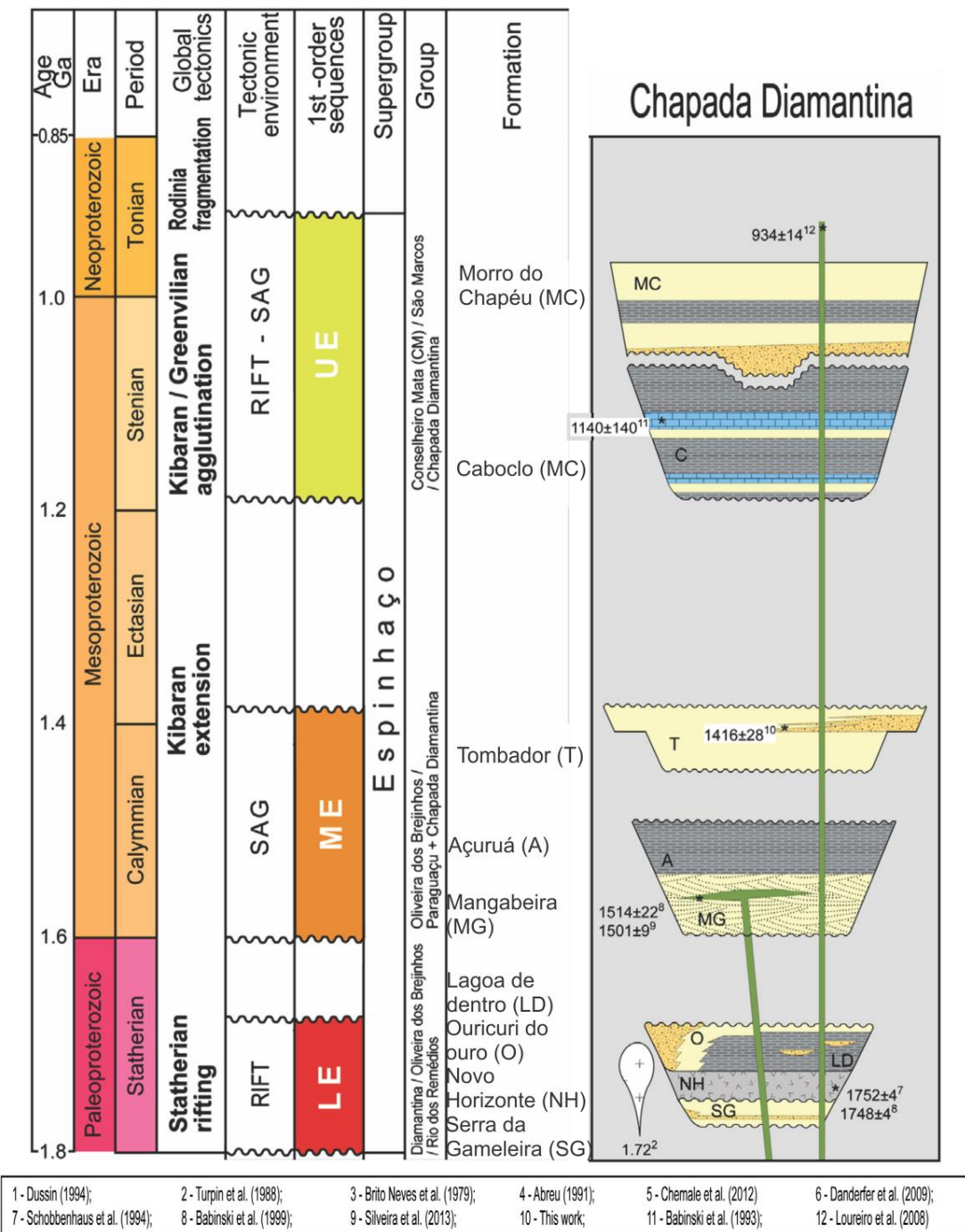


Figura 4: Coluna estratigráfica com as sequências do Supergrupo Espinhaço na região da Chapada Diamantina. Figura extraída de Guadagnin et al., (2015).

Os arenitos da Formação Bebedouro são litotipos de ocorrência subordinada, e inclui arcóseos marrons e esverdeados, grauvacas, arenito lítico e quartzo-arenito. Normalmente, os arenitos ocorrem intercalados com os diamictitos e com os pelitos. Os pelitos apresentam-se laminados e maciços e, em alguns casos, são relatados *dropstones* (Guimarães, 1996).

As litofácies encontradas na Formação Bebedouro são interpretadas como sendo formadas por mecanismos de fluxos de detritos, correntes de turbidez, *ice-rafting* e suspensão, sendo que, localmente, há evidências de retrabalhamento dos sedimentos por processos eólicos. As fácies identificadas na Formação são agrupadas em quatro associações de fácies, segundo Guimarães (1996), depositadas em ambiente glacio-marinho proximal. Datações de cristais de zircão detritico da matriz dos diamictitos de cerca de 850 Ma indicam a idade máxima de deposição (Figueiredo, 2008).

1.3.2.2 Formação Salitre

A Formação Salitre consiste em uma sequência predominantemente carbonática, disposta em discordância sobre os diamictitos da Formação Bebedouro e sobre os metassedimentos siliciclásticos e Mesoproterozoicos do Grupo Chapada Diamantina, com a sedimentação iniciando durante a transgressão de um mar epicontinental sobre o Cráton São Francisco (Misi e Kyle, 1994). É constituída por rochas carbonáticas, calcíticas e dolomíticas, com pequenas intercalações de rochas terrígenas, tendo como principais litotipos calcilutilos, calcissiltitos, dolo/calcarenitos, além de rochas bioconstruídas (Misi e Veizer, 1998).

São propostas duas classificações para a referida Formação, a saber: 1) A partir dos trabalhos de Misi (1979), Misi e Kyle (1994) e Misi e Silva (1996) (Figura 5), onde as unidades informais foram nomeadas por letras, C, B, B1, A e A1; e, 2) A partir do trabalho de Bonfim et al. (1985), onde as unidades são assim designadas: Nova América, Gabriel, Jussara e Irecê (Figura 6). A seguir têm-se a descrição das unidades proposta em cada classificação.

Unidade C

Constituída por dolomitos argilosos depositados sobre diamictitos da Formação Bebedouro. Eventualmente, há presença de laminações microbiais, estromatólitos e gretas de ressecamento, sobretudo na base; no topo passa gradativamente para calcários cinza-claros e laminados da unidade B (Torquato e Misi, 1977).

Unidade B

Composta por calcários cinzas laminados que gradam para o topo para camadas de dolomitos. Além disso, é caracterizada por uma sucessão rítmica de camadas centimétricas de calcário ou calcário dolomítico e argilito (Misi e Veizer, 1998).

Unidade B1

Consiste em dolomitos silticos avermelhados a cinza, associados com estromatólitos colunares ou laminares, localmente ricos em fosfato, calcários dolomíticos com laminação plano-paralela e lentes de calcarenito oolítico cinza escuro. Esta unidade contém as principais ocorrências de Pb-Zn e fosfato da Bacia. São também observadas estruturas sedimentares, tais

como estratificação cruzada e *ripples*, que indicam sedimentação em alta energia. Outras estruturas sedimentares como tepee, pseudomorfos de evaporitos e brechas lamelares estão presentes e sugerem exposição subaérea em clima árido (Misi e Kyle, 1994; Misi e Veizer, 1998). As unidades B e B1 representam uma sequência de raseamento para o topo (*Shallowing upward sequence*).

Unidade A

A presente Unidade encontra-se exposta na borda oeste da Bacia de Irecê, sendo constituída por uma intercalação de calcário argiloso, argilito e siltito, e, localmente, por calcarenitos. Ela foi depositada em águas relativamente profundas, marcando o início de um novo ciclo transgressivo-regressivo.

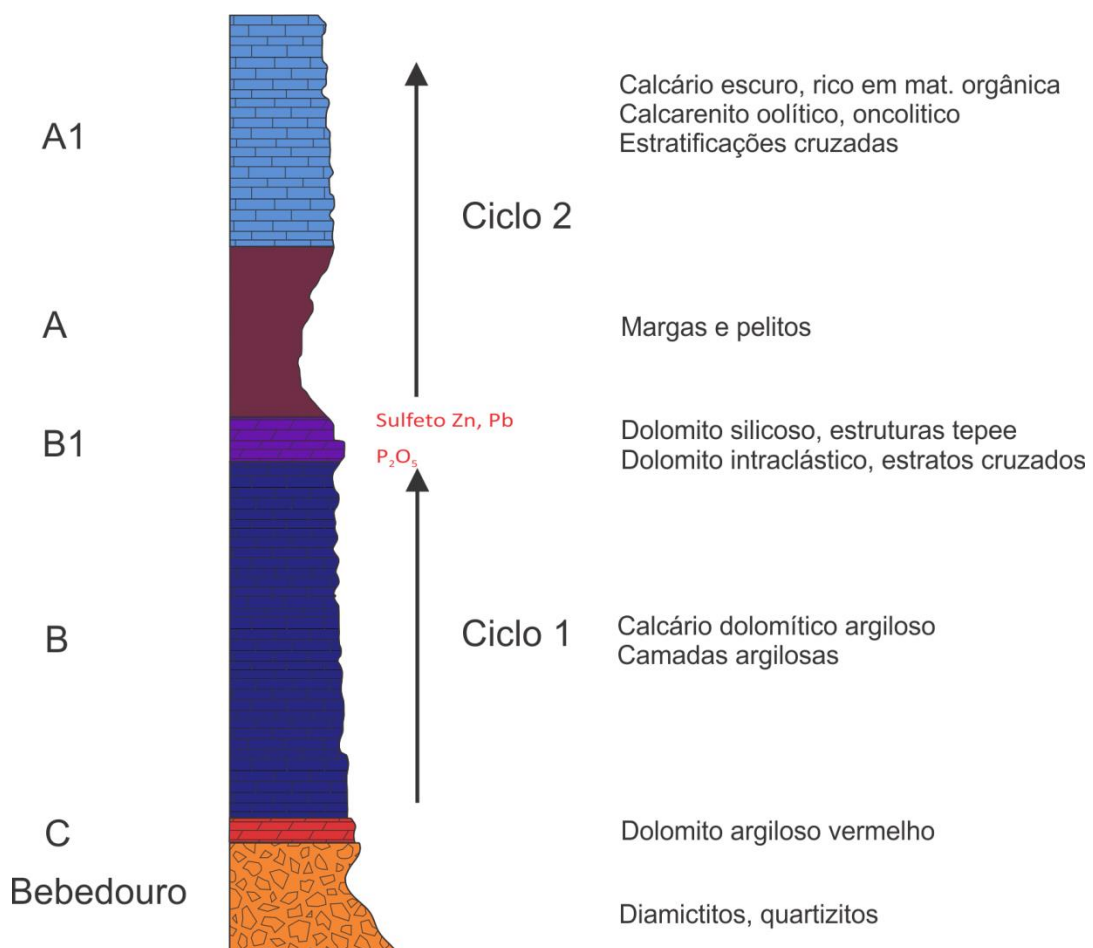


Figura 5: Unidades informais definidas para a Formação Salitre na Bacia de Irecê. Figura adaptada a partir de Misi e Silva, (1996).

Unidade A1

Esta unidade é caracterizada por calcários oolíticos e pisolíticos, pretos, maciços, ricos em matéria orgânica. Apresentam estratificações cruzadas e níveis ricos em intraclastos são comuns e interpretados como produtos de processos verificados em ambiente de água rasa com alta energia.

Pelo menos dois ciclos sedimentares maiores podem ser identificados na Formação Salitre (Misi et al., 2005; 2007). O ciclo 1 inicia na base da Formação, com a deposição das unidades C e B, e termina nos dolomitos com estruturas tepee (unidade B1) que representa a superfície de exposição de uma típica sequência de *Shallowing-upward*. O Ciclo 2 inicia-se com um evento transgressivo, representado por margas e folhelhos (Unidade A), imediatamente acima das fácies dolomíticas da unidade B1, passando para calcários pretos oolíticos e pisolíticos com estratificação cruzada, indicando sedimentação em alta energia (Unidade A1) (Figura 5).

A partir do trabalho de mapeamento geológico realizado por Bonfim et al. (1985) em escala 1:60000 na região do município de Irecê, é proposta uma nova subdivisão litoestratigráfica para a Formação Salitre em unidades informais. O mapeamento geológico realizado por Pedreira et al. (1987) em uma região diferente da bacia divide a Formação Salitre em quatro unidades – denominadas da base para o topo (Nova América, Gabriel, Jussara e Irecê). Souza et al. (1993) revisaram a litoestratigrafia e subdividiram a Formação Salitre em unidades e subunidades informais anteriormente propostas por Bonfim et al. (1985), que serão descritas a seguir (Figura 6).

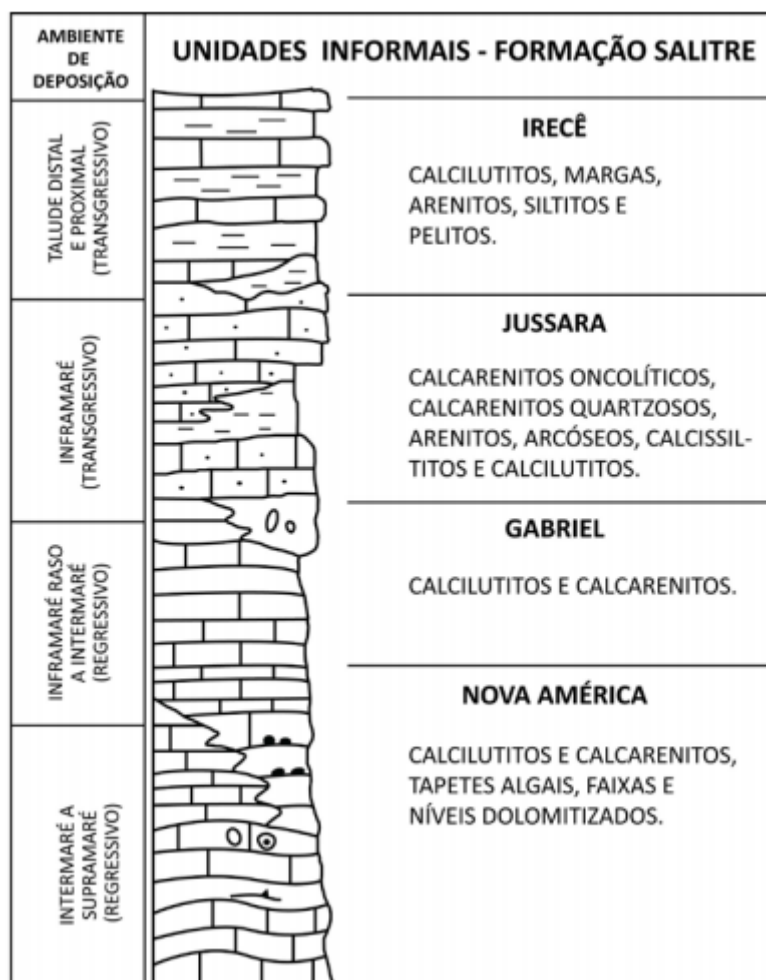


Figura 6: Unidades informais propostas para a Formação Salitre por Bomfim et al. (1985) e Pedreira et al. (1987). Figura adaptada a partir de Lagoeiro (1990) e extraída de Santana (2016).

Unidade Nova América

A Unidade Nova América é equivalente às unidades Nova América e Gabriel e a fácies Lapão, descritas por Bomfim et al. (1985), englobando a unidade Sarandi, descrita por Pedreira et al. (1987). A Unidade é dividida em duas subunidades: Nova América Inferior e Nova América Superior.

A subunidade Nova América Inferior é constituída por calssisiltitos com laminação plano-paralela e laminitos algais ondulados, sendo que os laminitos predominam na subunidade, e apresentam estruturas tepees associados a nódulos de calcita, além de *bird's eyes* e truncamentos irregulares. Os calcissiltitos com laminação paralela apresentam tonalidades claras e podem passar a calcarenitos de granulação fina com estratificação suavemente ondulada.

Já a subunidade Nova América Superior é caracterizada por dolomitos cinza-claros, doloarenitos oolíticos e dolorrúditos. Nessa subunidade são observadas as ocorrências de fosfato e Zn-Pb associados aos dolomitos. Os dolomitos oolíticos possuem estratificação gradacional e estratificações cruzadas *hummocky*, enquanto que nos doloarenitos finos a estratificação é gradacional.

Subunidade Sarandi

Aflora em locais restritos na parte central da Bacia de Irecê, sendo composta essencialmente por calcissiltitos e calcarenitos peloidais, podendo conter oncolitos e intraclastos. A estrutura sedimentar predominante na subunidade é a estratificação plano-paralela, sendo que, subordinadamente, ocorrem laminações planas e cruzadas, além de marcas de carga (Pedreira et al., 1987).

As litologias e estruturas sedimentares presentes sugerem um ambiente de sedimentação de supramaré a intermaré para a Unidade Nova América. A Subunidade Sarandi é interpretada como tendo sido depositada em um ambiente de inframaré.

Unidade Jussara

É reconhecida por Bomfim et al. (1985) e Pedreira et al. (1987). Souza et al. 1993 dividem a unidade em duas subunidades, denominadas de Subunidade Jussara Inferior e Subunidade Jussara Superior. A Subunidade Jussara Inferior é representada por calcissiltitos com estratificação plano-paralela, calcilutitos, calcarenitos oolíticos e/ou oncolíticos e calcarenito com concreções. Bonfim et al. (1985) incluem nessa subunidade calcarenitos quartzosos e arenitos arcosianos.

A Subunidade Jussara Superior é caracterizada por calcarenitos finos, médios e grossos, oolíticos e/ou oncolíticos de granulação grossa. Os calcarenitos finos possuem cor cinza-escuro e são odorosos. Ocorrem em bancos de espessura centimétrica, intercalados com calcilutitos com aspecto de laminitos algais. Os calcarenitos de granulação média são cinza-escuro ou cinza claro,

apresentam-se em bancos maciços ou finamente bandados, intercalados localmente com níveis de estromatólitos. Os calcarenitos oolíticos e/ou oncolíticos ocorrem em bancos de espessura métrica, apresentam estratificação cruzada sigmoidal ou, às vezes, maciços.

A Subunidade Jussara Inferior é interpretada como sendo depositada em um ambiente de maré, especificamente no intervalo entre a supramaré e intermaré. Em contrapartida, a Subunidade Jussara Superior é interpretada como tendo sido depositada em um ambiente de inframaré.

Unidade Irecê

A unidade Irecê é caracterizada por uma alternância de níveis carbonáticos e terrígenos. Os níveis carbonáticos são constituídos por calcarenitos finos a calcilutitos de cor cinza-escuro a negra, e os terrígenos são representados por margas, siltitos, arenitos imaturos e sílex. A alternância entre carbonatos e siliciclásticos é característica para a unidade. A Unidade Irecê é interpretada como tendo sido depositada abaixo do nível das ondas.

Em suma, as unidades reconhecidas na Formação Salitre caracterizam-se, segundo Souza *et al.* (1993), em quatro ciclos de sedimentação, sendo dois regressivos e dois transgressivos (Figura 7).

CICLO	SOUZA et al. 1993	PEDREIRA et al. (1987)	BOMFIM et al. (1985)
IV	TRANSGRESSIVO JUSSARA Superior JUSSARA Inferior	Jussara	Sup. Med Jussara Inf.
III	REGRESSIVO NOVA AMÉRICA Superior IRECÊ NOVA AMÉRICA Inferior	Sarandi Gabriel Nova América	Gabriel Nova América Lapão
II	TRANSGRESSIVO JUSSARA Superior IRECÊ		
I	REGRESSIVO NOVA AMÉRICA Superior NOVA AMÉRICA Inferior		

Figura 7: Correlação das unidades definidas por Souza et al. 1993 com trabalhos anteriores. Figura adaptada de Souza et al. (1993).

1.3.3 Síntese da evolução tectônica

Durante o ciclo Transamazônico, que ocorreu durante o Paleoproterozoico (2.3-2.15 Ga), os quatro segmentos crustais do Cráton São Francisco, Bloco Gavião, Bloco Serrinha, Bloco Jequié e corredor Itabuna-Salvador-Curaçá colidiram, resultando na formação de uma importante cadeia de montanhas (Barbosa e Sabaté, 2004).

A sequência Espinhaço inferior iniciou após o evento transamazônico em eventos de riftamento intraplaca que ocorreram no Cráton São Francisco durante a tafrogênese Estateriana (1.8 – 1.6 Ga). A Seção Estateriana inclui a porção basal do Grupo Diamantina na Serra do Espinhaço Meridional, o Grupo Oliveira dos Brejinhos na Serra do Espinhaço Setentrional e o grupo Rio dos Remédios na região da Chapada Diamantina. (Martins-Neto, 2000; Pedreira e De Waele, 2008; Danderfer et al., 2009; Chemale et al., 2012; Santos et al., 2013).

As unidades estratigráficas do Espinhaço Intermediário foram depositadas entre 1.60 e 1.38 Ga, estas sequências estão expostas na Serra do Espinhaço Setentrional e na Chapada Diamantina como preenchimentos de uma bacia *rift-sag*.

O Espinhaço Superior, depositado entre os períodos Steniano-Toniano (1.19 e 0,9 Ga) em uma bacia do tipo *rift-sag*, está representado na região da Chapada Diamantina pela deposição das Formações Caboclo e Morro do Chapéu.

A deposição do Supergrupo São Francisco está representada pelas Formações Bebedouro e Salitre. O grupo Macaúbas, correlato da Formação Bebedouro, é interpretado como uma bacia do tipo *rift*, com deposição glaciogênica formada durante o período Toniano (Cruz e Alckim, 2006).

A deposição da Formação Salitre está aparentemente associada com uma transgressão marinha, durante o período em que a área cratônica foi convertida em bacia de *foreland* por conta das cadeias orogênicas que se formaram nas margens do cráton durante o ciclo brasiliano. A Formação Salitre é correlata do Grupo Bambuí na bacia São Francisco. A Idade de Grupo Bambuí ainda é muito discutida na literatura, mas fósseis ediacaranos encontrados em pelitos por Warren et al. (2014) definem a sua idade de deposição em 550 Ma.

A inversão do Aulacógeno do Paramirim ocorreu devido às colisões envolvendo o Cráton São Francisco com outras placas durante a montagem do supercontinente Gondwana ocidental no final do Neoproterozoico (Alkmim et al., 2001;2006).

CAPÍTULO 2

2 ISOTOPE SIGNATURES AS FINGERPRINTS FOR FACIES AND FLUID-ROCK INTERACTIONS: IMPLICATIONS FOR CARBONATE RESERVOIR FLUID MIGRATION

Igor A. P. Taveira¹, Lucieth C. Vieira¹, Roberto V. Santos¹, Cleber P. Gomes Junior¹, Diego C. C. Couto¹, Paola F. Barbosa¹, Francisco H. R. Bezerra²

¹Institute of Geosciences, University of Brasília, Brasília, DF, Brazil

²Department of Geology, Federal University of Rio Grande do Norte, Natal, RN, Brazil

*Corresponding author: iaptaveira@gmail.com

Abstract

Carbonate reservoir analogs are essential for understanding the history of fluid flow in complex carbonate systems. In this study, we address the relationship between lithofacies and fluid-rock migration in carbonate rocks based on detailed petrographic and geochemical data ($\delta^{13}\text{C}$, $\delta^{18}\text{O}$, and $^{87}\text{Sr}/^{86}\text{Sr}$). Facies analysis was carried out in a section with continuous exposure which produced a 345 m-thick stratigraphic column. We grouped the facies into three associations distributed across a carbonate ramp system. The lower part of the stratigraphic column displays limestone that was deposited under open-basin conditions. In contrast, the intermediate and upper parts of the stratigraphic column shows that dolostones were deposited under restricted basin conditions. Deposition and superimposed diagenetic processes vary significantly across the section, as indicated by petrographic and isotope data. We show that postsedimentary diagenetic processes followed by tectonic imprints changed the petrophysical properties of these rocks and strongly affected fluid flow. The geochemical data reveal that the fractured dolomites in the intermediate part of the section formed the primary fluid flow pathway across the succession and parallel to the sedimentary layers. We also identified two groups of veins that cross-cut the dolomites. One group is characterized by negative $\delta^{13}\text{C}$ and $\delta^{18}\text{O}$ values and radiogenic $^{87}\text{Sr}/^{86}\text{Sr}$ ratios which have been interpreted as hydrothermal fluids derived from outside the carbonate system. The second group of veins have $\delta^{13}\text{C}$ and $\delta^{18}\text{O}$ values that are similar to those of the host rock and were related to pressure-solution mechanisms. By combining facies analysis, diagenesis, and isotope geochemistry, we identify the primary fluid flow zones and fluid-rock interaction processes.

Keywords: Facies analysis, Neoproterozoic carbonates, isotope geochemistry, fluid-rock interaction

Highlights

- The δO^{18} and δC^{13} levels from the host rock are primary and are related to the different stages of basin evolution;
- The $^{87}\text{Sr}/^{86}\text{Sr}$ ratio changed during the course of diagenesis;
- There were different fluid sources for the veins;
- The paleoenvironmental and diagenetic conditions were fundamental for establishing fluid flow

2.1 INTRODUCTION

Fluid flow in carbonate rocks is usually related to a complex network that includes fractures, faults, and facies-controlled pathways (Peacock, 2002; Agosta et al., 2010; Michie et al., 2014; Peacock et al., 2016; 2017; 2018). Predicting fluid migration in this kind of rock type has become increasingly critical because such rocks are important reservoirs for water, oil, and gas worldwide (Montaron, 2008). In most instances, primary fluid pathways in carbonate rocks are controlled by diagenesis and tectonics, which are processes that occur during different stages of evolution of these rocks (Laubach et al., 2010). Diagenetic processes are usually associated with shallow conditions when carbonate sediments still have abundant pore fluids. At increased burial depths, fluids are expelled by compression and sediment permeabilities tend to decrease. Under these conditions, fluid pathways are strongly dependent on fractures and, consequently, on geomechanical properties that are controlled by mineralogical and chemical processes (Bjorlykke et al., 1994).

Diagenesis involves interactions of carbonate rocks with fluids of different origins (e.g., marine, meteoric, and hydrothermal) which result in secondary textures and changes in petrophysical properties (Mazzullo and Harris, 1992; Kaufman and Knoll, 1995; Moore, 2001; Frimmel, 2010). During eodiagenesis, the interactions with meteoric water and mixing may significantly affect the primary porosity of these rocks (Giles and Marshall, 1986) while during mesodiagenesis, acidic fluids generated by chemical processes within the basin play a major role in the dissolution and precipitation reactions. These acidic fluids may have different sources such as CO_2 degassing (Giles and Marshall, 1986; Clayton, 1990; Biel et al., 2016), carboxylic acids originating from organic matter degradation (Giles and Marshall, 1986), mineral reactions in shales (Bjorlykke, 1983; Giles and Marshall, 1986), and thermochemical sulfate reduction reactions (Machel et al., 1995; Machel, 2001; Jiang et al., 2018). In most instances, diagenesis promotes dolomitization and is accompanied by increased rock porosity (Weyl, 1960; Chen et al., 1985; Wang et al., 2015).

In addition to diagenesis, fractures and faults are essential for the creation of fluid pathways in deep-seated carbonate rocks in which geomechanical properties exert primary control over porosity and permeability (Bjorlykke et al., 1994; 1997). As shown by previous studies (Becker and Gross, 1996; Hanks et al., 1997; Underwood et al., 2003; Cooke et al., 2006), stratigraphic relationships may control the density of fractures within a sedimentary succession rather than the tectonics. Hence, predicting fluid flow in massive carbonate successions depends on integrated approaches that involve multidisciplinary studies.

Reconstructing fluid pathways in ancient carbonate successions may be challenging due to superimposed processes that leave their imprints on these rocks. In most instances, fluid flow imprints the changes in geochemical parameters (e.g., $\delta^{18}\text{O}$, $\delta^{13}\text{C}$, and $^{87}\text{Sr}/^{86}\text{Sr}$) that are controlled by temperature, primary composition of rocks and fluids, water/rock ratios, and whether fluid-rock interactions occurred under open or closed conditions (Banner and Hanson, 1990). Previous studies have shown that, at shallow burial depths, fluid flow imprints the pervasive changes in the isotopic compositions of carbonate rocks (Moore, 1989; 2001; Choquette and James, 1990; Swart and Eberli, 2005). In contrast, under tectonic regimes, fluid flow is concentrated in the central cores of active fault systems (Pili et al., 2002) which leads to restricted isotopic changes in carbonate rocks. Determining the nature of fluid-rock interactions and the timing of these events is essential for understanding the main controls on present-day circulation in deep-seated carbonate successions. This type of approach requires well-exposed successions that display clear relationships between diagenetic and tectonic features.

In the Achado Quarry, northeastern Brazil, Neoproterozoic carbonates outcrop continuously for approximately 345 m. Placed vertically by tectonic processes, these carbonates have multiple burial and hydrothermal diagenetic histories which are comparable to many rocks of this age (Shields and Veizer, 2002; Halverson et al., 2005; Misi et al., 2007). These complex diagenetic and tectonic histories mean that this area is an ideal site for investigating the controls on fluid flow in complex carbonate systems.

In this work, we performed a detailed investigation of the Achado Quarry, including facies analysis, petrography, and sampling for geochemistry (e.g., $\delta^{18}\text{O}$, $\delta^{13}\text{C}$ and, $^{87}\text{Sr}/^{86}\text{Sr}$). Based on these data, we have been able to define the main mechanisms of fluid pathways that are related to primary and diagenetic processes and tectonic imprints.

2.2 GEOLOGICAL BACKGROUND

The study area comprises the Salitre Formation in the Irecê Basin which is located in the northern part of the São Francisco craton (Figure 1). This cratonic area is surrounded by

Neoproterozoic mobile belts (e.g., Brasília, Rio Preto, Riacho do Pontal, Sergipana and Araçuaí belts) that were not affected by the pervasive deformation and metamorphism of the Brasiliano orogeny (750-540 Ma) (Cruz and Alkmim, 2006; Alkmim and Martins-Neto, 2012; Brito Neves et al., 2014). The São Francisco craton is composed of Archean-Paleoproterozoic basement units and Meso- and Neoproterozoic sedimentary units that overlie the older basement (Barbosa and Sabaté, 2004; Cruz and Alkmim, 2006).

The sedimentary cover of the São Francisco craton occurs as two distinct morphotectonic domains, namely, the Paramirim aulacogen and the São Francisco Basin. The study area is located in the Paramirim aulacogen which is represented by Precambrian fill units of the Paleo/Mesoproterozoic Espinhaço and Neoproterozoic São Francisco supergroups (Cruz and Alkmim, 2006). The aulacogen represents rift-sag events from the Estonian to the Tonian (1.8 – 0.9 Ma). It was partly inverted in the late Neoproterozoic by the Brasiliano orogeny (Schobbenhaus 1996; Cruz and Alkmim, 2006; Alkmim e Martins-Neto, 2012).

The Neoproterozoic sedimentary fills of the Paramirim aulacogen are represented by the São Francisco Supergroup which consists of the Una Group which is subdivided into the Bebedouro and Salitre Formations (Cruz and Alkmim, 2006). The Bebedouro Formation is a glaciogenic succession composed of diamictites, pelites and sandstones that is separated from the older units by a regional unconformity (Guimarães, 1996). Detrital U-Pb zircon dating of the Bebedouro Formation indicates a maximum depositional age of 874 ± 9 Ma (Figueiredo, 2008).

The Salitre Formation consists predominantly of carbonate sequences up to 1,200 m thick. These carbonates overlie the glaciogenic deposits of the Bebedouro Formation and sedimentary rocks from the Chapada Diamantina Group (Misi and Kyle, 1994). The Salitre Formation is composed of calcitic and dolomitic carbonate rocks with small intercalations of detrital rocks and its main lithotypes are calcilutite, calcisiltite, dolo/lime calcarenites and stromatolites (Misi and Veizer, 1998).

Two lithostratigraphic subdivisions are proposed for the Salitre Formation. Misi and Silva (1996) subdivided the Salitre Formation into five informal units referred to by the letters C, B, B1, A and A1 while Bomfim et al. (1985) designated the units as Nova América, Gabriel, Jussara and Irecê.

The inversion of the Paramirim aulacogen occurred due to collisions of the São Francisco craton with other plates during the assembly of the West Gondwana supercontinent at the end of the Neoproterozoic (Alkmim et al., 2001; 2006).

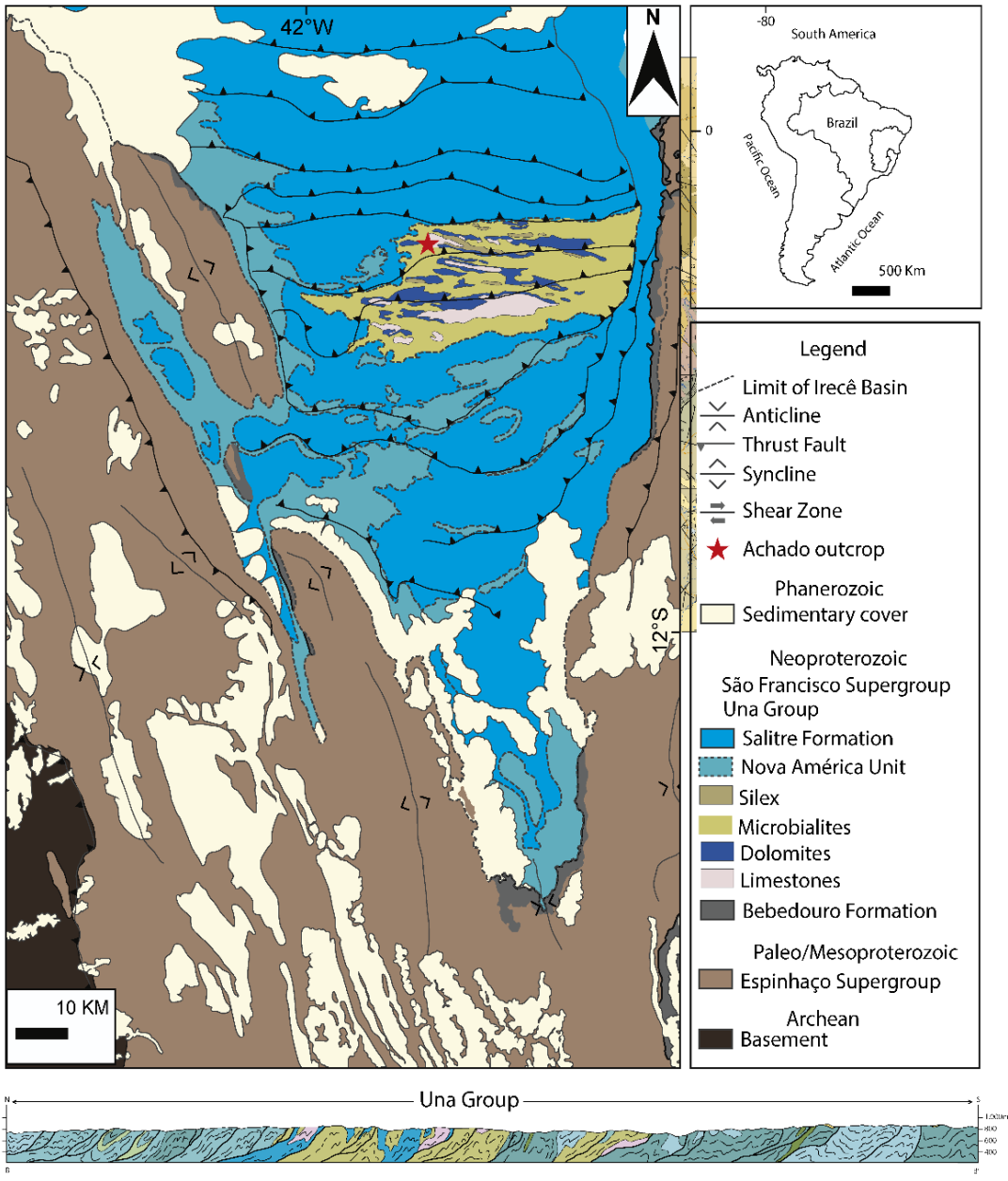


Figure 1: Irecê fold and thrust belt geologic map and NS-oriented cross-section. Based on Alkmim (2004), Kuchenbecker et al. (2011) and Redivo et al. (2019). The Achado quarry (red star) is the focus of this study.

2.3 MATERIAL AND METHODS

An analysis of sedimentary facies was carried out over a 345 m thick section with continuous exposure at Achado village, near Irecê, Bahia (NE Brazil) (Figure 1) and followed the systematics of Walker (1992). This area was previously mapped as occurring in the Nova América member of the Salitre Formation (Bomfim et al., 1985). The sedimentary facies were grouped in facies associations (FA) to identify depositional environments. The Dunham classification (Dunham, 1962) was used for carbonate rocks and the pore types were classified according to Choquette and Pray (1970).

A total of 389 samples were collected from the entire section and 27 samples were obtained from locations where there was contact between sedimentary rocks and structural features (veins and fills). Standard-thickness thin sections were prepared from 56 blue epoxy resin-impregnated samples for transmitted light microscopy. All thin sections were half-stained with Alizarin Red and potassium ferricyanide solutions to differentiate the carbonate minerals, as was discussed by Dickson (1966). Thin sections were described according to the systematics proposed by Flugel (2010). Diagenetic features that were not discernable using standard petrographic techniques were revealed using a Zeiss Axio Scope.A1 polarizing microscope equipped with a CITL mk5 Optical cathodoluminescence system. Cathodoluminescence (CL) microscopy was conducted on 16 polished thin sections.

All samples collected from the whole section from different facies were subjected to $\delta^{13}\text{C}$ and $\delta^{18}\text{O}$ determinations. Sampling was conducted at a regular interval of 1 meter and was preferably performed in portions without fractures, alterations or venules. In some intervals, more than one sample was taken with a goal of evaluating the lateral reproducibility of the isotopic data. A total of 27 samples were selected for $\delta^{13}\text{C}$ and $\delta^{18}\text{O}$ determinations in host rocks and veins/fills and each sample was powdered using a microdrill.

All samples were analyzed on a Delta V plus mass spectrometer connected to a Gas Bench II apparatus at the Geochronology and Isotope Geochemistry Lab at the University of Brasília. The samples were reacted with H_3PO_4 at a temperature of 72°C after flushing the flask using helium to remove atmospheric gases. Carbon and oxygen isotopes are reported in delta notation relative to the Pee Dee Belemnite reference standard (V-PDB; Craig, 1957). All runs included the standard reference materials, NBS-18 and NBS-19. The uncertainties in isotope measurements were 0.05‰ for carbon and 0.10% for oxygen which were based on multiple analyses of an internal laboratory standard.

For $^{87}\text{Sr}/^{86}\text{Sr}$ analysis, 28 samples were selected from host rocks with powders being made while avoiding veins and secondary fills and six samples were from powder collected from veins/fills. $^{87}\text{Sr}/^{86}\text{Sr}$ analyses were performed after acid digestion of the powdered carbonate samples and analytical determinations were made using thermal ionization mass spectrometry in a Thermo Triton Plus thermal ionization mass spectrometer in a static multicollector (TIMS). Analyses were performed at the Geochronology and Isotope Geochemistry Laboratory of the University of Brasília. The Sr ratios were normalized by assuming an $^{87}\text{Sr}/^{86}\text{Sr}$ ratio of 0.1194. The standard used was NBS-987. The external reproducibility of the $^{87}\text{Sr}/^{86}\text{Sr}$ ratios from the NBS-987 standard was 0.710271 ± 0.000017 ($n = 20$).

2.4 RESULTS

2.4.1 Facies and facies associations

We identified 12 facies in the studied section (Table 1) (Figure 2.3 and 4), which were grouped into three facies associations distributed across a carbonate ramp system: (FA1) an inner carbonate ramp dominated by tidal process and microbialites, (FA2) an inner carbonate ramp dominated by waves and (FA3) a middle carbonate ramp dominated by storm waves. Despite well-preserved sedimentary structures, the entire sequence presents deformation features such as veins, fractures and faults. An integral and first-order structure consists of an oblique thrust-dominated fault with minor sinistral strike-slip components which is located in the upper part of the succession (Figure 2).

Facies	Structures	Processes	Environment	Facies Association
Flaser-bedded grainstone and lime mudstone (F1)	Flaser bedding, wave-ripples, mudcracks, tepee, evaporite pseudomorphs and stylolites	Deposition in the supratidal/intertidal environment due to alternation between traction and suspension processes during arid conditions	Supratidal/intertidal	FA1
Laminar stromatolite (F2)	Stromatolitic laminae	Deposition in the low energy peritidal environment. Authigenic precipitation of carbonate fluorapatite. The microbial activity probably helped in the carbonate precipitation due to removal of CO ₂	Intertidal	FA1
Laminated boundstone (F3)	Crenulated lamination	Deposition in the low energy peritidal environment. The microbial activity probably helped in the carbonate precipitation due to removal of CO ₂	Intertidal	FA1
Siliciclastic mudstone (F4)	lamination	Deposition of siliciclastic mud by suspension	Intertidal	FA1
Laminated dolostone extraclast rich interbedded with cross-bedded dolo grainstone (F5)	heterolithic bedding; grainstones with cross bedding and laminated dolostone.	Deposition in the intertidal environment due to alternation between traction and suspension processes. Deposition of extraclasts due to the proximal environment.	Intertidal	FA1
Cross-bedded intraclast rich lime grainstone (F6)	Cross-stratification	Deposition in the subtidal environment dominated by waves. The intraclasts probably represent clasts from the hardground reworked by waves	Upper subtidal	FA2
Cross-bedded dolograinstone with dolomudstone lenses (F7)	Cross-stratification, wave-ripple	Facies deposited in the subtidal environment during wave action.	Upper subtidal	FA2
Columnar stromatolites (F8)	Columnar stromatolites	Columnar stromatolites <i>Jurussania Krylov</i> . The stromatolite laminae are composed of authigenic carbonate fluorapatite. Facies deposited in the high energy intertidal environment	Intertidal	FA2

Dome-shaped stromatolites (F9)	Dome-shaped stromatolites	Stromatolite laminae composed of dolomicrite and some allochems, deposited through microbial trapping and binding sediments in the high energy intertidal environment.	Intertidal	FA2
Rudstone (F10)	Rudstone massive	Facies deposited in the intertidal environment during wave action. Intraclasts were reworked by waves.	Intertidal	FA2
Hummocky cross-stratified grainstone (F11)	Hummocky stratification	Facies deposited in the subtidal environment with storm action.	Subtidal	FA3
Thrombolite (F12)	Massive	Facies deposited in the subtidal environment below the fair-weather wave base	Subtidal	FA3

Table 1: Summary of facies, sedimentary structures, processes and facies association of the Salitre Formation in the Achado Quarry.

FA1 - Inner ramp dominated by tidal process and microbialites

These facies associations are characterized by grainstones, lime mudstone, laminar stromatolite, laminated boundstone interbedded with siliciclastic mudstone, and laminated dolostone. The lithologies of these facies associations are mainly limestones and dolostone with rare intercalations of siliciclastic mudstones. The sedimentary structures include heterolithic bedding, cross-bedding, microbial lamination, mud cracks, tepee structures, and evaporite pseudomorphs.

F1 – Flaser-bedded grainstone and lime mudstone

This facies consists mainly of flaser-bedded grainstone and lime mudstone with tepee structures and evaporite pseudomorphs (Figure 3A). The grainstones are tan and are characterized by wave ripples and are composed primarily of ooids and peloids. The lime mudstones are gray, laminated and are characterized by mud cracks and tepee structures and are composed mainly of microcrystalline calcite which is locally replaced by planar-s and euhedral dolomite (Figure 4A). The replacement by dolomite occurs mostly parallel to the bedding. Detrital grains include quartz and opaque minerals. Blocky calcite and length-slow quartz commonly replace evaporite nodule pseudomorphs (Figure 4B and 4C).

Microbial mats are a common feature in the lime mudstones between wave ripples. Stylolites occur parallel to as well as perpendicular to the laminations. It was not possible to identify any porosity based on the petrography.

F2 – Laminar stromatolite

F2 consists of black noncolumnar stromatolitic laminae that have considerable lateral continuity. Carbonate fluorapatite defines the laminations which have the same petrographic characteristics as the columnar stromatolites. The laminar stromatolites generally have lower phosphate concentrations than the columnar stromatolites (Misi and Kyle, 1994). This facies was also utilized as a stratigraphic marker.

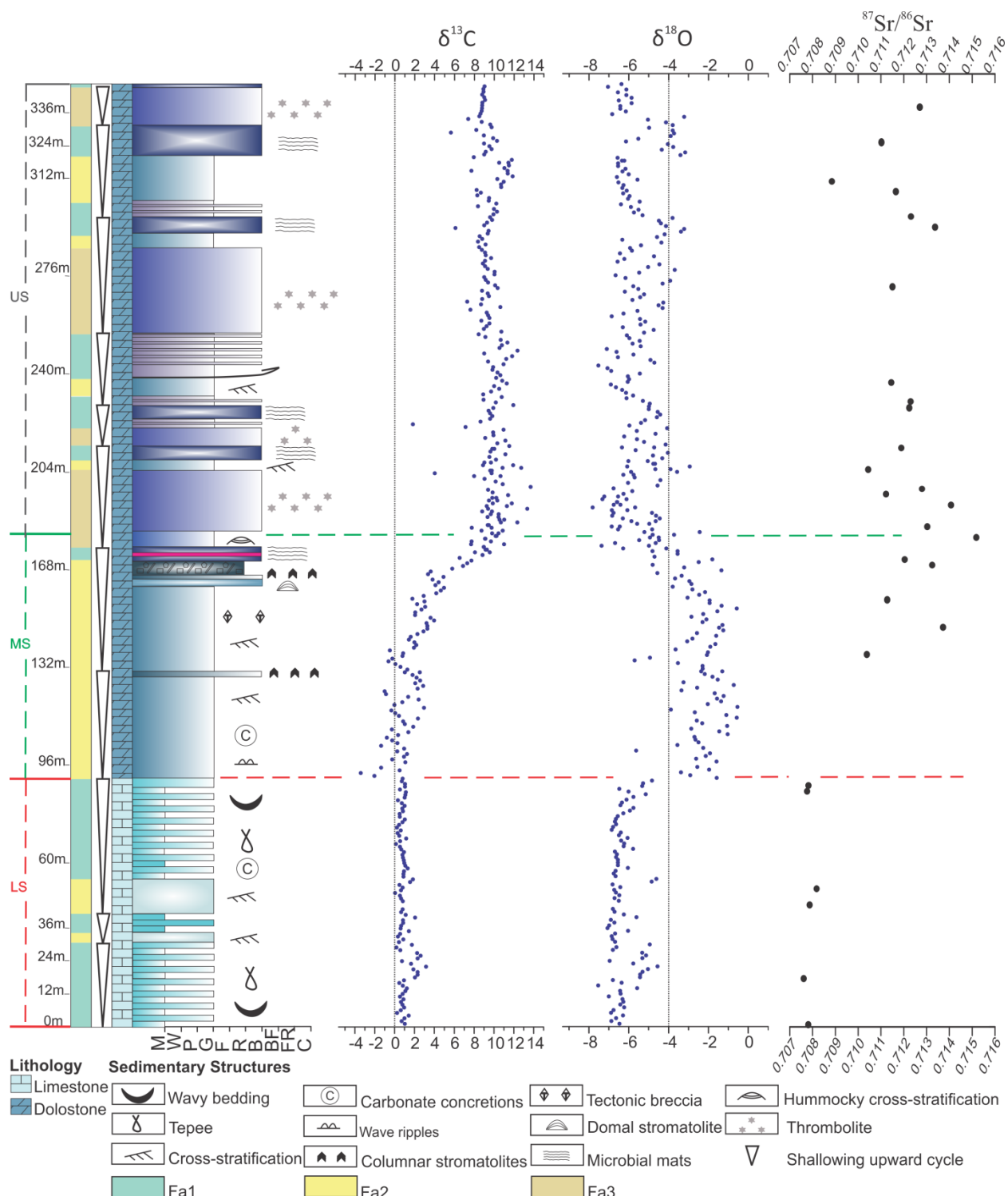


Figure 2: Stratigraphic column of the Achado Quarry with $\delta^{13}\text{C}$, $\delta^{18}\text{O}$ and $^{87}\text{Sr}/^{86}\text{Sr}$ data from host rock samples. Stratigraphic division: LS, Lower section; MS, Middle section; US, Upper section. Carbonate classification: M, Mudstone; W, Wackstone; P, Packstone; G, Grainstone; F, Floatstone; R, Rudstone; B, Boundstone; BF, Bafflestone; FR, Framestone; C, Crystalline.

F3 – Laminated boundstone

F3 is dolomitic, dark gray, and shows crenulated laminations. Its thickness varies from several centimeters to few meters and shows cyclicity throughout the section (Figure 3B). It is composed mainly of planar-s dolomite while rare dolomicrite peloids observed and also domains

with dolomicrite and detrital quartz (Figure 4D and 4E). Green stromatolite laminations composed of carbonate-fluorapatite are locally observed.

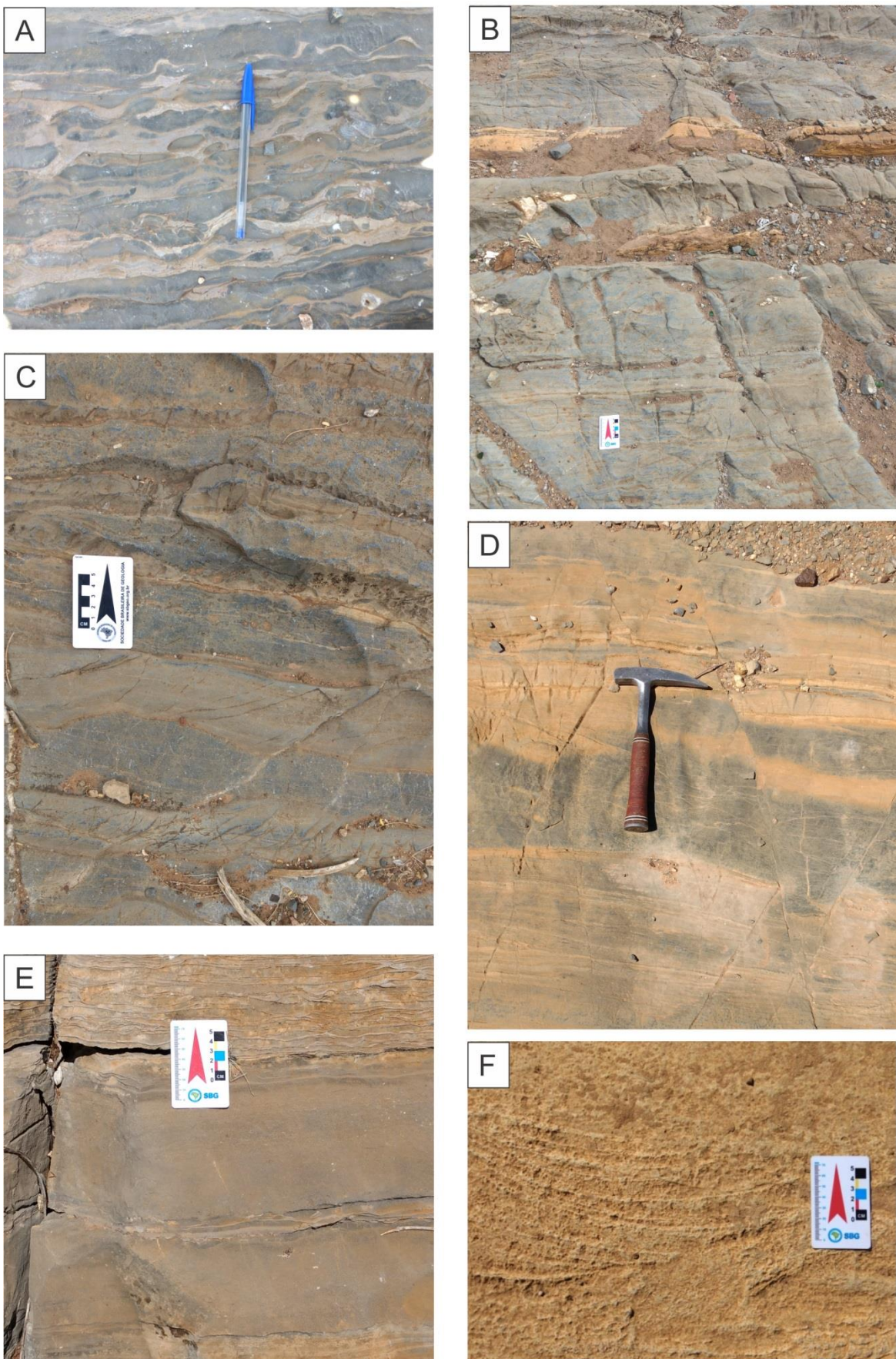


Figure 3: Facies found in Achado quarry. A) F1, flaser-bedded grainstone and lime mudstone; B) F3, laminated boundstone interbedded with laminated siliciclastic mudstone (F4); C) Laminated dolostone extraclast rich interbedded with cross-bedded dolo grainstone (F5); D) Facies F5 showing faults and fractures, near to the major sinistral transpressional fault; E) cross-bedded intraclast rich lime grainstone (F6); F) F7, cross-bedded dolo grainstone with dolo mudstone lenses.

F4 - Siliciclastic mudstone

F4 is represented by light brown, laminated siltstone, which has a thickness of a few centimeters (less than 20cm) and occurs interbedded with F3 (Figure 3B).

F5 - Laminated dolostone extraclast rich interbedded with cross-bedded dolo grainstone

F5 is composed of laminated dolostone interbedded with cross-bedded dolo-grainstone (Figure 3C, 3D, 9A and 9B). The laminated dolostone is composed mainly of microcrystalline dolomite. Detrital quartz, feldspar and opaque minerals are disseminated in this facies (Figure 4F). Planar-s dolomite and blocky calcite cement phases are common. The cross-bedded dolo grainstone is composed of peloids and detrital grains of quartz and feldspar (Figure 4F). Blocky calcite and length-slow quartz are the main cement phases filling vugs (Figure 4G). Planar-s cloudy core dolomite cement occurs subordinately. Some dolomite crystals show dissolution features and are replaced by blocky calcite.

Interpretation

All of the sedimentary structures such as heterolithic bedding, tepees, mud cracks, microbial laminations and evaporite pseudomorphs indicate that these carbonates were deposited in an inner ramp peritidal platform under arid climatic conditions. F1 is interpreted to have accumulated in an intertidal/supratidal environment. Microbial mats controlled the deposition of facies F2 and F3 which occurred in a low-energy peritidal environment. Microbial activity probably helped carbonate precipitation due to the removal of carbon dioxide from water by photosynthesizing bacteria (Frimmel, 2010). F5 represents an intertidal environment in which traction processes transported the grainstones and suspension processes carried the mud fraction.

FA2 - inner ramp dominated by waves

This facies association includes grainstones, rudstones and stromatolites. Nearly all facies are dolostones and the sedimentary structures consist of cross-bedding in addition to columnar and domic stromatolites. The main sedimentary and petrographic features of each facies are described below:

F6 Cross-bedded intraclast rich lime grainstone

F6 consists of light gray, cross-bedded, intraclast-rich lime grainstone. The bedding thickness is a few meters and F6 occurs interbedded with F1 (Figure 3E). Under the microscope, F6 is characterized by peloids, ooids and intraclasts. All allochems are micritized whereas the ooid nuclei are replaced with blocky calcite and this mineral phase constitutes the sparry cement (Figure 4H).

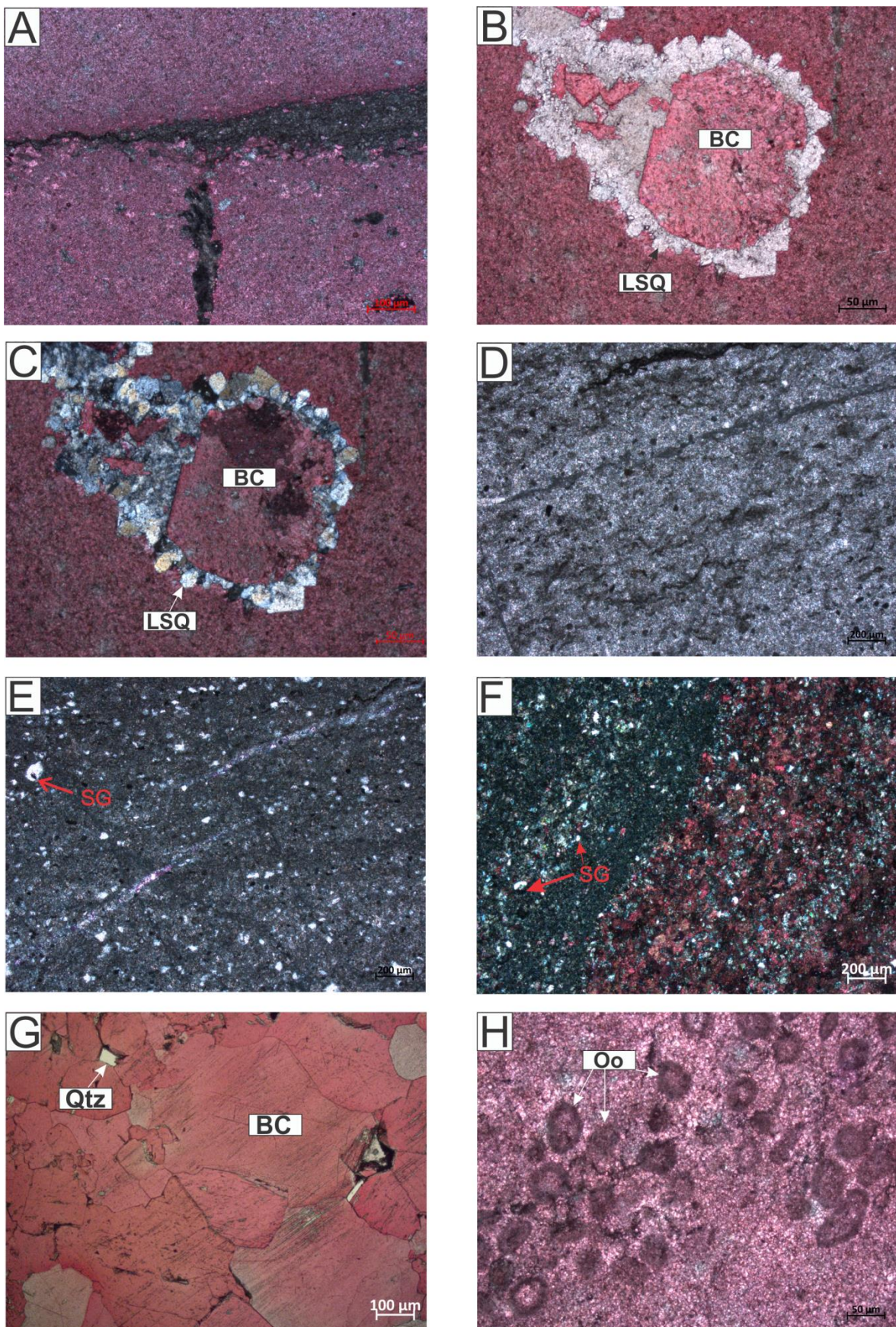


Figure 4: Diagenetic features A) Microcrystalline calcite replaced with planar-s dolomite; B) Nodules constituted of blocky calcite (BC) and length-slow quartz (LSQ) NP; C) Nodules constituted of blocky calcite(BC) and length-slow quartz (LSQ) NX; D) crenulated lamination in F3; E) detrital grains in F3 - SG = siliciclastic grains; F) F5, contact between extraclast-rich laminated dolostone interbedded with cross-bedded dolo grainstone - SG = siliciclastic grains; G) blocky calcite (BC) filling vug in F5. H) Ooids (Oo) and peloids replaced with blocky calcite in the core (F6).

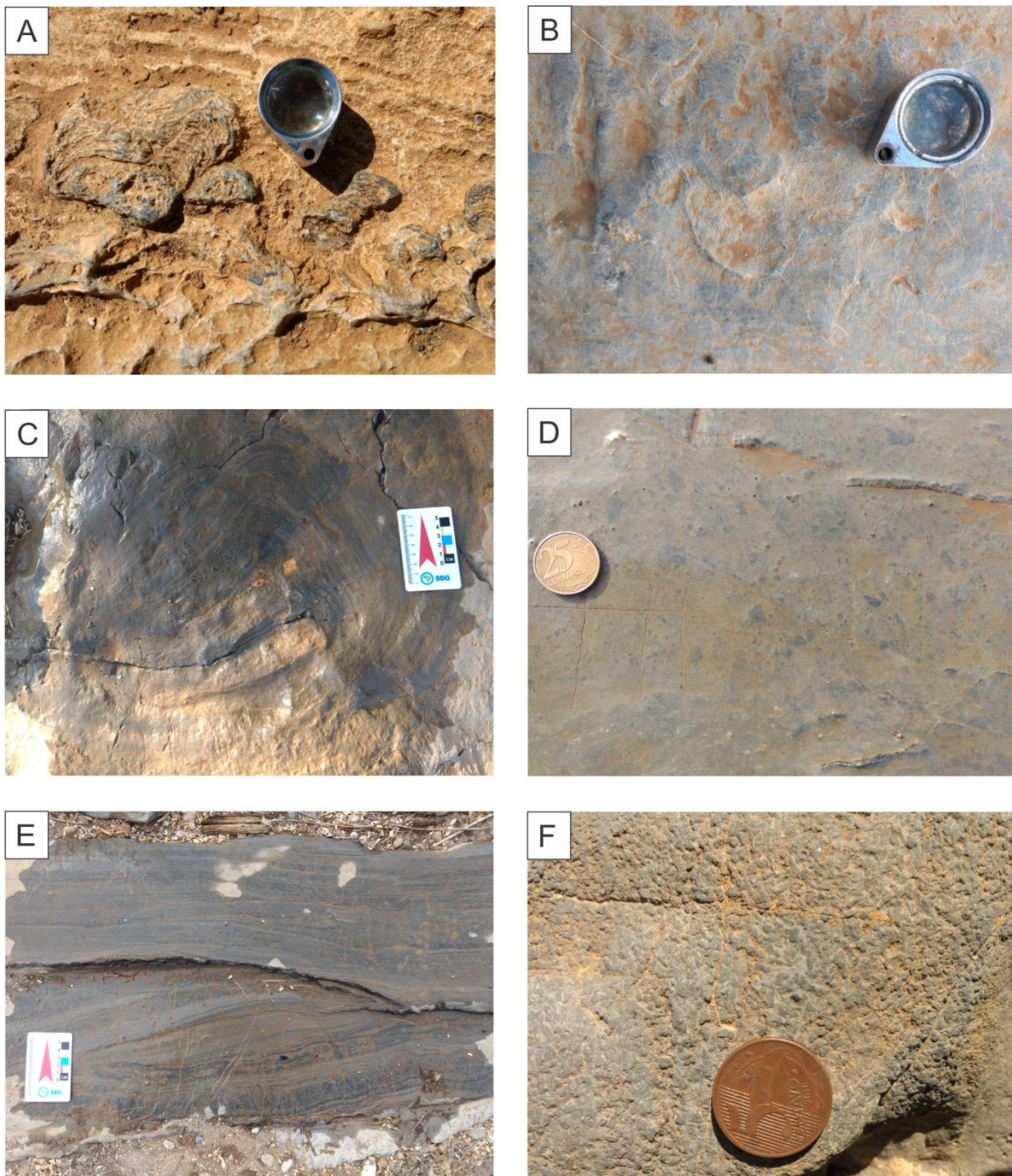


Figure 5: A) and B) F8, columnar stromatolites; C) F9, dome-shaped stromatolites); D) F10, rudstone; E) F11, Hummocky cross-stratified grainstone; F) Thrombolite, showing amoeboids, dark gray mesoclots separated by patches of light-colored dolo mudstones and sparry cement (F12).

F7 – Cross-bedded dolograinstone with dolomudstone lenses.

F7 is a tan cross-bedded dolograinstone with gray dolomudstone lenses. The grainstone shows wave-ripple structures as well as cross-stratification and contains millimeter-scale thick lenses of dolomudstone (Figure 3F). The grainstones consist of ooids, peloids and intraclasts. All of these constituents are microcrystalline dolomite which shows coarse-graining (Figure 6A). The cement phase present is mainly cloudy-center planar-s dolomite while some dolomite crystals show cloudy centers and limpid rims (Figure 6B).

Another cement phase present is blocky calcite which occurs by filling intergranular and intercrystalline spaces (Figure 6C and 6D). The pore type is mainly intercrystalline porosity which is present between dolomite crystals and vugs. The porosity itself is very low in this interval. Stylolites are a ubiquitous feature and are parallel to the stratification (Figure 6E).

In this facies, two types of tectonic rocks are observed, namely, a cataclasite (Figure 9C and 9D) and hydraulic breccia (Figure 9E and 9F). The cataclasite consists of grainstone clasts immersed in a comminuted matrix. The fracture and vein densities are very high and they are filled with blocky calcite. Hydraulic breccia occurs laterally and continuously in F7 and consists of clasts from the host rocks. The veins consist of saddle dolomite which show curved faces with sweeping extinction (Warren, 2000) and macrocrystalline calcite. Vugs are observed near the contact with the host rocks (Figure 7A) and within veins (Figure 7B).

F8 – columnar stromatolites

This facies consists of columnar stromatolites with average diameters 2.5 cm and lengths of 8 centimeters (Figure 5A e 5B). They were previously described by Srivastava (1986) as *Jurussania Krylov*; these stromatolites mainly occur in two layers which are up to 10 cm thick. As they extend laterally for more than 600 m, the layers were used as a stratigraphic marker across the outcrop. The stromatolite laminae are composed of carbonate fluorapatite and the intercolumnar spaces consist of dolomitic peloidal grainstone. The porosity observed in the grainstone is mainly intercrystalline and contains vugs (Figure 7C and 7D) that are often filled with blocky calcite.

F9 – Dome-shaped stromatolites

This facies consists of dark-gray dome-shaped stromatolites. F9 occurs as an isolated body. It is characterized by concentric laminations with stromatolite heads up to 30 cm in diameter (Figure 5C). Under the microscope, this facies is primarily composed of dolomicrite and some allochems such as peloids and intraclasts. Some of the grains, as well as the dolomicrite laminations, are replaced with cloudy core planar-s dolomite. Detrital grains represent up to 5% of the total rock volume. Nodular features are present and are filled with saddle dolomite and blocky calcite.

F10 - Rudstone

F10 is a dark-gray rudstone which is up to 3 m thick. The intraclasts range from several millimeters to a few centimeters in length and are immersed in a dark dolo mud matrix (Figure 5D). Under the microscope, the intraclasts consist of fine-grained recrystallized dolomite crystals and rare peloids are also present. The main cement phase is cloudy-center planar-s dolomite crystals and filled vugs. The main pore type observed is intercrystalline vugs filled with saddle dolomite and blocky calcite.

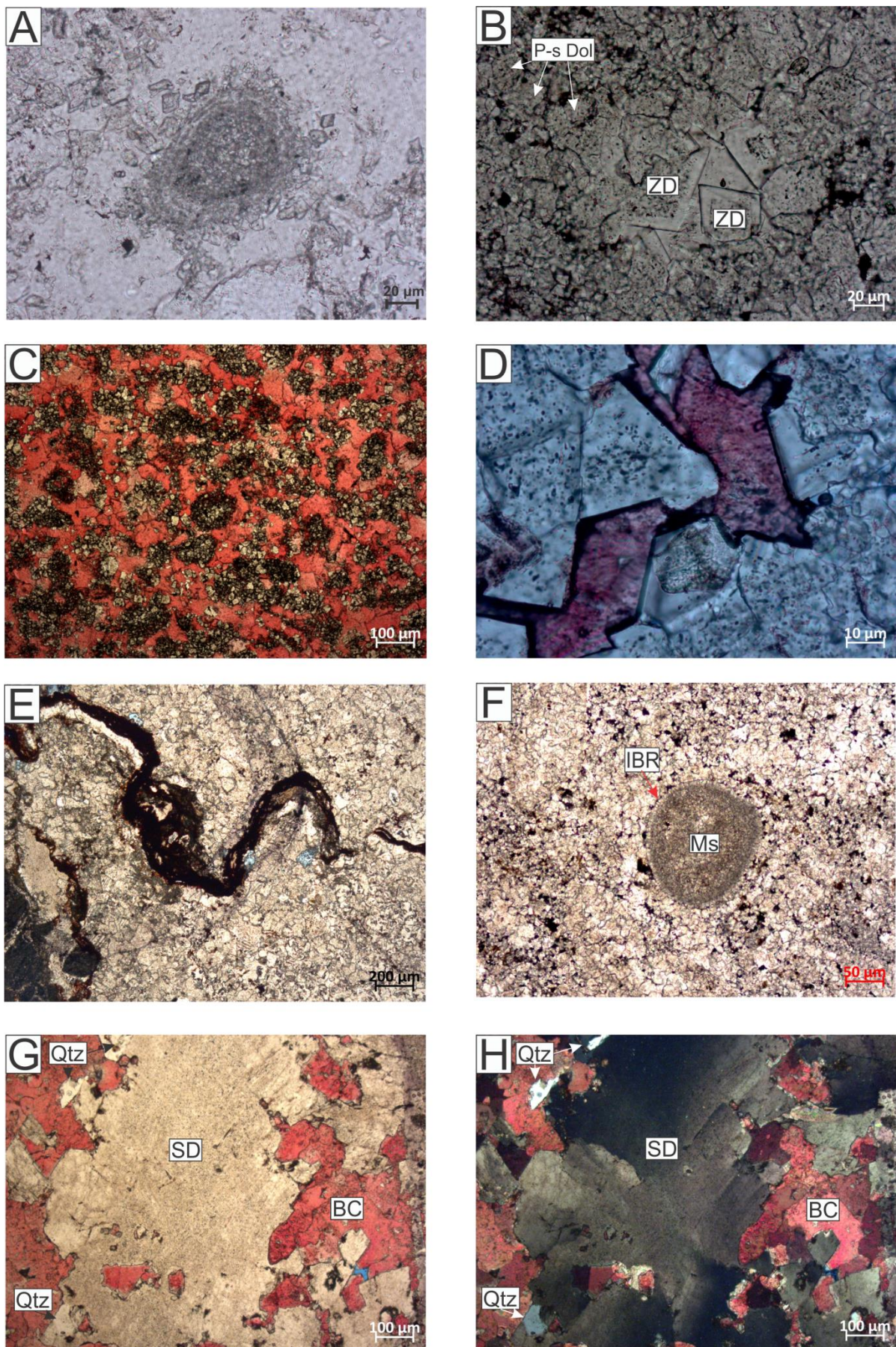


Figure 6: Diagenetic features: A) ooids with cortical layers, the mineralogy is dolomite; B) zoned dolomite (ZN) and planar-s dolomite (P-s dol) crystals; C) dolomicrite peloids partially recrystallized - red-stained minerals are block calcite; D) porosity filled by calcite. E) stylolite; F) Mesoclot (Ms) with dolomite isopachous bladed rim (IBR); G) PPL photomicrograph of saddle dolomite (SD), quartz (Qtz) and blocky calcite (BC); H) NX photomicrograph of saddle dolomite (SD), quartz (Qtz) and blocky calcite (BC).

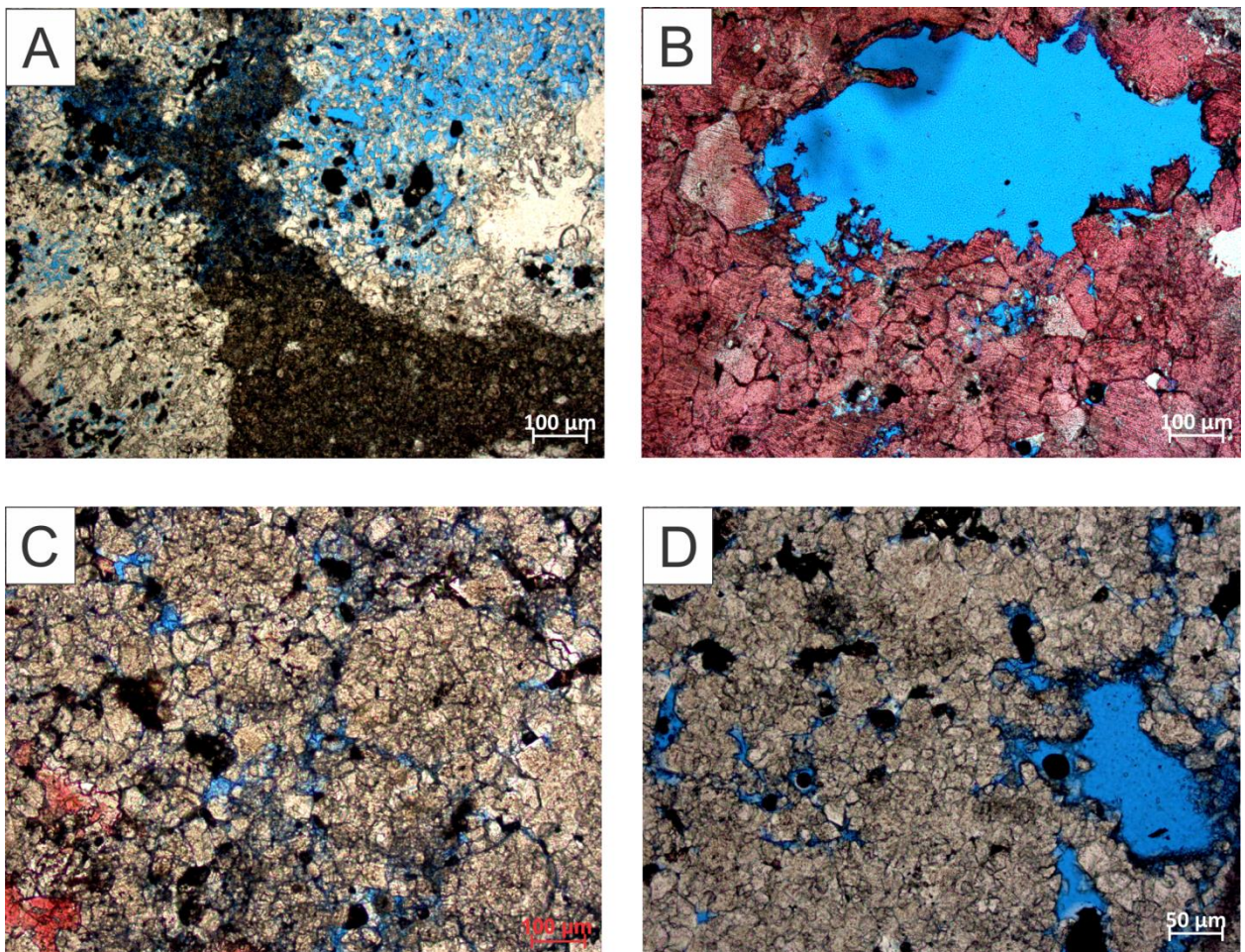


Figure 7: Main pore types found in our samples: A) intracrystalline porosity; B) vugs in red-stained blocky calcite; C) intercrystalline pores between dolomite crystals; D) vugs and intercrystalline pores between dolomite crystals.

Interpretation

This facies association represents deposition in a high-energy environment where F7 corresponds to a wave-dominated shallow subtidal shoal. The presence of ooids with cortical layers suggests aragonite as the primary mineral phase (Caird et al 2017; Hood and Wallace, 2018) (Figure 6A). The columnar and dome-shaped stromatolites indicate deposition in a high-energy intertidal environment. The columnar stromatolites formed phosphatic biostromes on intertidal flats (Caird et al., 2017). F10 represents wave reworking and redeposition in an intertidal environment.

FA3 - Mid carbonate ramp dominated by storm waves

Thrombolites and hummocky cross-stratified grainstone mainly characterize this facies association.

F11 – Hummocky cross-stratified grainstone

Facies F11 consists of light gray hummocky cross-stratified (HCS) dolomitic grainstone and occurs in the upper section (Figure 5E).

F12 – Thrombolite

This facies is gray and exhibits thicknesses ranging from a few to several meters and in some domains, some centimeters-thick grainstones are observed (F7). The mesoclotes are dark gray amoeboids which are separated by patches of light-colored dolo mudstone and sparry cement (Figure 5F). Under a petrographic microscope, the mesoclotes show a dolomitic texture and also isopachous rim cement (Figure 6F).

The spaces between mesoclotes are filled with dolomiticite and with planar-s dolomite cement. In this facies, there is hydraulic breccia which is similar to that found in F7. The difference here is that the breccia clasts are composed of fragments from F12 (Figure 9G and 9H). The host rock clasts consist of recrystallized dolomitic mesoclotes and the cement phase present is mainly planar-s dolomite. Veins and vugs are filled with saddle dolomite, macrocrystalline calcite and quartz (Figure 6G and 6H).

Interpretation

This facies association represents deposition in a mid-ramp subtidal environment with storm action below the fair-weather wave base. In the subtidal environment, the mesoclotes which constitute thrombolites are biogenic and were probably derived from calcification of microbial colonies in the sediments (Dongjie et al., 2013).

2.4.2 Isotope geochemistry

Considering the lithology, sedimentary features, and isotopic variations throughout the studied section, a division of the succession into three parts is proposed for better visualization and discussion of the data presented here. These parts have been designated as a lower section (LS), middle section (MS) and upper section (US) (Figure 2).

2.4.2.1 C and O isotope signatures

A total of 389 samples were analyzed along the whole section and revealed a wide range of $\delta^{13}\text{C}$ (-3.41‰ to +13.69‰) and $\delta^{18}\text{O}$ (-7.81‰ to -0.53‰) values (Figure 2) (Table 2). In the lower section, the $\delta^{13}\text{C}$ isotope values range from -0.46‰ to +3.17‰ and the $\delta^{18}\text{O}$ values range from -7.53‰ to -4.55‰. The middle section shows a major positive carbon isotope excursion in which the $\delta^{13}\text{C}$ values increase from -3.41‰ at the base to +8.85‰ at the top. The $\delta^{18}\text{O}$ values along the same interval vary from -5.59‰ to -0.53‰ and exhibit a negative correlation with respect to the carbon isotope values. The upper section shows very positive and nearly constant $\delta^{13}\text{C}$ values which range from +5.66‰ to +13.69‰ (excluding two outliers) and shows $\delta^{18}\text{O}$ values that range from -7.81‰ to -2.43‰.

A total of 27 samples were analyzed for $\delta^{13}\text{C}$ and $\delta^{18}\text{O}$ isotope composition of veins and fills, which show very discrepant values, and based on their isotope signature, two groups can be defined (Figure 8). Group 1, located in the middle and upper sections, is characterized by $\delta^{13}\text{C}$ values ranging from -8.89 ‰ to +0.61 ‰ and $\delta^{18}\text{O}$ ranging from -9.29‰ to -4.24 ‰ (Figures 8 9D 9F and 9H). Group 2, located in the upper section near the sinistral transpressional fault, shows $\delta^{13}\text{C}$ isotope values ranging from +4.48 ‰ to +10.37‰ (excluding one outlier), and $\delta^{18}\text{O}$ isotopes values ranging from -7.46 ‰ to -4.34 ‰ (Figures 8 and 9B).

A total of 27 samples were analyzed to determine the $\delta^{13}\text{C}$ and $\delta^{18}\text{O}$ isotope compositions of veins and fills which show very divergent values; based on their isotope signature, two groups were defined (Figure 8). Group 1, which is located in the middle and upper sections, is characterized by $\delta^{13}\text{C}$ values ranging from -8.89 ‰ to +0.61 ‰ and $\delta^{18}\text{O}$ values ranging from -9.29‰ to -4.24 ‰ (Figures 8, 9D, 9F and 9H). Group 2, which is located in the upper section near the sinistral transpressional fault, shows $\delta^{13}\text{C}$ isotope values ranging from +4.48‰ to +10.37‰ (excluding one outlier) and $\delta^{18}\text{O}$ isotope values ranging from -7.46‰ to -4.34‰ (Figures 8 and 9B).

2.4.2.2 *Sr isotope*

The $^{87}\text{Sr}/^{86}\text{Sr}$ ratios of a total of 34 samples were analyzed which covered most of the stratigraphic column and included veins and fills (Figure 2 and 8) (Tables 2 and 3). The $^{87}\text{Sr}/^{86}\text{Sr}$ ratios across the entire section showed a wide range of values. The lower section showed the lowest values which ranged from 0.70762 to 0.70818. The middle section showed values ranging from 0.71039 to 0.71373 with one outlier that showed the highest value for the host rocks with an $^{87}\text{Sr}/^{86}\text{Sr}$ ratio of 0.7279 (Figure 9F). The values in the upper section ranged from 0.70885 to 0.71519 (Figure 9H). The $^{87}\text{Sr}/^{86}\text{Sr}$ ratios for veins and fills were analyzed in the hydraulic breccia, which was located in the middle and upper sections and showed values ranging from 0.71056 to 0.73854 (Figures 9F and 9H).

2.5 DISCUSSION

2.5.1 Depositional model

The relative distribution and temporal evolution of the facies associations recorded in the studied succession are schematically outlined in Fig. 10. The depositional system is characterized by tens of meters-thick tidal and wave-influenced carbonate deposits and microbialites that are within a carbonate ramp system.

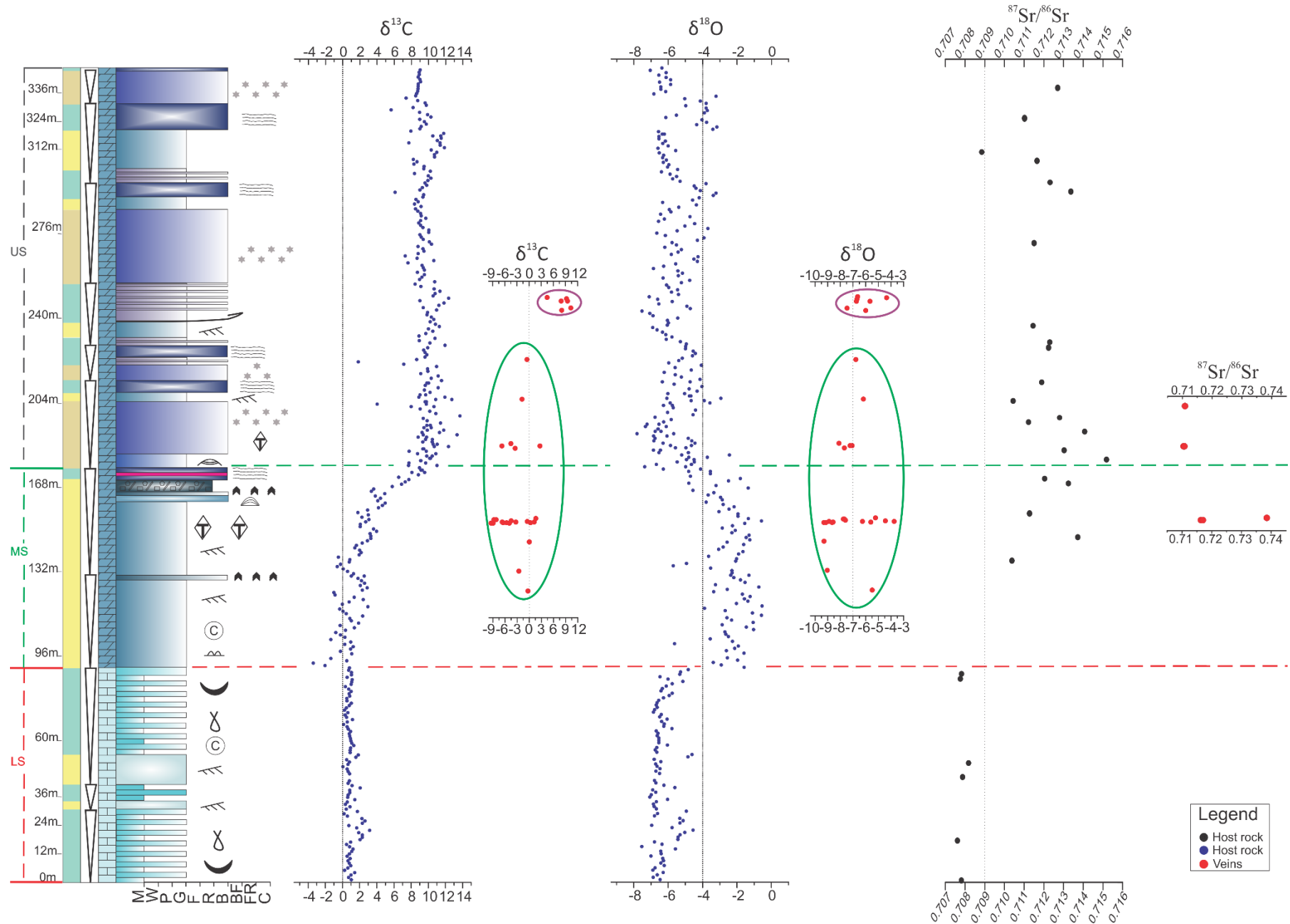


Figure 8: Isotope values for host rock and veins. The green and purple circles represent isotopic values of two groups of veins. The red dots in the green circle represent $\delta^{13}\text{C}$ and $\delta^{18}\text{O}$ values of group 1. The red dots in the purple circle represent $\delta^{13}\text{C}$ and $\delta^{18}\text{O}$ values of group 2.

Sample	Lithology	Facies	$\delta^{13}\text{C}$	$\delta^{18}\text{O}$	$^{87}\text{Sr}/^{86}\text{Sr}$	Stratigraphic position (m)
CARB 775	Limestone	F1	1.02	-6.45	0.70782	1
CARB 792	Limestone	F1	2.05	-5.43	0.70762	18
CARB 819	Limestone	F2	0.8	-6.79	0.70788	45
CARB 825	Limestone	F2	0.81	-6.42	0.70818	51
CARB 860	Limestone	F1	1.12	-6	0.70777	86
CARB 863	Limestone	F1	1.04	-5.27	0.70783	89
CARB 538	Dolostone	F3	0.86	-2.01	0.71039	137
CARB 40A	Dolostone	F3	1.99	-3.17	0.71373	147
CARB 67C	Dolostone	F3	2.3	-5.28	0.7279	148
CARB 43	Dolostone	F3	3.55	-3.68	0.71128	157
CARB 573	Dolostone	F6	6.54	-4.69	0.71205	172
CARB 52B	Dolostone	F11	8.53	-6.1	0.71519	180
CARB 585	Dolostone	F11	9.38	-4.96	0.71304	184
CARB 593	Dolostone	F11	9.89	-6.58	0.71408	192
CARB 624	Dolostone	F11	9.87	-5.82	0.71123	196
CARB 57A	Dolostone	F11	9.27	-5.28	0.71281	198
CARB 633	Dolostone	F3	12.76	-6.07	0.71045	205
CARB 642	Dolostone	F12	11.55	-4.14	0.71119	213
CARB 656	Dolostone	F9	9.93	-4.98	0.71225	227
CARB 659	Dolostone	F9	8.95	-6.1	0.71231	230
CARB 666	Dolostone	F3	10.84	-5.97	0.71146	237
CARB 701	Dolostone	F11	10.13	-4.29	0.71151	272
CARB 723	Dolostone	F19	9.02	-4.38	0.71338	294
CARB 727	Dolostone	F12	9.95	-5.73	0.71232	298
CARB 736	Dolostone	F3	8.25	-6.32	0.71166	307
CARB 739	Dolostone	F3	10.99	-5.55	0.70885	310
CARB 754	Dolostone	F9	10.31	-5.51	0.71103	325
CARB 767	Dolostone	F11	8.82	-5.85	0.71271	338

Table 2: C, O, Sr-isotope ratio for host rock samples. More data in the supplementary material.

Sample	$\delta^{13}\text{C}$	$\delta^{18}\text{O}$	$^{87}\text{Sr}/^{86}\text{Sr}$	Stratigraphic position (m)
CARB 40B	-5.52	-8.58	0.71638	147
CARB 40C	0.37	-5.58	0.71706	147
CARB 67B	-4.84	-8.64	0.73854	148
CARB 52A	-6.7	-7.22	0.71056	180
CARB 52C	2.73	-7.06	0.71084	180
CARB 57B	-1.71	-6.17	0.71102	198

Table 3: C, O, Sr-isotope ratio values for veins. More data in the supplementary material.

The lack of observed prominent shelf-slope breaks in seismic profiles obtained in the southern São Francisco Craton and in the facies associations described in this study suggest that the accumulation of peritidal carbonates of the Nova América member occurred on an Ediacaran epeiric ramp (Martins-Neto, 2009; Caird et al. 2017).

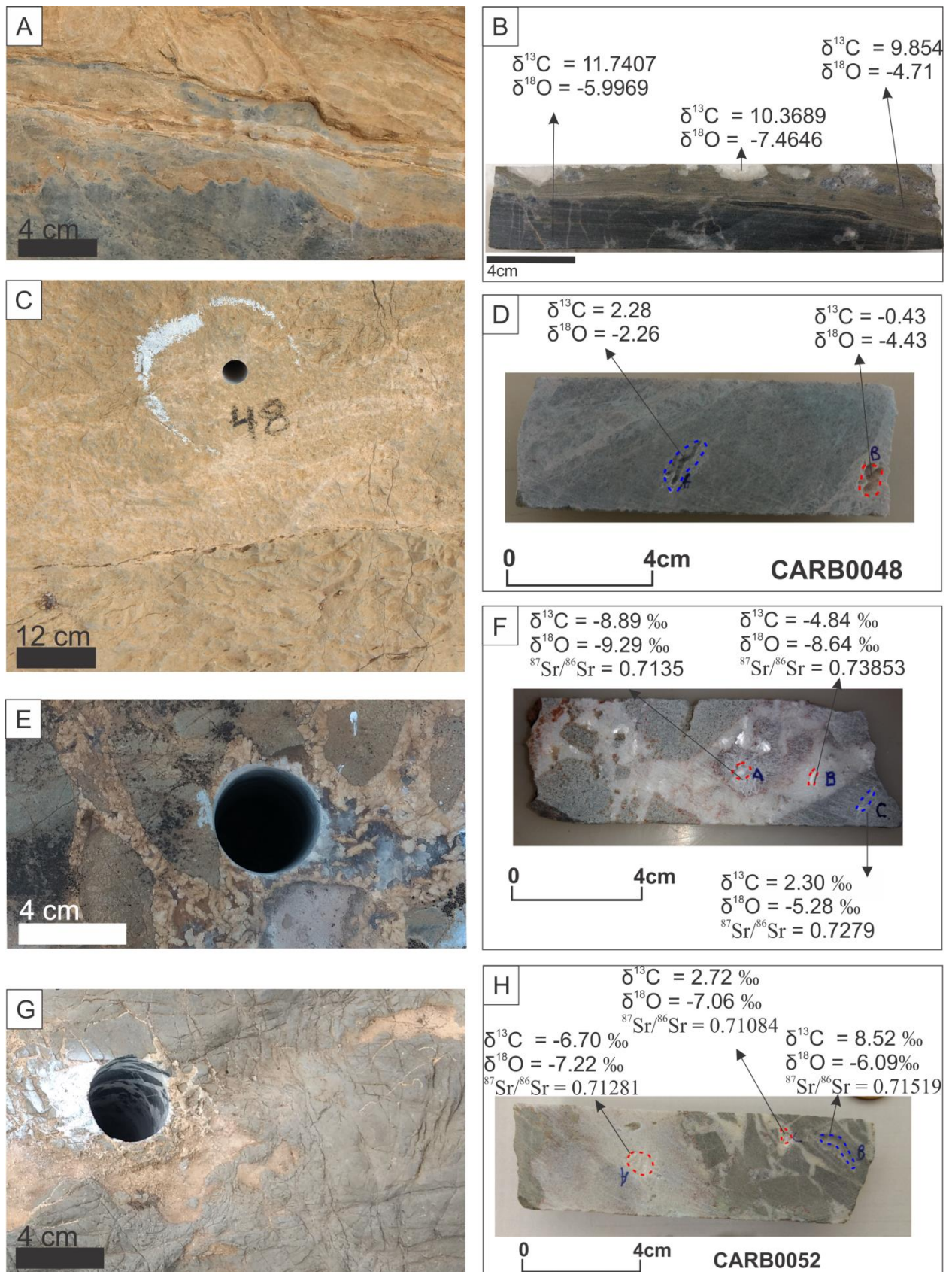


Figure 9: A) Major sinistral transpressional fault with sharp boundary surface; B) Plug sample from sinistral transpressional fault showing the sharp contact between facies and their isotopic values, as well as isotopic values for vugs filled by latter diagenetic mineral phases; C) cataclasite rock that occurs in F7; D) plug sample of cataclasite showing isotopic values of veins and host rock; E) hydraulic breccia that occurs in F7. F) plug sample of hydraulic breccia showing $\delta^{13}\text{C}$, $\delta^{18}\text{O}$ and ${}^{87}\text{Sr} / {}^{86}\text{Sr}$ values for the host rock and veins - Sample CARB 0067; G) hydraulic breccia that occurs in facies F12; H) plug sample of hydraulic breccia in F12 showing isotopic values of veins and host rock.

In the proposed depositional model, tidal processes dominated the proximal inner ramp. In the supratidal environment, sediments were deposited under arid conditions, as indicated by the occurrence of mud cracks, tepee structures and evaporite pseudomorphs. Microbial mats formed in the intertidal environment under mainly low-energy conditions while alternations between traction and suspension were responsible for the formation of the heterolithic bedding observed in some facies. The proximal condition is also evidenced by the amount of detrital sediments which occur in the rocks of FA1. Laterally toward the basin, changes in the hydraulic regime promoted wave action in the inner ramp and deposition of carbonate sand shoals. This high-energy environment favored the occurrence of columnar and dome stromatolites. Even further toward the center of the basin and below the fair-weather wave base, deposition of the FA3 facies indicated a higher-productivity environment that was represented by thrombolites with occasional storms.

The entire succession suggests a transgressive event which may be assessed by the increased occurrence of subtidal deposits from bottom to top. The facies stacking shows cyclic repetition throughout the succession. These cycles typically consist of subtidal deposits overlain by inter and supratidal sediments which form meter-thick shallowing-upward sequences. The shallowing-upward trend is represented by an overall facies change from the mid-ramp, through the inner ramp dominated by waves and to the inner ramp dominated by tidal processes.

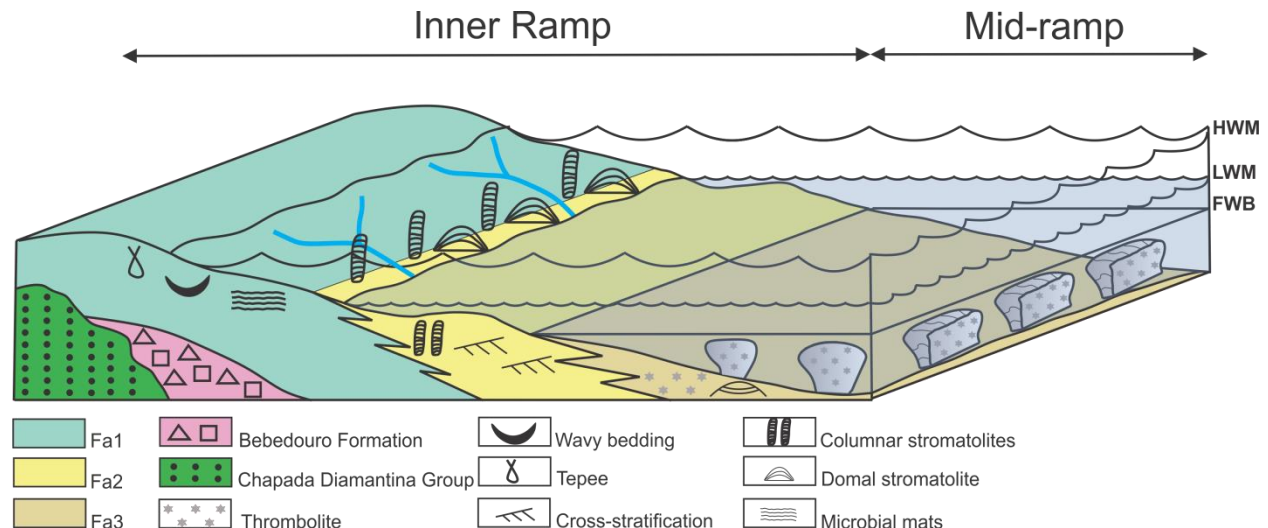


Figure 10: Depositional model for the Achado outcrop. FA1 is constituted of F1, F2, F3, F4 and F5, FA2 is composed of F6, F7, F8, F9 and F10. And FA3 is constituted of F11 and F12. High water mean (HWM) and Low Water Mean (LWM) mark the intertidal environment. Fair-weather base (FWB) marks the transition between the inner ramp and the mid-ramp.

2.5.2 Diagenesis

Diagenesis of the Salitre Formation in the studied section is interpreted to have occurred in six sequential stages (Figure 11).

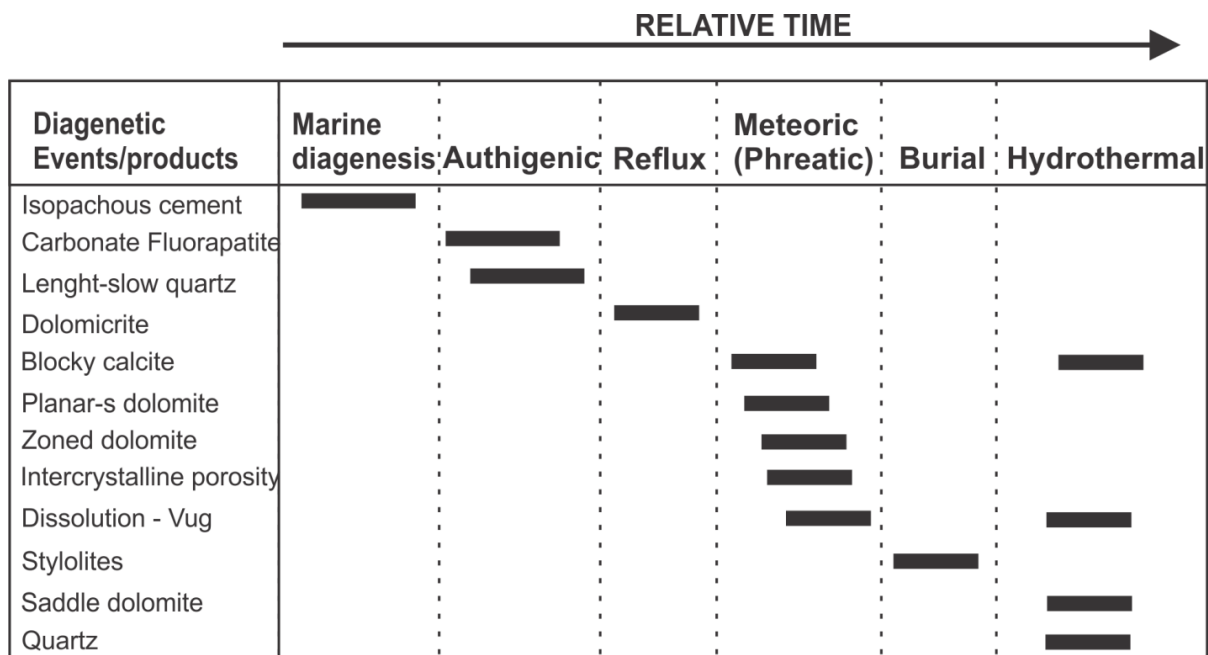


Figure 11: Simplified paragenetic sequence, in diagenetic phases, of the Achado outcrop.

Marine diagenesis

The first diagenetic stage after carbonate deposition in peritidal environment is characterized by marine diagenesis. The seafloor diagenesis is represented by dolomite-bladed isopachous rims around mesoclots that constitute thrombolites (Figure 6F). As stated by Hood and Wallace (2018), the Ediacaran seas were characterized by aragonite and high-Mg calcite seas, so the dolomite-bladed isopachous rims probably represent aragonite pseudomorphs.

Authigenesis

Authigenic mineral precipitation is characterized by nodules of radial length-slow quartz and blocky calcite (Figures 4B and 4C) which probably represent partial silicification of sulfate minerals (including gypsum and anhydrite) (Folk and Pittmann, 1971). The sulfate nodules in the lower section precipitated in the evaporitic supratidal/upper intertidal environment due to evaporation of pore waters. Precipitation of gypsum and anhydrite increased Mg/Ca ratios and removed sulfate (SO_4^{2-}) from pore waters and thus favored dolomitization (Warren, 2000). Dolomitization in this part of the succession was restricted to mud cracks and interbedding surfaces (Figure 4A) which were preferential paths for the dolomitizing fluids. Possible sources of fluids were the sinking of surface brines into the sediments (Warren, 2000) or through evaporative pumping where phreatic seawater flowed landward beneath the sabkha flat to replace groundwater lost by evaporation at or near the surface (Hsu and Scheneider, 1973). The lower section is dominated by limestones with $\delta^{13}\text{C}$ values approximately 0‰ and lower radiogenic strontium isotope values across the succession. We argue that these carbonates were deposited in a marine setting that was fully connected to an open sea.

The degradation of organic matter in the peritidal sediments resulted in release of phosphorus into the pore waters where authigenic precipitation or replacement by carbonate fluorapatite occurred (Misi and Kyle, 1994).

Reflux

Early dolomitization is interpreted to have occurred in the middle and upper sections by reflux dolomitization. Reflux dolomites form when hypersaline brines eventually become heavy enough to displace pore waters and seep slowly downward into the sediments (Adams and Rhodes, 1960; Warren, 2000). Hypersaline brines may form in platforms via tectonic controls on basin isolation. The occurrence of evaporite pseudomorph nodules and high $\delta^{13}\text{C}$ values (up to +13.69‰) in the middle and upper section represent a stage of basin restriction, as has been reported for other parts of the São Francisco Craton. (Santos et al., 2000; Vieira et al., 2007; Paula-Santos et al., 2015; 2017; Caxito et al., 2019).

This stage is characterized by replacement of calcium carbonate minerals by dolomicrite as the brines moved into the sediments while this feature is seen due to that dolomicrite that composed almost all of the allochems (Figure 6C) (e.g., ooids, peloids, and intraclasts). Early dolomitization was favored by the precipitation of sulfate minerals and CaCO_3 , which increased the brine density, Mg/Ca ratios, and salinity (Warren, 2000).

Meteoric diagenesis

Meteoric diagenesis is represented by planar-s dolomite and zoned dolomite in which both minerals have cloudy cores (characterized by calcite inclusions) but in the latter, the outer parts of the crystals shows clear rims (Figures 6B, 12A, 12C). Such features suggest cementation in a meteoric environment, probably in a mixing zone (Warren, 2000; Choquette and Hiatt, 2008). The complex zonation observed in the cathodoluminescence implies that these cements grew in ambient water whose chemistry changed more abruptly and/or more frequently and often represented mixtures of marine and meteoric waters (Figures 12B and 12D). The alternations of bright and dull zoned luminescence are attributed to varying Mn^{2+} and Fe^{2+} concentrations which are redox-sensitive and fluctuated in the shallow burial realm (Banner et al., 1988; Choquette and Hiatt, 2008). The vugs observed in the host rocks, which display nonfabric selective dissolution, are interpreted to have been formed at the same time as the precipitation of planar-s dolomite (Figure 7D) (Caird et al., 2017). Most of the observed porosity is intercrystalline and is present between dolomite crystals (Figure 7C). The evaporitic minerals are interpreted to have been replaced by blocky calcite in this stage (Figure 4G) (Caird et al., 2017).

Burial and Hydrothermal diagenesis

The widespread occurrence of stylolites parallel to laminations in the studied section indicates deep burial diagenesis (Figure 6E) (Misi and Kyle, 1994). The hydrothermal activity

was characterized by hydraulic breccia and veins that crosscut all of the diagenetic features. The veins are filled with saddle dolomite (Figures 6G, 6H and 12E), macrocrystalline calcite, and quartz and feature very negative $\delta^{18}\text{O}$ values. Saddle dolomite forms at elevated temperatures and is a useful geothermometer which indicates minimum burial temperatures of 60° to 150°C (Warren, 2000).

Under cathodoluminescence, saddle dolomite crystals display very bright red luminescence and internal zonation due to the varying iron and manganese contents (Figures 12F and 12H). Other research in the basin has reported the cooccurrence of saddle dolomite with sulfide minerals (e.g., pyrite, sphalerite, and galena), barite, quartz, gypsum, and in some instances, bitumen (Misi and Kyle, 1994; Kyle and Misi, 1997; Misi et al. 2005; Caird et al. 2017).

2.5.3 Isotopic interpretation

2.5.3.1 Carbon and oxygen isotopes

The isotope stratigraphy of Precambrian sedimentary rocks has been extensively used as a proxy for seawater chemistry, environmental conditions, stratigraphic correlations and sedimentary provenance (Halverson et al., 2010; Caxito et al., 2019). In this way, changes in $\delta^{13}\text{C}$ values are widely used as a proxy for understanding the global carbon cycle (Veizer et al., 1999; Zachos and Kump, 2005; Macdonald et al., 2010) as well as for local, regional and global stratigraphic correlations. Because bicarbonate-calcite carbon isotope fractionation does not vary much with temperature, carbon isotopes in carbonates that have precipitated from ocean water are generally considered to be reliable monitors of the C isotope compositions of ambient ocean waters (Frimmel, 2010) However, ancient carbonate rocks pose particular problems since the shallow-marine environments in which they were deposited have probably been influenced by meteoric diagenesis. Based mainly on the work of Allan and Matthews (1982), several workers have used the presence of a positive covariance between $\delta^{13}\text{C}$ and $\delta^{18}\text{O}$ values as evidence of alteration and the absence of such covariance as proof of the geochemical integrity of the rock (e.g., Fike et al., 2006; Grotzinger et al., 2011; Rose et al., 2012).

The interaction of carbonates with interstitial fluids during diagenesis and metamorphism frequently leads to increases in Mn/Sr, Fe/Sr, $^{87}\text{Rb}/^{86}\text{Sr}$, and $^{87}\text{Sr}/^{86}\text{Sr}$ ratios as well as decreases in $\delta^{18}\text{O}$ and $\delta^{13}\text{C}$ (Brand and Veizer, 1980; Banner and Hanson, 1990). The relationship between postsedimentary alteration and the maximum values of these parameters is mostly empirical. For example, $\delta^{13}\text{C}$ is likely to have remained effectively unaltered if Mn/Sr <2, Fe/Sr <50 and the

oxygen isotopic values are higher than -10‰ (VPDB) (Derry, et al., 1992; Jacobsen and Kaufman, 1999; Malezhik et al., 2001).

Carbon-isotope compositions are less affected by postdepositional alteration than $\delta^{18}\text{O}$ compositions because diagenetic and metamorphic fluids are typically aqueous and have relatively low carbon contents when compared to carbonate rocks (Frimmel, 2010).

The isotope data from our stratigraphic column corroborate the suggested complex diagenetic history (Figure 11). Carbon isotope levels from the lower section vary from -0.46‰ to +3.17‰ (Figure 2) which is within the range of the isotopic compositions of other primary Neoproterozoic limestones deposited in open ocean waters (Frimmel, 2010). The $\delta^{13}\text{C}$ vs. $\delta^{18}\text{O}$ plots show no positive correlations between C and O isotopes (Figures 13A and 13B) which suggests little or no alteration in the isotopic compositions during postdepositional modification (Grotzinger et al., 2011; Rose et al., 2012; Cui et al., 2018). Hence, we argue that the $\delta^{13}\text{C}$ values are primary and represent the original marine depositional environment. The $\delta^{18}\text{O}$ values in the lower section, with a mean value of -5.88‰, are consistent with the O-isotope values from a wide range of open marine carbonates in the Proterozoic (Kah, 2000; Kah et al., 2012).

The transition between the lower and middle sections also marks a shift from a limestone to dolostone dominated lithology. Across this transition, there is also an increase in the amplitude of the $\delta^{13}\text{C}$ values that reinforces the diagenetic imprint in the dolostones. Despite their amplitudes, the $\delta^{13}\text{C}$ values in the dolostone probably reflect the primary depositional signal. The upper part of the middle section also displays a positive $\delta^{13}\text{C}$ excursion in which the carbon isotope values increase from -3.41‰ to +8.85‰ (Figure 2). The carbon isotope values present large amplitudes in the remaining profile but persist as mostly highly positive values (up to +13.69‰) (Figure 2). The positive $\delta^{13}\text{C}$ excursion can be explained by various processes such as: increased burial rates of organic matter (Knoll et al., 1986); methane production associated with fermentation and a direct reduction in CO_2 (Whiticar et al., 1986); sulfate reduction accompanied by sulfide generation under anaerobic conditions (Claypool and Kaplan, 1974; Pierre, 1989); CO_2 evasion during evaporation; and high photosynthetic bioproductivity (Frimmel, 2010). Among the above processes, the occurrence of evaporite pseudomorphs in the upper section, which are filled with length-slow quartz and blocky calcite, suggests that evaporative conditions may have prevailed during the formation of these rocks.

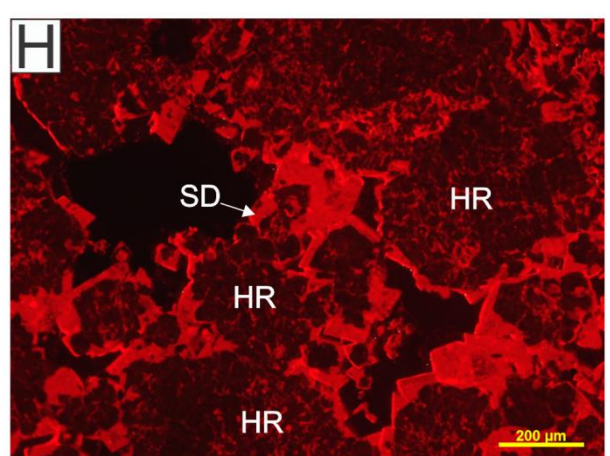
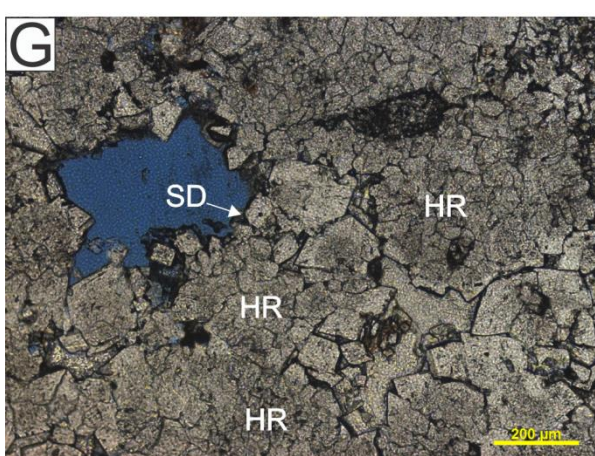
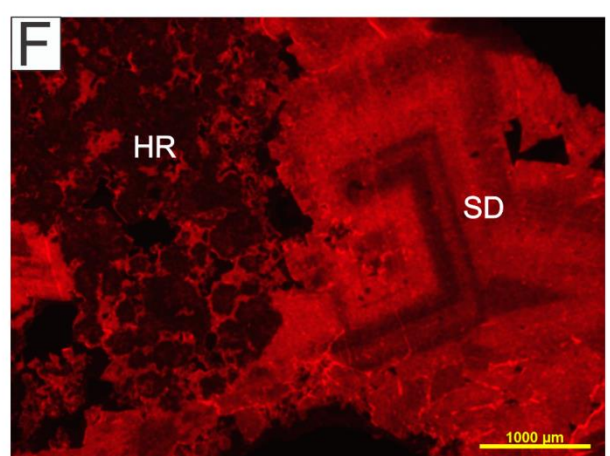
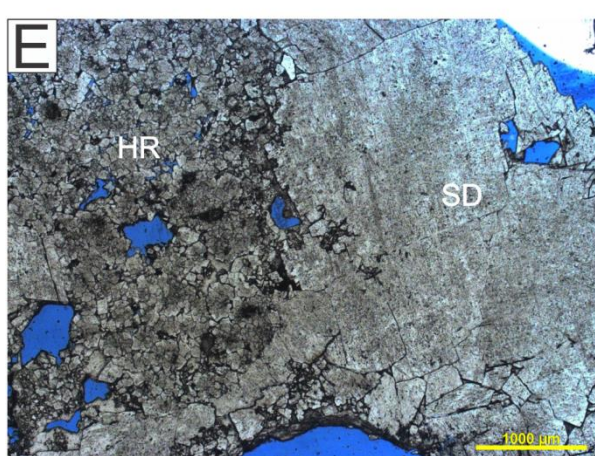
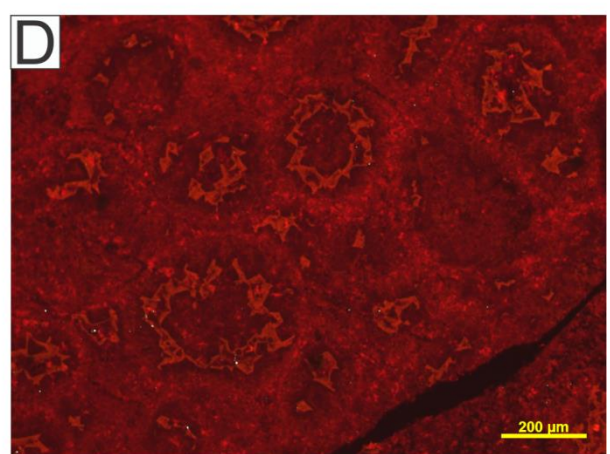
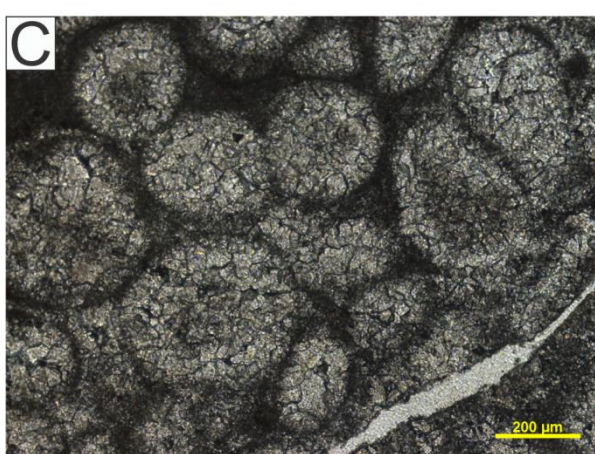
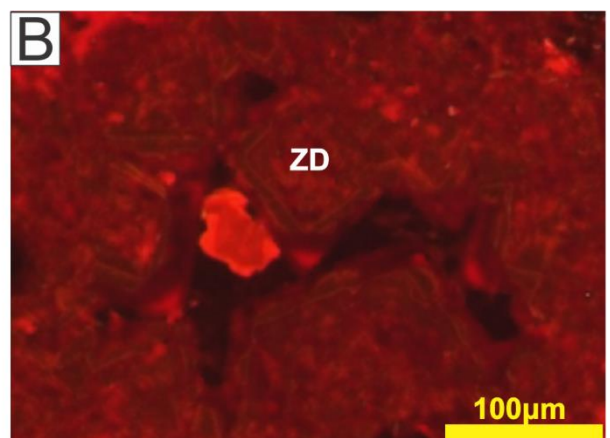
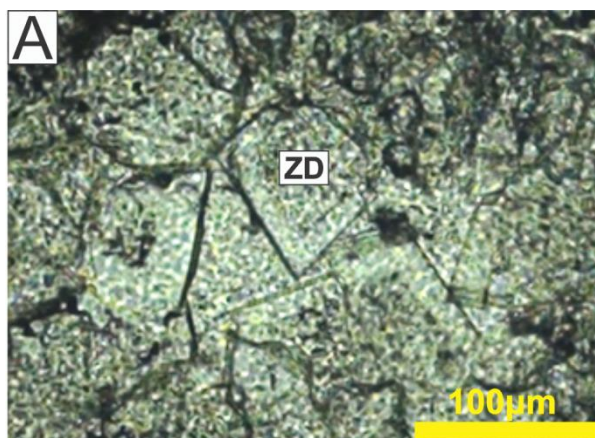


Figure 12: A) cloudy-core and limpid-rim zoned dolomite (ZD) PPL (plane polarized light) photomicrograph from Facies F3; B) Cathodoluminescence image of zoned dolomite, showing the alternation between dull red, bright red and dull yellow luminescence - Facies F7; C) ooids replaced with planar-s dolomite PPL photomicrograph - Facies F7; D) Cathodoluminescence image of ooids, showing alternation between yellow, dull red and bright red luminescence - Facies F7; E) PPL photomicrograph of the hydraulic breccia, showing on the left the host rock (HR), composed mainly of planar-s dolomite, and on the right the vein filled with saddle dolomite (SD) - sample CARB 0067; F) Cathodoluminescence image of the hydraulic breccia shows the host rock, on the left, displaying dull luminescence, while, on the other hand, saddle dolomite on veins shows very bright red zoned luminescence, saddle dolomite occurs between dull luminescent crystals that composed the host rock - CARB 0067; G) PPL photomicrograph of the host rock clasts from hydraulic breccia that occur in Facies 7 - CARB 0067; H) Cathodoluminescence image of host rock clast from hydraulic breccia showing bright red luminescence saddle dolomite as a cement - CARB 0067.

Heavier $\delta^{18}\text{O}$ values characterize the middle section interval (Figure 2), which may be consistent with evaporative conditions leading to ^{18}O enrichment. The increase in $\delta^{18}\text{O}$ values from the lower section to the middle section may be explained by isotope fractionation between dolomite and calcite, which means that dolomite crystals tended to be enriched in ^{18}O by 2.8‰ (Zhou and Zheng, 2006). However, the $\delta^{18}\text{O}$ difference between the middle and lower sections is too high to be explained only by isotope fractionation between carbonate minerals. The passage from the lower section to the middle section represents a stage of basin restriction in which isolation from the global ocean, which was associated with high evaporation rates, increased the $\delta^{18}\text{O}$ values. Inefficient circulation resulted in low oxygenation of deep waters which thus favored preservation of organic matter and enhanced burial of organic carbon which led to high $\delta^{13}\text{C}$ levels in the water column (Santos et al., 2000; Paula-Santos et al., 2017). The basin restriction was driven by the advances of orogenic fronts into the São Francisco Craton, as was reported for the São Francisco Basin (Paula-Santos et al., 2017; Uhlein et al., 2019). Thus, the middle and upper sections were deposited during periods of basin restriction. The transgressive event that was identified in the studied succession may be related to the advance of orogenic fronts toward the craton which created accommodation space in the foreland basin due to the increased orogenic load in the early stage of the Brasiliano orogeny.

A second hypothesis that explains the high $\delta^{18}\text{O}$ values observed in the host rock of the middle section (Figure 2) refers to fluid-rock interactions between the carbonate rocks and connate fluids. Previous studies have reported that interstitial fluids at greater burial depths exchange isotopes with the host rocks and produce higher $\delta^{18}\text{O}$ fluid values when compared to those from shallower regions (Teles et al., 2010). We argue that dolomite facies controlled the strain concentrations in this interval and promoted a highly permeable zone (Moore, 2013). The high density of fractures and brittle deformation observed in the middle section support this interpretation. Therefore, the middle section has the highest potential for fluid migration channeling of connate fluids from the deep parts of the basin. Once along the fault zone, these fluids spread laterally and promoted oxygen isotope fluid-rock exchange within the damaged zone. This interaction would explain the high $\delta^{18}\text{O}$ values that were observed in carbonates near the fault. In addition to a higher density of middle-zone fractures, the lower permeabilities of rocks in the lower and upper sections behaved as hydraulic barriers and further channelized the

fluids within the fractured grainstones. The fluid flow timing probably occurred after dolomitization and before the percolation of hydrothermal fluids because host-rock clasts with high $\delta^{18}\text{O}$ values are observed in the hydraulic breccia.

The lower section shows similar $\delta^{13}\text{C}$ values to those reported in other parts of the basin (Torquato and Misi, 1977; Misi and Veizer, 1998) and correlates with Unit B which overlies cap carbonates with a negative $\delta^{13}\text{C}$ excursion (Misi and Veizer, 1998). Due to a lack of radiogenic ages for the carbonates, it is difficult to correlate these cap carbonates in the context of the Neoproterozoic snowball events (Hoffman et al., 1998; Hoffman and Schrag, 2002) i.e., it is difficult to determine whether they are cap carbonates of Sturtian or Marinoan age.

2.5.3.2 *Sr Isotopes*

The $^{87}\text{Sr}/^{86}\text{Sr}$ variations in seawater track the relative input of riverine Sr derived from continental weathering and of Sr derived from hydrothermal sources (Halverson et al., 2010; Kuznetsov et al., 2012). As such, marine $^{87}\text{Sr}/^{86}\text{Sr}$ ratios are a useful measure of global scale changes in tectonics and climatic regimes.

The general trend of Neoproterozoic marine Sr isotope records shows that $^{87}\text{Sr}/^{86}\text{Sr}$ ratios increased from <0.7055 to >0.7080 toward the end of the era (Thomas et al., 2004; Shields, 2007; Halverson et al., 2007b). Such an increase in Sr isotope ratios has been used as a tool to establish the relative timing of deposition and for global stratigraphic correlations (Melezhik et al., 2001; Halverson et al., 2007; Halverson et al., 2010; Caxito et al., 2019).

In the lower section, macroscopic and petrographic data show little postdepositional dolomitization in carbonate rocks which suggests primary, little-affected $^{87}\text{Sr}/^{86}\text{Sr}$ ratios. $^{87}\text{Sr}/^{86}\text{Sr}$ ratios ranging from 0.70762 to 0.70818 are the least-radiogenic values for the entire succession (Figure 2) and these ratios may be interpreted as a marine Sr isotope record. When compared to the reference curves for the Sr isotope evolution of the Neoproterozoic, these ratios match those that are related to the Early Ediacaran Period which suggest sedimentation after the late Cryogenian glaciation (Misi and Veizer, 1998; Jacobsen and Kaufman, 1999; Halverson et al., 2010).

The middle and upper sections show very high radiogenic values for the $^{87}\text{Sr}/^{86}\text{Sr}$ ratios which range from 0.71039 to 0.71373 for the middle section and from 0.70885 to 0.71519 for the upper section (Figure 2). These values are very radiogenic and are incompatible with the Sr values expected for early Ediacaran seawater. As these sections consist of dolostone, the very radiogenic Sr values for the host rock represent a diagenetic alteration of the Sr ratios which means that the dolomitizing fluids were mainly derived from-modified seawater mixed with continental inputs (Jian et al., 2019) in the meteoric phreatic realm.

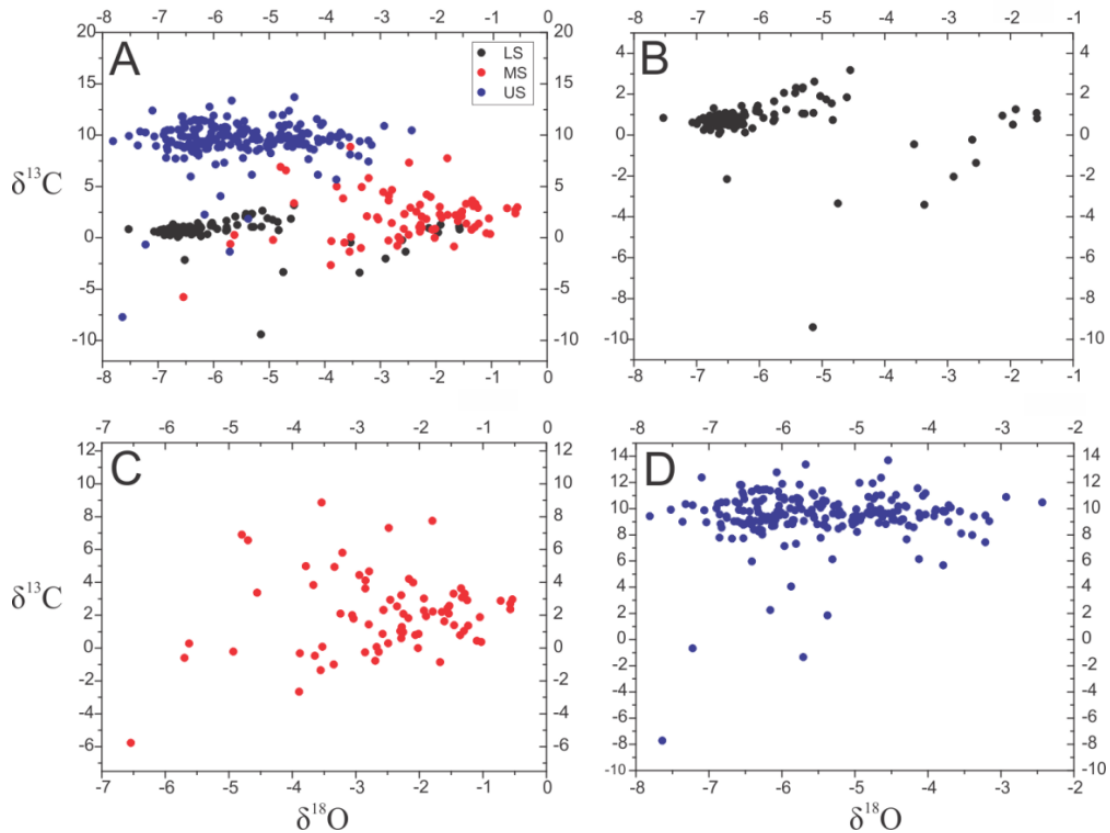


Figure 13: Cross plot of the C and O data shown in Fig. 2: A) all three sections; B) lower section; C) middle section; D) upper section. LS = lower sections, MS = middle section, US = upper section.

2.5.4 Fluid migration and fluid-rock interactions

In ancient carbonate rocks, fluid flows may be recorded in veins and rocks. The fluid sources and physicochemical conditions of these fluids may be evaluated through analyses of the minerals that fill the veins (Gomez et al., 2011). The petrophysical properties of carbonate rocks that control fluid flow are mainly porosity and permeability. Fractures are usually associated with increased permeability which allows for pervasive fluid circulation. In carbonate rocks, fluid flow may induce dissolution and precipitation within the fracture network and eventually lead to vein cementation (Dietrich et al., 1983; Barker et al., 2006). In this study, isotope geochemistry (C, O and Sr isotopes) was applied in veins and in the host rock to track fluid-rock interactions and fluid sources.

The entire succession presents fractures and veins but they are most concentrated in some parts of the middle and upper sections (F7 and F12 facies, respectively) and near the sinistral transpressional fault-damaged zone. In facies F7 and F12, we see the cross-cutting relationship between cataclasite, which is a fault rock, and hydraulic breccia in which the latter superimposes the former. Both have lateral continuity and are parallel to the bedding which is E-W oriented. The occurrence of cataclasite and deformed carbonates (Figure 9C and 9D) suggests the

occurrence of faults, which have the same direction as the thrust faults formed during the Brasiliano orogeny (Souza et al., 1993).

Faults can be excellent fluid conduits, especially those with considerable lateral and vertical connectivity (Moore, 2013). The fluids that were responsible for the formation of the hydraulic breccia probably migrated through the fault-damaged zone that is characterized by cataclasite. Isotopic analyses in the veins and secondary fills in the cataclasite (Figure 9D) show similar $\delta^{13}\text{C}$ values to those found in the host rock located at the lower section and in the bottom of the middle section (Figure 8) which suggest that the fluids that formed veins in the cataclasite were derived from pressure solution of these rocks during fault formation. The similar values indicate that the fluid-rock interaction occurred in a closed system.

The stable isotope values for the veins in the hydraulic breccia show very negative $\delta^{13}\text{C}$ (up to -8.89‰) and $\delta^{18}\text{O}$ (up to -9.29‰) values (Figures 8, 9F and 9H). These veins consist mainly of macrocrystalline calcite, saddle dolomite and quartz. For the same analyzed stratigraphic interval, metal sulfide occurrences have been reported (Misi and Kyle, 1994). These sulfide occurrences were interpreted as having formed due to thermochemical sulfate reduction (TSR) (Kyle and Misi, 1997). The highly depleted $\delta^{13}\text{C}$ values found in the veins of the hydraulic breccia suggest that the carbon had an organic source. Oxidation of organic matter by sulphates occurs during TSR and releases CO_2 which can form carbonate minerals with highly depleted $\delta^{13}\text{C}$ values. In addition, saddle dolomite may occur as a byproduct of TSR (Machel, 2001). Thus, the occurrence of sulfides in the same stratigraphic interval, negative $\delta^{13}\text{C}$ values, and mineral paragenesis suggest that the formation of these veins was a consequence of TSR.

The $^{87}\text{Sr}/^{86}\text{Sr}$ ratios found in the veins of the hydraulic breccia are very radiogenic (Figures 8, 9F and 9H) and are not related to the Sr isotope compositions of the late Neoproterozoic seawater (Halverson et al., 2010) or to meteoric diagenesis alterations. Thus, the fluid sources of for these veins may have been related to the heat released by intrusion of alkaline granites during the reactivation of basement structures (Misi et al., 2005). The sulfide deposits occur within NW-trending faults/fractures (Misi et al., 2005) and the hydraulic breccia occurs cross-cutting the cataclasite which is related to a thrust fault with an E-W direction. We suggest that these structures were connected during fluid migration from the basement and that the cataclasite/faults were the conduit for fluid flow (Figure 14). Facies control was important for the lateral fluid migration, mainly in the middle section, where it is observed that late diagenetic fluids with bright red luminescence (Figures 12E, 12F 12G and 12H) percolated through the host rock and precipitated in cavities due to the high porosity and permeability of the host rock. The $^{87}\text{Sr}/^{86}\text{Sr}$ isotope values in the host rock near the contact with hydrothermal veins show very radiogenic $^{87}\text{Sr}/^{86}\text{Sr}$ values (Figure 9F) when compared to the Sr ratios of the entire section

(Figure 2) and these high values are due to fluid-rock interactions, as Sr is a trace element in carbonates and is more susceptible to changes in its isotopic composition. The low $\delta^{18}\text{O}$ values in the veins are interpreted as a consequence of precipitation at hydrothermal temperatures (O’Neil and Epstein, 1966; Warren, 2000). In the host rock near the contacts with veins, the $\delta^{18}\text{O}$ values are more negative when compared to host rocks that are located far from the veins at the same interval, so the high temperature and the aqueous nature of the fluid were responsible for these negative $\delta^{18}\text{O}$ values. The differences in isotope compositions and petrographic features of the veins and host rock suggest that the fluids which precipitated in fractures represent an external source of fluids and that fluid-rock interactions occurred in an open system, which caused changes in the isotopic composition of the host rock. Secondary porosity was formed due to the interactions of these hydrothermal fluids with the host rock and vugs were formed close to the contact between the veins and host rock (Figures 7A and 7B).

The veins and fills near the transpressional fault in the upper section show very similar $\delta^{13}\text{C}$ isotope values compared to the host rock and more negative $\delta^{18}\text{O}$ values (Figure 8 and 9B). The similar $\delta^{13}\text{C}$ values for the veins and host rock indicate the same carbon source for both, so we suggest that these veins represent dissolution and precipitation events of the host rocks due to the deformation that was related to the kinematics of the sinistral transpressional fault and to fluid-rock interactions occurring in a closed system.

The integrated study involving facies analysis, diagenesis and isotope geochemistry of the studied carbonate succession of the Salitre Formation is useful for identifying the main fluid-flow zones, origins of these fluids, and isotope signatures resulting from fluid-rock interactions.

Identification of preferential sites for fluid migration in carbonate systems is crucial since such fluids may cause positive or negative effects with respect to the quality of carbonate reservoirs. They may promote dissolution and/or precipitation of minerals in cavities which can lead to increased or decreased porosity and permeability (Giles and Marshall, 1986; Biehl et al., 2016).

Paleoenvironmental and diagenetic conditions were essential for establishing fluid flow in the studied succession. The dolomitization that was observed when the basin was still connected to the ocean was localized. When the basin became restricted, the dolomitization was more pervasive, as is observed in the middle and upper sections. More effective dolomitization processes may be accompanied by increased porosity (Warren, 2000; Wang et al., 2015) as well as by fracture development since dolomites are more brittle than limestones (Moore, 2013). The most widespread dolomitization stage took place during meteoric diagenesis which was responsible for altering the Sr ratios to more radiogenic values. It is likely that there was lithological control over the distribution of faults and fractures along the succession with the

middle section being more fractured and thus allowing preferential fluid flow. The facies controls were fundamental for the lateral fluid migration in the middle section.

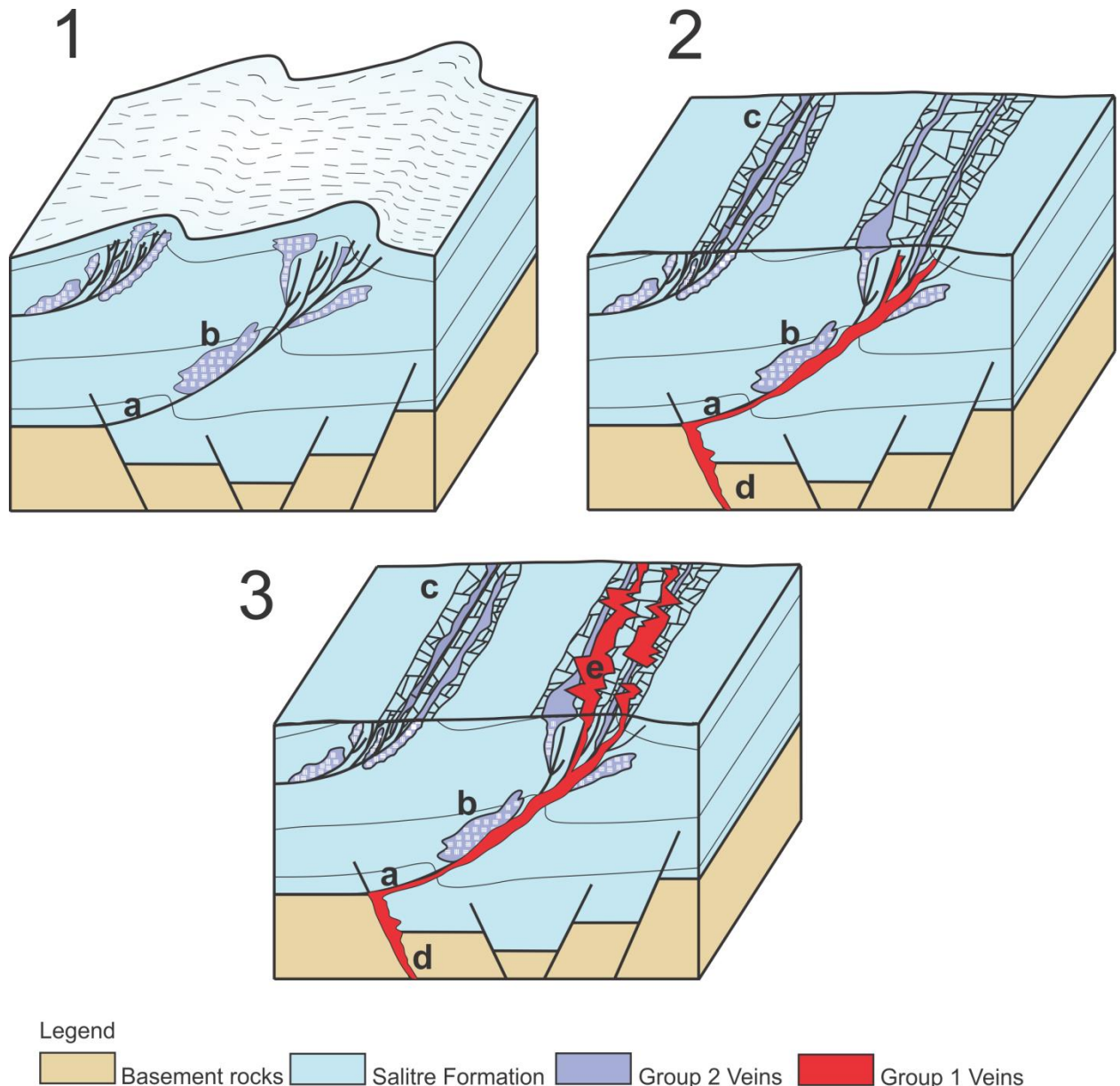


Figure 14: Block diagram showing the fault evolution and vein formation. 1) thrust fault formation (a) and veins of group 2 formed through pressure solution mechanisms (B). 2) Cataclasite formation (c) and fluid migration from the reactivation of basement structures (d). 3) Formation of the hydraulic breccia and group 1 veins due to the fluid migrated through basement structures (e).

The veins that constitute the hydraulic breccia formed in an open system due to the migration of hydrothermal fluids. These veins are characterized by very negative $\delta^{13}\text{C}$ values which signify organic carbon as the source for these carbonate veins and negative $\delta^{18}\text{O}$ values which indicate high temperatures. The extremely radiogenic Sr ratios suggest that these veins represented an external source for the fluids which migrated due to the reactivation of basement structures. Fluid-rock interactions caused isotopic changes in the host rock to more negative $\delta^{18}\text{O}$ values and to more radiogenic Sr values. This is an example of how isotopes may be used as tracers for fluid-rock interactions and may be used as a tool for predicting fluid-flow zones. The isotope analyses also made it possible to determine that the veins located near the sinistral

transpressional fault damaged zone formed in a closed system as a result of fluid-rock interactions through a pressure-solution mechanism. The similar $\delta^{13}\text{C}$ and $\delta^{18}\text{O}$ values for the veins and host rock support this interpretation.

2.6 CONCLUSION

A multidisciplinary study involving facies analysis, diagenesis and well as isotope geochemistry is presented for the Neoproterozoic carbonates of the Salitre Formation outcropping near Irecê, Bahia. This area is an ideal site to investigate strategies and procedures to better understand the history of fluid flow in complex carbonate systems.

Detailed analysis of sedimentary facies characteristics indicate that the studied succession consists of twelve major lithofacies types which are grouped into three facies associations which represent a carbonate ramp system: an (FA1) inner carbonate ramp dominated by tidal process and microbialites, (FA2) an inner carbonate ramp dominated by waves and (FA3) a middle carbonate ramp dominated by storm waves. The entire succession suggests a transgressive event which can be evaluated by the increased subtidal deposits from the bottom to top.

The $\delta^{13}\text{C}$ isotope values in the host rock are probably primary and are related to the paleoenvironmental conditions during deposition and reflect different stages of basin evolution. The $\delta^{13}\text{C}$ values ranging from $-0.46\text{\textperthousand}$ to $+3.17\text{\textperthousand}$ in the lower section are similar to the isotopic composition of the Neoproterozoic open ocean and are related to the deposition that took place at the time when the basin was connected to the open ocean. The positive $\delta^{13}\text{C}$ excursion of up to $+13.69\text{\textperthousand}$ observed in the upper section was related to basin restriction which meant inefficient circulation and favored burial of organic carbon.

Diagenesis in the studied section is complex and has recorded multiple dolomitization and hydrothermal events. Meteoric diagenesis altered the $^{87}\text{Sr}/^{86}\text{Sr}$ ratios to more radiogenic values which suggest a continental input of radiogenic Sr by dolomitizing fluids.

The paleoenvironmental and diagenetic conditions were fundamental to establishing fluid flow in the studied carbonate succession. It is likely that there was lithological control of the distribution of faults and fractures along the succession with the middle section being more fractured which allowed for preferential fluid flow. The facies controls were important for lateral fluid migration in this section.

Two groups of veins were identified in the study area based on their isotope signatures; one was related to the formation of hydraulic breccia and the other occurred close to a sinistral transpressional fault. Veins in the hydraulic breccia have more negative $\delta^{13}\text{C}$ values which suggest incorporation of organic carbon, probably due to TSR, and the more negative values of

$\delta^{18}\text{O}$ suggest formation at high temperatures. These veins have extremely radiogenic $^{87}\text{Sr}/^{86}\text{Sr}$ ratios (up to 0.73854) which suggest an external fluid source which was probably due to reactivation of basement structures. Near these veins, the host rock shows more radiogenic $^{87}\text{Sr}/^{86}\text{Sr}$ values and more negative $\delta^{18}\text{O}$ values which indicate isotopic alterations due to fluid-rock interactions.

Veins located near the sinistral transpressional fault damaged zone formed in a closed system as a result of fluid-rock interactions through a pressure-solution mechanism. Similar values of $\delta^{13}\text{C}$ and $\delta^{18}\text{O}$ for the veins and host rock support this interpretation.

In conclusion, by using a multidisciplinary approach, we provide evidence that fluid-rock interactions and carbonate reservoir-quality modifications are primarily controlled by the facies and tectonic features. The facies exert important controls on the intensity and propagation of faults and fractures which are used for fluid migration. In addition, they control the lateral distribution of these fluids from the conduits. The integrated study involving facies analysis, diagenesis and the isotope geochemistry was useful to identify the main fluid flow zones, origin of these fluids, and isotope signatures resulting from fluid-rock interactions.

2.7 ACKNOWLEDGEMENTS

This research was carried out in association with the ongoing R&D Project registered as ANP 20502-1, “Processos e Propriedades em Reservatórios Carbonáticos Fraturados e Carstificados – POROCARSTE 3D” (UFRN/ UnB / UFRJ / UFC / Shell Brasil / ANP) – PoroKarst – Processes and Properties in Fractured and Karstified Carbonate Reservoirs, sponsored by Shell Brasil under the ANP R&D levy as “Compromisso de Investimentos com Pesquisa e Desenvolvimento”. This study was financed in part by the Coordenação de Aperfeiçoamento de Pessoal de Nível Superior – Brasil (CAPES) – Finance Code 001.

3 REFERÊNCIAS BIBLIOGRÁFICAS

- Adams, J.F., Rhodes, M.L., 1960. Dolomitization by seepage refluxion. Am. Assoc. Petrol. Geol. Bull. 44, 1912–1920.
- Agosta, F., Alessandroni, M., Antonellini, M., Tondi, E., & Giorgioni, M., 2010. From fractures to flow: A field-based quantitative analysis of an outcropping carbonate reservoir. *Tectonophysics*, 490, 197-213.
- Alkmim, F. D. 2004. O que faz de um cráton um cráton? O Cráton do São Francisco e as revelações almeidianas ao delimitá-lo. *Geologia do continente Sul-Americanoo: evolução da obra de Fernando Flávio Marques de Almeida*, 17-34.
- Alkmim, F. F., & Martins-Neto, M. A. 2012. Proterozoic first-order sedimentary sequences of the São Francisco craton, eastern Brazil. *Marine and Petroleum Geology*, 33, 127-139.
- Alkmim, F. F., Chemale Jr, F., & Endo, I., 1996. A deformação das coberturas proterozóicas do Cráton do São Francisco e o seu significado tectônico. *Revista da escola de Minas*, 49, 22-38.
- Alkmim, F. F., Marshak, S., & Fonseca, M. A. 2001. Assembling West Gondwana in the Neoproterozoic: clues from the São Francisco craton region, Brazil. *Geology*, 29, 319-322.
- Alkmim, F.F., Marshak, S., Pedrosa-Soares, A.C., Peres, G.G., Cruz, S., Whittington, A. 2006. Kinematic evolution of the Araçuaí-West Congo orogen in Brazil and Africa: Nutcracker tectonics during the Neoproterozoic assembly of Gondwana. *Precambrian Research*, 149, 43–64.
- Allan, J. R., & Matthews, R. K., 1982. Isotope signatures associated with early meteoric diagenesis. *Sedimentology*, 29, 797-817.
- Almeida FF. 1977. O Cráton do São Francisco. *Rev Bras Geocienc*, 4, 349–364.
- Almeida, F. F. M. 1967 Origem e Evolução da Plataforma Brasileira. Rio de Janeiro, DNPM/DGM. 96 p. (Boletim 241).
- Babinski, M., Brito-Neves, B.B., Machado, N., Noce, C.M., Ulhein, A., Van Schumus, W.R. 1994. Problemas na metodologia U/Pb em zircões de vulcânicas continentais: o caso do Grupo Rio dos Remédios, Supergrupo Espinhaço, no estado da Bahia. XXXVIII Congresso Brasileiro de Geologia, Boletim de Resumos Expandidos, v.2, p. 409–410.
- Babinski, M., Pedreira, A., Brito-Neves, B.B., Van-Schmus, W.R. 1999. Contribuição à geocronologia da Chapada Diamantina. 7º Simpósio Nacional de Estudos Tectônicos, Anais, p. 118–121.
- Babinski, M., Vieira, L. C., & Trindade, R. I. 2007. Direct dating of the Sete Lagoas cap carbonate (Bambuí Group, Brazil) and implications for the Neoproterozoic glacial events. *Terra Nova*, 19, 401-406.

Banner, J. L., & Hanson, G. N. 1990. Calculation of simultaneous isotopic and trace element variations during water-rock interaction with applications to carbonate diagenesis. *Geochimica et Cosmochimica Acta*, 54, 3123-3137.

Banner, J. L., & Hanson, G. N., 1990. Calculation of simultaneous isotopic and trace element variations during water-rock interaction with applications to carbonate diagenesis. *Geochimica et Cosmochimica Acta*, 54, 3123-3137.

Banner, J.L., Hanson, G.N. & M Eyers, W.J. 1988. Water-rock-interaction history of regionally extensive dolomites of the Burlington-Keokuk Formation (Mississippian): isotopic evidence. In Shukla, V.J. & Baker, P.A., eds., *Sedimentology and geochemistry of dolostones: SEPM Spec. Publ.* 43, 129–144.

Barbosa, J. S. F., & Sabaté, P. 2004. Archean and Paleoproterozoic crust of the São Francisco craton, Bahia, Brazil: geodynamic features. *Precambrian Research*, 133, 1-27.

Barker, S. L., Cox, S. F., Egginis, S. M., & Gagan, M. K., 2006. Microchemical evidence for episodic growth of antitaxial veins during fracture-controlled fluid flow. *Earth and Planetary Science Letters*, 250, 331-344.

Becker, A., & Gross, M. R. 1996. Mechanism for joint saturation in mechanically layered rocks: an example from southern Israel. *Tectonophysics*, 257, 223-237.

Biehl, B. C., Reuning, L., Schoenherr, J., Lewin, A., Leupold, M., & Kukla, P. A. 2016. Do CO₂-charged fluids contribute to secondary porosity creation in deeply buried carbonates?. *Marine and Petroleum Geology*, 76, 176-186.

Bjørlykke, K. 1983. Diagenetic reactions in sandstones. In *Sediment diagenesis* pp. 169-213. Springer, Dordrecht.

Bjørlykke, K. 1994. Fluid-flow processes and diagenesis in sedimentary basins. Geological Society, London, Special Publications, 78, 127-140.

Bjørlykke, K., & Høeg, K. 1997. Effects of burial diagenesis on stresses, compaction and fluid flow in sedimentary basins. *Marine and Petroleum Geology*, 14, 267-276.

Bomfim, L.F.C.; Rocha, A.J.D.; Pedreira, A.J.; Morais, J.C., P; Guimarães, J.T.; Tesch, N.A. 1985. Projeto Bacia de Irecê. Salvador, CPRM. (Relatório Final).

Brand, U., & Veizer, J., 1980. Chemical diagenesis of a multicomponent carbonate system; 1, Trace elements. *Journal of Sedimentary Research*, 50, 1219-1236.

Brito Neves, B. B., Fuck, R.A., Pimentel, M.M., 2014. The Brasiliano collage in South America: a review. *Braz. J. Genet.* 44, 493-518.

Caird, R. A., Pufahl, P. K., Hiatt, E. E., Abram, M. B., Rocha, A. J. D., & Kyser, T. K. 2017. Ediacaran stromatolites and intertidal phosphorite of the Salitre Formation, Brazil: Phosphogenesis during the Neoproterozoic Oxygenation Event. *Sedimentary Geology*, 350, 55-71.

- Caxito, F. D. A., Uhlein, G. J. Uhlein, A., Pedrosa-Soares, A. C., Kuchenbecker, M., Reis, H. & Vieira, L. C., 2019. Isotope stratigraphy of Precambrian sedimentary rocks from Brazil: Keys to unlock Earth's hydrosphere, biosphere, tectonic, and climate evolution. In *Stratigraphy & Timescales* (Vol. 4, pp. 73-132). Academic Press.
- Chemale Jr., F., Dussin, I.A., Alkmim, F.F., Martins, M.S., Queiroga, G., Armstrong, R., Santos, M.N., 2012. Unravelling a Proterozoic basin history through detrital zircon geochronology: the case of the Espinhaço Supergroup, Minas Gerais, Brazil. *Gondwana Research* 22, 200–206.
- Chen, Y. H., Liu, Y., & Sun, S. 1985. Change for pore volume in dolomitization. *Exp. Pet. Geol*, 7, 29-37.
- Choquette, P. W., & Hiatt, E. E. 2008. Shallow-burial dolomite cement: a major component of many ancient sucrosic dolomites. *Sedimentology*, 55, 423-460.
- Choquette, P. W., and N. P. James, 1990, Limestones: The burial diagenetic environment, in I. E. McIlreath and D. A. Morrow, eds., *Diagenesis*: Geological Association of Canada, Geoscience Canada Reprint Series 4, p. 75–112.
- Choquette, P. W., Pray, L.C. 1970, Geologic nomenclature and classification of porosity in sedimentary carbonates: AAPG Bulletin 54, 207–244.
- Claypool, G. E., & Kaplan, I. R., 1974. The origin and distribution of methane in marine sediments. In *Natural gases in marine sediments*, pp. 99-139. Springer, Boston, MA.
- Clayton, J. L., Spencer, C. W., Koncz, I., & Szalay, A. 1990. Origin and migration of hydrocarbon gases and carbon dioxide, Békes Basin, southeastern Hungary. *Organic Geochemistry*, 15, 233-247.
- Cooke, M. L., Simo, J. A., Underwood, C. A., & Rijken, P. 2006. Mechanical stratigraphic controls on fracture patterns within carbonates and implications for groundwater flow. *Sedimentary Geology*, 184(3-4), 225-239.
- Craig, H., 1957. Isotopic standards for carbon and oxygen and correction factors for massspectrometric analysis of carbon dioxide. *Geochimica et Cosmochimica Acta* 12, 133–149.
- Cruz, S. C. P., & Alkmim, F. F., 2017. The Paramirim Aulacogen. In *São Francisco Craton, Eastern Brazil* (pp. 97-115). Springer, Cham.
- Cruz, S. C., & Alkmim, F. F. 2006. The tectonic interaction between the Paramirim Aulacogen and the Araçuaí belt, São Francisco craton region, Eastern Brazil. *Anais da Academia Brasileira de Ciências*, 78, 151-173.
- Cui, H., Kaufman, A. J., Peng, Y., Liu, X. M., Plummer, R. E., & Lee, E. I., 2018. The Neoproterozoic Hüttenberg $\delta^{13}\text{C}$ anomaly: Genesis and global implications. *Precambrian Research*, 313, 242-262.
- Danderfer, A., De Waele, B., Pedreira, A.J., Nalini, H.A., 2009. New geochronological constraints on the geological evolution of Espinhaço basin within the São Francisco Craton—Brazil. *Precambrian Research*, 170, 116–128.
- Derry, L.A., Kaufman, A.J., Jacobsen, S.B., 1992. Sedimentary cycling in the Late Proterozoic: evidence from stable and radiogenic isotopes. *Geochimica et Cosmochimica Acta* ,56, 2331–2339.

Dickson, J.A.D., 1966. Carbonate identification and diagenesis as revealed by Staining. *Journal of Sedimentary Petrology* 36, 491-505.

Dietrich, D., McKenzie, J.A., Song, H., 1983. Origin of calcite in syntectonic veins as determined from carbon-isotope ratios. *Geology*, 11, 547- 551 .

Dominguez, J.M.L. 1993. As coberturas do Cráton do São Francisco: uma abordagem do ponto de vista da análise de bacias. Em: Dominguez, J.M.L.; Misi, A. (Eds). O Cráton do São Francisco. Salvador. SBG, p. 137-159.

Dongjie, T., Xiaoying, S., Ganqing, J., Yunpeng, P., Wenhao, Z., Yuan, W., & Min, L. 2013. Environment controls on Mesoproterozoic thrombolite morphogenesis: a case study from the North China Platform. *Journal of palaeogeography*, 2(3), 275-296.

Dunham, R.J. 1962. Classification of carbonate rocks according to depositional texture. In; HAM, W.E. ed., Classification of carbonates rocks. Amer, Assoc. Petrol. Geol. p. 108-121 (Memoir I).

Fabrizio, A., Mulch, A., Chamberlain, P., & Aydin, A., 2008. Geochemical traces of CO₂-rich fluid flow along normal faults in central Italy. *Geophysical Journal International*, 174, 758-770.

Figueiredo, F.T. 2008. Fácies sedimentares e proveniência da Formação Bebedouro, Neoproterozóico (BA). Dissertação de Mestrado, Instituto de Geociências, Universidade de São Paulo, São Paulo, (121 p).

Fike, D. A., Grotzinger, J. P., Pratt, L. M., & Summons, R. E., 2006. Oxidation of the Ediacaran ocean. *nature*, 444(7120), 744-747.

Flügel, E. 2010. Microfacies of Carbonate Rocks. London, Springer, 1006 p.

Folk, R. L., & Pittman, J. S. 1971. Length-slow chalcedony; a new testament for vanished evaporites. *Journal of Sedimentary Research*, 41, 1045-1058.

Fölling, P. G., & Frimmel, H. E., 2002. Chemostratigraphic correlation of carbonate successions in the Gariep and Saldania Belts, Namibia and South Africa. *Basin Research*, 14, 69-88.

Frimmel, H. E. 2010. On the reliability of stable carbon isotopes for Neoproterozoic chemostratigraphic correlation. *Precambrian Research*, 182, 239-253.

Giles, M. R., & Marshall, J. D. 1986. Constraints on the development of secondary porosity in the subsurface: re-evaluation of processes. *Marine and Petroleum Geology*, 3, 243-255.

Gómez, J. C., Figueroa, L. C. M., Vesga, J. N., 2011. Fluid migration history from analysis of filling fractures in a carbonate formation: (lower cretaceous, middle magdalena valley basin, Colombia). *CT&F-Ciencia, Tecnología y Futuro*, 4, 21-36.

Grotzinger, J. P., Fike, D. A., & Fischer, W. W., 2011. Enigmatic origin of the largest-known carbon isotope excursion in Earth's history. *Nature Geoscience*, 4(5), 285-292.

Guadagnin, F. and Chemale Jr. F. 2015. Detrital zircon record of the Paleoproterozoic to Mesoproterozoic cratonic basins in the SãoFrancisco Craton. *Journal of South American Earth Sciences*, 60, 104–116.

Guimarães, J. T. 1996. A Formação Bebedouro no Estado da Bahia; faciologia, estratigrafia e ambientes de sedimentação. Dissertacão (Mestrado em Geologia), Instituto de Geociências, Universidade Federal da Bahia (UFBA), Brasil.

Guimarães J.T.; Santos R.A.S.; Melo R.C. (Orgs.). 2008. Geologia da Chapada Diamantina Ocidental. In: Guimarães J.T., Santos R.A., Melo R.C. Projeto Ibitiara – Rio de Contas. Companhia Baiana de Pesquisa Mineral-CBPM, Salvador, Arquivos Abertos 31, 64 p.

Guimaraes, J. T., Misi, A., Pedreira, A. J. & Dominguez, J. M. L. 2011. The Bebedouro Formation, Una Group, Bahia (Brazil). *Geological Society, London, Memoirs*, 36, 503-508.

Guimarães, J.T. 2005. Projeto Ibitiara - Rio de Contas. Salvador: CPRM & CBPM, p. 182, 2005.

Guimarães, J.T., Alkmim, F.F., Cruz, S.C.P. 2012. Supergrupos Espinhaço e São Francisco. In: Barbosa, J.S.F., Mascarenhas, J.F. M., Corrêa-Gomes, L.C., Domingues, J.M.L. (eds.). *Geologia da Bahia. Pesquisa e Atualização de Dados*. Salvador, Companhia Baiana de Pesquisa Mineral-CBPM, v. 2, p. 33–86.

Halverson, G. P., Dudás, F. Ö., Maloof, A. C., & Bowring, S. A., 2007. Evolution of the $^{87}\text{Sr}/^{86}\text{Sr}$ composition of Neoproterozoic seawater. *Palaeogeography, Palaeoclimatology, Palaeoecology*, 256, 103-129.

Halverson, G. P., Hoffman, P. F., Schrag, D. P., Maloof, A. C., & Rice, A. H. N. 2005. Toward a Neoproterozoic composite carbon-isotope record. *GSA Bulletin*, 117, 1181-1207.

Halverson, G. P., Wade, B. P., Hurtgen, M. T., & Barovich, K. M., 2010. Neoproterozoic chemostratigraphy. *Precambrian Research*, 182, 337-350.

Hanks, C. L., Lorenz, J., Teufel, L., & Krumhardt, A. P. 1997. Lithologic and structural controls on natural fracture distribution and behavior within the Lisburne Group, northeastern Brooks Range and North Slope subsurface, Alaska. *AAPG bulletin*, 81, 1700-1720.

Hoffman, P. F., & Schrag, D. P., 2002. The snowball Earth hypothesis: testing the limits of global change. *Terra nova*, 14, 129-155.

Hoffman, P.F., Kaufman, A.J., Halverson, G.P., 1998b. A Neoproterozoic snowball Earth. *Science*, 281, 1342–1346.

Hood, A.V.S., Wallace, M.W., 2018. Neoproterozoic marine carbonates and their paleoceanographic significance. *Global and Planetary Change* 160, 28–45.

Hsü, K. J., & Schneider, J. 1973. Progress report on dolomitization—hydrology of Abu Dhabi sabkhas, Arabian Gulf. In *The Persian Gulf* pp. 409-422. Springer, Berlin, Heidelberg.

Jacobsen, S.B., Kaufman, A.J., 1999. The Sr, C and O isotopic evolution of Neoproterozoic seawater. *Chemical Geology* ,161, 37–57.

Jiang, L., Worden, R. H., & Yang, C. 2018. Thermochemical sulphate reduction can improve carbonate petroleum reservoir quality. *Geochimica et Cosmochimica Acta*, 223, 127-140.

Jiang, W., Hou, M., & Wang, C., 2019. Strontium isotopic compositions of Cambrian (Upper Miaolingian–Furongian Series) dolomites from south-eastern Sichuan Basin, China: Significance of sources of dolomitizing fluids and timing of dolomitization. *Marine and Petroleum Geology*, 109, 408-418.

Kah, L.C., 2000. Depositional $\delta^{18}\text{O}$ signatures in Proterozoic dolostones: constraints on seawater chemistry and early diagenesis. In: Grotzinger, J.P., James, N.P. (Eds.), *Carbonate Sedimentation and Diagenesis in the Evolution Precambrian World*. SEPM, Special Publications ,67, pp. 345–360.

Kah, L.C., Bartley, J.K., Teal, D.A., 2012. Chemostratigraphy of the Late Mesoproterozoic Atar Group, Taoudeni Basin, Mauritania: muted isotopic variability, facies correlations, and global isotopic trends. *Precambrian Res.* 200–203, 82–103.

Kah, L.C., Lyons, T.W., Chesley, J.T., 2001. Geochemistry of a 1.2 Ga carbonate-evaporite succession, northern Baffin and Bylot Island: implications for Mesoproterozoic marine evolution. *Precambrian Res.* 111, 203–234.

Kaufman, A. J., & Knoll, A. H. 1995. Neoproterozoic variations in the C-isotopic composition of seawater: stratigraphic and biogeochemical implications. *Precambrian research*, 73, 27-49.

Knoll, A. H., Hayes, J. M., Kaufman, A. J., Swett, K., & Lambert, I. B., 1986. Secular variation in carbon isotope ratios from Upper Proterozoic successions of Svalbard and East Greenland. *Nature*, 321, 832-838.

Kuchenbecker, M., Reis, H. L. S., & Fragoso, D. G. C. 2011. Caracterização estrutural e considerações sobre a evolução tectônica da Formação Salitre na porção central da Bacia de Irecê, norte do Cráton do São Francisco (BA). *Geonomos* 19.

Kuznetsov, A. B., Semikhatov, M. A., & Gorokhov, I. M., 2012. The Sr isotope composition of the world ocean, marginal and inland seas: Implications for the Sr isotope stratigraphy. *Stratigraphy and Geological Correlation*, 20, 501-515.

Kyle, J. R., & Misi, A. (1997). Origin of Zn-Pb-Ag sulfide mineralization within upper Proterozoic phosphate-rich carbonate strata, Irece basin, Bahia, Brazil. *International Geology Review*, 39, 383-399.

Lagoeiro, L. E., 1990. Estudo da deformação nas sequências carbonáticas do Grupo Uma, na região de Irecê, Bahia. Dissertação de mestrado, Universidade Federal de Ouro Preto, Ouro Preto, (105pp).

Laubach, S. E., Eichhubl, P., Hilgers, C., & Lander, R. H., 2010. Structural diagenesis. *Journal of Structural Geology*, 32, 1866-1872.

Loureiro H.S.C., Bahiense I.C., Neves J.P., Guimarães J.T., Teixeira L. R., Santos R.A., Melo R.C. (Org.). 2009. Geologia e recursos minerais da parte norte do corredor de deformação do Paramirim: (Projeto Barra – Oliveira dos Brejinhos). Companhia Baiana de Pesquisa Mineral-CBPM, Salvador, Série Arquivos Abertos 33, 113p.

Macdonald, F.A., et al., 2010. Calibrating the Cryogenian. *Science* 327 (5970), 1241–1243.

Machel, H. G. 2001. Bacterial and thermochemical sulfate reduction in diagenetic settings—old and new insights. *Sedimentary Geology*, 140, 143–175.

Machel, H. G. 2001. Bacterial and thermochemical sulfate reduction in diagenetic settings—old and new insights. *Sedimentary Geology*, 140, 143–175.

Machel, H. G., Krouse, H. R., Riciputi, L. R., & Cole, D. R. 1995. Devonian Nisku sour gas play, Canada: A unique natural laboratory for study of thermochemical sulfate reduction. (eds. M. A. Vairavamurthy and M. A. A. Schoonen), pp. 439–454.

Magalhães, A.J.C., Raja Gabaglia, G.P., Scherer, C.M.S., Bállico, M. B., Guadagnin, F., Bento Freire, E., Silva Born, L.R., Catuneanu, O. 2016. Sequence hierarchy in a Mesoproterozoic interior sag basin: from basin fill to reservoir scale, the Tombador Formation.

Magalhães, A.J.C., Scherer, C.M.S., Raja Gabaglia, G.P., Bállico, M. B., Catuneanu, O. 2014. Unclosed fluvial and tide-dominated estuarine systems from the Meso-proterozoic Lower Tombador Formation, Chapada Diamantina basin, Brazil. *Journal South American Earth Science*, 56, 68–90.

Martins-Neto, M. A. 2009. Sequence stratigraphic framework of Proterozoic successions in eastern Brazil. *Marine and Petroleum Geology*, 26, 163–176.

Martins-Neto, M.A., 2000. Tectonics and sedimentation in a paleo/mesoproterozoic rift-sag basin (Espinhaço basin, southeastern Brazil). *Precambrian Research*, 103, 147–173.

Mazzullo,S.J.,& Harris,P.M. 1992. Mesogenetic dissolution: Its role in porosity development in carbonate reservoirs. *AAPG bulletin*, 76(5), 607-620.

Melezhik, V.A., Gorokhov, I.M., Kuznetsov, A.B., Fallick, A.E., 2001. Chemostratigraphy of Neoproterozoic carbonates: implications for ‘blind dating’. *Terra Nova*, 13, 1–11.

Michie, E. A. H., Haines, T. J., Healy, D., Neilson, J. E., Timms, N. E., & Wibberley, C. A. J., 2014. Influence of carbonate facies on fault zone architecture. *Journal of Structural Geology*, 65, 82–99.

Misi, A. 1979. O Grupo Bambuí no estado da Bahia. *Geologia e recursos minerais do estado da Bahia: Textos básicos*. Salvador, CPM, 1, 119–154.

Misi, A., & Kyle, J. R. 1994. Upper Proterozoic carbonate stratigraphy, diagenesis, and stromatolitic phosphorite formation, Irecê Basin, Bahia, Brazil. *Journal of Sedimentary Research*, 64, 299–310.

Misi, A., & Veizer, J. 1998. Neoproterozoic carbonate sequences of the Una Group, Irecê Basin, Brazil: chemostratigraphy, age and correlations. *Precambrian Research*, 89, 87–100.

Misi, A., Iyer, S.S.S., Coelho, C.E.S., Tassinari, C.C.G., Franca-Rocha, W.J.S., Cunha, I.D.A., Gomes, A.S.R., de Oliveira, T.F., Teixeira, J.B.G., Filho, V.M.C., 2005. Sediment hosted lead–zinc deposits of the Neoproterozoic Bambuí Group and correlative sequences, São Francisco craton, Brazil: a review and a possible metallogenic evolution model. *Ore Geology Reviews*, 26, 263–304.

Misi, A., Kaufman, A., Veizer, J., Powis, K., Azmy, K., Boggiani, P., Gaucher, C., Teixeira, J.B.G., Sanches, A., Iyer, S., 2007. Chemostratigraphic correlation of Neoproterozoic successions in South America. *Chemical Geology*, 237, 143–167.

Misi, A.; Silva, M.G. 1996. Chapada Diamantina Oriental, Bahia. *Geologia e Depósitos Minerais*. Superintendência de Geologia e Recursos Minerais/Universidade Federal da Bahia, Salvador, 194 p.

Misi, A.; Souto, P.G. 1975. Controle estratigráfico das mineralizações de Pb-Zn-F-Ba do Grupo Bambuí, parte leste da Chapada de Irecê (Bahia). *Rev. Bras. Geociências*, 5, 30-45.

Montaron, B., 2008. Confronting carbonates. *Oil Rev. Middle East* 5: 132 –135.

Moore, C. H., & Wade, W. J., 2013. Natural fracturing in carbonate reservoirs. In *Developments in Sedimentology*, Vol. 67, pp. 285-300. Elsevier.

Moore, C. H., 1989. Carbonate diagenesis and porosity: Amsterdam, Elsevier, *Developments in Sedimentology*, 46, 338 p.

Moore, C.H., 2001. Carbonate reservoir porosity evolution and diagenesis in a sequence-stratigraphic framework: Amsterdam. *Dev. Sedimentol.*, 55, 460.

Neves, B. B. D. B., Fuck, R. A., & Pimentel, M. M. 2014. The Brasiliano collage in South America: a review. *Brazilian Journal of Geology*, 44(3), 493-518.

O'Neil, J. R., & Epstein, S., 1966. Oxygen isotope fractionation in the system dolomite-calcite-carbon dioxide. *Science*, 152(3719), 198-201.

Paula-Santos, G. M., Babinski, M., Kuchenbecker, M., Caetano-Filho, S., Trindade, R. I., & Pedrosa-Soares, A. C. 2015. New evidence of an Ediacaran age for the Bambuí Group in southern São Francisco craton (eastern Brazil) from zircon U–Pb data and isotope chemostratigraphy. *Gondwana Research*, 28, 702-720.

Paula-Santos, G. M., Caetano-Filho, S., Babinski, M., Trindade, R. I., & Guacaneme, C., 2017. Tracking connection and restriction of West Gondwana São Francisco Basin through isotope chemostratigraphy. *Gondwana Research*, 42, 280-305.

Peacock, D. C. P. 2002. Propagation, interaction and linkage in normal fault systems. *Earth-Science Reviews*, 58, 121-142.

Peacock, D. C. P., Dimmen, V., Rotevatn, A., & Sanderson, D. J., 2017. A broader classification of damage zones. *Journal of Structural Geology*, 102, 179-192.

Peacock, D. C. P., Nixon, C. W., Rotevatn, A., Sanderson, D. J., & Zuluaga, L. F., 2016. Glossary of fault and other fracture networks. *Journal of Structural Geology*, 92, 12-29.

Peacock, D. C. P., Sanderson, D. J., & Rotevatn, A., 2018. Relationships between fractures. *Journal of Structural Geology*, 106, 41-53.

Pedreira, A. J. et al. 1987. Projeto Bacia do Irecê II: relatório final. Texto. Salvador: CPRM, v. 1. 168 p.

Pedreira, A.J., De Waele, B., 2008. Contemporaneous evolution of the Palaeoproterozoic–Mesoproterozoic sedimentary basins of the São Francisco–Congo Craton. In: Pankhurst, R.J., Trouw, R.A.J., Brito Neves, B.B., De Wit, M.J. (Eds.), West Gondwana:

Pedreira, A.J.C.L. 1997. O limite Meso-Neoproterozoico na região central da Bahia. In: SBG/NMG, Simpósio de Geologia de Minas Gerais, 9, Anais, p. 1–2.

Pedreira, A.J.C.L., Arcanjo, J. B., Pedrosa, C.J., Oliveira, J.E., Silva, B. C.E. 1975. Projeto Bahia - Geologia da Chapada Diamantina, Relatório Final. DNPM/CPRM, 225 p

Pierre, C. 1989. Sedimentation and diagenesis in restricted marine basins. Handbook of environmental isotope geochemistry, 3, 257-315.

Pili, E., Poitrasson, F., & Gratier, J. P. 2002. Carbon–oxygen isotope and trace element constraints on how fluids percolate faulted limestones from the San Andreas Fault system: partitioning of fluid sources and pathways. Chemical Geology, 190, 231-250.

Redivo, H. V., Mizusaki, A. M., & Santana, A. V. 2019. REE patterns and trustworthiness of stable carbon isotopes of Salitre Formation, Irecê Basin (Neoproterozoic), São Francisco Craton. Journal of South American Earth Sciences, 90, 255-264.

Rose, C. V., Swanson-Hysell, N. L., Husson, J. M., Poppick, L. N., Cottle, J. M., Schoene, B., Maloof, A. C., 2012. Constraints on the origin and relative timing of the Trezona $\delta^{13}\text{C}$ anomaly below the end-Cryogenian glaciation. Earth and Planetary Science Letters, 319, 241-250.

Santana, A.V.A. Análise estratigráfica em alta resolução: exemplo em rampa carbonática dominada por microbialitos da Formação Salitre, Bacia do Irecê, Bahia. Tese (Doutorado em Geologia) – Instituto de Geociências, Universidade de Brasília. Brasília, 2016

Santos R.V., Alvarenga C.J.S., Dardenne M.A., Sial A.N., Ferreira V.P., 2000. Carbon and oxygen isotope profiles across Meso-Neoproterozoic limestones from central Brazil: Bambuí and Paranoá Groups. Precambrian Research, 104, 107-122.

Santos,M.N., Chemale Jr., F., Dussin, I.A., Martins, M., Assis, T.A.R., Jelinek, A.R., Guadagnin, F., Armstrong, R., 2013. Sedimentological and paleoenvironmental constraints of the Statherian and Stenian Espinhaço rift system, Brazil. Sedimentary Geology, 290, 47–59.

Schobbenhaus C., Kaul, P.T. 1971. Contribuição à Estratigrafia da Chapada Diamantina Bahia-Central. Mineração e Metalurgia, 53 (315): 116–120.

Schobbenhaus, C. 1996. As tafrogênese superpostas Espinhaço e Santo Onofre, estado da Bahia: Revisão e novas propostas. Revista Brasileira de Geociências, 4, 265–276.

Schobbenhaus, C., Hoppe, A., Baumann, A., Lork, A. 1994. Idade U/Pb do vulcanismo Rio dos Remédios, Chapada Diamantina, Bahia. In: SBG, Congresso Brasileiro de Geologia, 38, Anais, 2, p. 397–399.

Shields, G. A., 2007. A normalised seawater strontium isotope curve: possible implications for Neoproterozoic-Cambrian weathering rates and the further oxygenation of the Earth. *EEarth*, 2, 35-42.

Shields, G., & Veizer, J. 2002. Precambrian marine carbonate isotope database: Version 1.1. *Geochemistry, Geophysics, Geosystems*, 3(6)

Silveira, E.M., Söderlund, U., Oliveira, E.P., Ernst, R.E., Menezes Leal, A.B. 2013. First precise U-Pb baddeleyite ages of 1500 Ma mafic dykes from the São Francisco Craton, Brazil, and tectonic implications. *Lithos*, 174, 144 – 156.

Souza, S. L., Brito, P. C. R., & Silva, R. W. S. 1993. Estratigrafia, Sedimentologia e Recursos Minerais da Formação Salitre na Bacia de Irecê, Bahia (Série Arquivos Abertos 2). Companhia Baiana de Pesquisa Mineral (CBPM), Salvador.

Srivastava, N.K., 1986, Os Estromatólitos do Projeto Bacia de Irecê II: Universidade Federal do Rio Grande do Norte, Natal, Brasil, 9 p. (unpublished report).

Strauss, H. 1993. The sulfur isotopic record of Precambrian sulfates: new data and a critical evaluation of the existing record. *Precambrian research*, 63, 225-246.

Swart, P. K., and G. Eberli, 2005. The nature of the $\delta^{13}\text{C}$ of periplatform sediments: Implications for stratigraphy and the global carbon cycle: *Sedimentary Geology*, 175, p. 115–129.

Swart, P. K., Reijmer, J. J., & Otto, R., 2009. A reevaluation of facies on Great Bahama Bank II: Variations in the $\delta^{13}\text{C}$, $\delta^{18}\text{O}$ and mineralogy of surface sediments. *Int. Assoc. Sedimentol. Spec. Publ*, 41, 47-59.

Teixeira, L. 2005. Projeto Barra-Oliveira dos Brejinhos. Relatório Temático de Litogeocquímica. Convênio CPRM/CBPM, 29p.

Teles, D. R. D. S., Azevedo, A. E. G. D., & Santos, C. P. L. D., 2010. Caracterização isotópica de águas de formação hipersalinas de um campo de petróleo da Bacia do Recôncavo, Brasil. *Revista Brasileira de Geofísica*, 28, 291-301.

Thomas, C., Graham, C., Ellam, R., & Fallick, A., 2004. $^{87}\text{Sr}/^{86}\text{Sr}$ chemostratigraphy of Neoproterozoic Dalradian limestones of Scotland and Ireland: constraints on depositional ages and time scales. *Journal of the Geological Society*, 161, 229-242.

Torquato, J. R., & Misi, A., 1977. Medidas isotópicas de carbono e oxigenio em carbonatos do Grupo Bambui, na regiao centro-norte do Estado da Bahia. *Revista Brasileira de Geociências*, 7, 14-24.

Trindade, R.I. F., D'Agrella-Filho, M.S., Babinski, M., Font, E., Brito Neves, B.B. 2004. Paleomagnetism and geochronology of the Bebedouro Cap Carbonate: Evidence for continental-scale Cambrian remagnetization in the São Francisco craton, Brazil. *Precambrian Research*, 128, 83–103.

- Uhlein, G.J., et al., 2019. Ediacaran paleoenvironmental changes recorded in the mixed carbonate-siliciclastic Bambu' Basin, Brazil. *Palaeogeogr. Palaeoclimatol. Palaeoecol.*, 517, 39–51. Elsevier.
- Underwood, C. A., Cooke, M. L., Simo, J. A., & Muldoon, M. A. 2003. Stratigraphic controls on vertical fracture patterns in Silurian dolomite, northeastern Wisconsin. *AAPG bulletin*, 87, 121-142.
- Veizer, J., et al., 1999. $^{87}\text{Sr}/^{86}\text{Sr}$, $\delta^{13}\text{C}$ and $\delta^{18}\text{O}$ evolution of Phanerozoic seawater. *Chem. Geol.* 161 (1 –3), 59–88.
- Vieira, L. C., Trindade, R. I., Nogueira, A. C., & Ader, M., 2007. Identification of a Sturtian cap carbonate in the Neoproterozoic Sete Lagoas carbonate platform, Bambu' Group, Brazil. *Comptes Rendus Geoscience*, 339, 240-258.
- Walker, R. G. 1992. Facies, facies models and modern stratigraphic concepts. In: Walker, R. G. e James, N. P. (eds) *Facies models: response to sea level change*, Geological Association of Canada, Ontario, 1–14.
- Wang, G., Li, P., Hao, F., Zou, H., & Yu, X. 2015. Dolomitization process and its implications for porosity development in dolostones: A case study from the Lower Triassic Feixianguan Formation, Jiannan area, Eastern Sichuan Basin, China. *Journal of Petroleum Science and Engineering*, 131, 184-199.
- Warren LV, Quaglio F, Riccomini C, Simões MG, Poiré DG, Strikis NM, Aneli LE, Strikis, P.C. 2014. The puzzle assembled: Ediacaran guide fossil Cloudina reveals an old proto-Gondwana seaway. *Geology*, 5, 391– 394.
- Warren, J. 2000. Dolomite: occurrence, evolution and economically important associations. *Earth-Science Reviews*, 52, 1-81.
- Weyl ,P. K. 1960. Porosity through dolomitization--Conservation-of-mass requirements. *Journal of Sedimentary Research*, 30, 85-90.
- Whiticar, M. J., Faber, E., & Schoell, M., 1986. Biogenic methane formation in marine and freshwater environments: CO₂ reduction vs. acetate fermentation-isotope evidence. *Geochimica et Cosmochimica Acta*, 50, 693-709.
- Zachos, J. C., & Kump, L. R., 2005. Carbon cycle feedbacks and the initiation of Antarctic glaciation in the earliest Oligocene. *Global and Planetary Change*, 47, 51-66.
- Zhou, G.-T., Zheng, Y.-F., 2006. On the direction and magnitude of oxygen isotope fractionation between calcite and aragonite at thermodynamic equilibrium. *Aquatic Geochemistry* 12, 239–268.

ANEXO A – Dados de C e O amostras de mão

Amostra	$\delta^{13}\text{C}\text{\textperthousand}$	$\delta^{18}\text{O}\text{\textperthousand}$ VPDB	$\delta^{18}\text{O}\text{\textperthousand}$ SMOW	Posição na coluna	Fácies	Section
CARB-531	1.04	-1.30	29.52	130	F7	MS
CARB-532	1.28	-2.27	28.52	131	F7	MS
CARB-533	0.59	-2.28	28.51	132	F7	MS
CARB-534	0.07	-3.52	27.23	133	F7	MS
CARB-535	-0.61	-5.69	24.99	134	F7	MS
CARB-536	-0.22	-4.93	25.78	135	F7	MS
CARB-537	0.79	-2.06	28.73	136	F7	MS
CARB-538	0.86	-2.01	28.79	137	F7	MS
CARB-539	-0.48	-3.64	27.10	138	F7	MS
CARB-540	1.94	-1.89	28.91	139	F7	MS
CARB-541	2.19	-1.64	29.16	140	F7	MS
CARB-542	1.99	-3.06	27.71	141	F7	MS
CARB-543	1.43	-2.79	27.98	142	F7	MS
CARB-544	1.62	-1.60	29.21	143	F7	MS
CARB-545	2.30	-2.56	28.22	144	F7	MS
CARB-546	2.91	-1.24	29.58	145	F7	MS
CARB-547	3.30	-1.46	29.36	146	F7	MS
CARB-548	3.31	-1.28	29.54	147	F7	MS
CARB-549	3.21	-2.28	28.51	148	F7	MS
CARB-550	3.98	-2.09	28.70	149	F7	MS
CARB-551	3.61	-2.85	27.92	150	F7	MS
CARB-552	2.07	-2.25	28.54	151	F7	MS
CARB-553	2.09	-1.54	29.28	152	F7	MS
CARB-554	2.70	-0.57	30.27	153	F7	MS
CARB-555	3.07	-1.33	29.49	154	F7	MS
CARB-556	2.27	-1.93	28.87	155	F7	MS
CARB-557	3.00	-1.93	28.87	156	F7	MS
CARB-558	1.78	-3.03	27.73	157	F7	MS
CARB-559	2.92	-2.46	28.33	158	F7	MS
CARB-560	4.20	-2.16	28.63	159	F7	MS
CARB-561	4.65	-2.79	27.98	160	F7	MS
CARB-562	4.97	-3.78	26.96	161	F9	MS
CARB-563	4.11	-2.84	27.93	162	F9	MS
CARB-564	4.44	-2.94	27.83	163	F9	MS
CARB-565	3.83	-3.67	27.08	164	F10	MS
CARB-566	4.93	-3.33	27.42	165	F10	MS
CARB-567	3.36	-4.55	26.17	166	F10	MS
CARB-568	3.63	-1.34	29.48	167	F10	MS
CARB-569	5.80	-3.21	27.55	168	F10	MS
CARB-570	6.89	-4.79	25.92	169	F10	MS
CARB-571	7.30	-2.48	28.30	170	F3	MS
CARB-572	7.74	-1.79	29.01	171	F3	MS
CARB-573	6.55	-4.70	26.02	172	F3	MS
CARB-574	8.85	-3.54	27.21	173	F3	MS

Amostra	$\delta^{13}\text{C}\text{\%}$	$\delta^{18}\text{O}\text{\%}$ VPDB	$\delta^{18}\text{O}\text{\%}$ SMOW	Posição na coluna	Fáries	Section
CARB-575	9.58	-4.80	25.91	174	F11	US
CARB-576	9.15	-6.28	24.39	175	F11	US
CARB-577	8.98	-7.36	23.27	176	F11	US
CARB-578	7.71	-6.68	23.97	177	F11	US
CARB-579	9.70	-4.47	26.25	178	F11	US
CARB-580	9.14	-4.48	26.24	179	F11	US
CARB-581	10.17	-4.79	25.92	180	F12	US
CARB-582	9.82	-5.21	25.49	181	F12	US
CARB-583	10.89	-4.81	25.90	182	F12	US
CARB-584	9.78	-6.44	24.22	183	F12	US
CARB-585	9.38	-4.96	25.75	184	F12	US
CARB-586	10.69	-5.86	24.82	185	F12	US
CARB-587	10.56	-6.29	24.37	186	F12	US
CARB-588	10.46	-6.83	23.82	187	F12	US
CARB-589	10.48	-6.76	23.89	188	F12	US
CARB-590	9.81	-6.06	24.61	189	F12	US
CARB-591	9.41	-7.81	22.81	190	F12	US
CARB-592	9.28	-6.75	23.90	191	F12	US
CARB-593	9.89	-6.58	24.07	192	F12	US
CARB-594	9.50	-6.10	24.57	193	F12	US
CARB-595	10.24	-7.22	23.42	194	F12	US
CARB-596	10.67	-5.75	24.93	202	F7	US
CARB-597	9.77	-3.56	27.19	203	F7	US
CARB-598	9.64	-4.66	26.06	204	F7	US
CARB-599	10.87	-2.93	27.84	205	F3	US
CARB-600	8.91	-4.67	26.05	206	F3	US
CARB-601	9.05	-5.04	25.66	207	F3	US
CARB-602	8.09	-3.54	27.21	174	F11	US
CARB-603	9.29	-4.11	26.63	175	F11	US
CARB-604	8.98	-4.98	25.72	176	F11	US
CARB-605	11.02	-4.64	26.08	177	F11	US
CARB-606	7.75	-5.47	25.22	178	F11	US
CARB-607	9.11	-4.92	25.78	179	F11	US
CARB-608	10.25	-3.71	27.03	180	F11	US
CARB-609	10.46	-2.43	28.35	181	F12	US
CARB-610	8.75	-6.53	24.13	182	F12	US
CARB-611	7.77	-6.85	23.80	183	F12	US
CARB-612-A	9.47	-5.57	25.12	184	F12	US
CARB-613	12.36	-4.64	26.08	185	F12	US
CARB-614	11.04	-4.43	26.29	186	F12	US
CARB-615	9.36	-4.62	26.10	187	F12	US
CARB-616	9.69	-4.83	25.89	188	F12	US
CARB-617	8.82	-6.84	23.81	189	F12	US
CARB-618	13.36	-5.67	25.01	190	F12	US

Amostra	$\delta^{13}\text{C}\text{\%}$	$\delta^{18}\text{O}\text{\%}$ VPDB	$\delta^{18}\text{O}\text{\%}$ SMOW	Posição na coluna	Fácies	Section
CARB-619	11.31	-6.41	24.25	191	F12	US
CARB-620	11.80	-6.57	24.08	192	F12	US
CARB-621	10.34	-7.32	23.32	193	F12	US
CARB-622	9.83	-6.53	24.13	194	F12	US
CARB-623	11.43	-6.26	24.41	195	F12	US
CARB-624	9.87	-5.82	24.86	196	F12	US
CARB-625	9.42	-6.76	23.89	197	F12	US
CARB-626	13.69	-4.54	26.18	198	F12	US
CARB-627	10.88	-6.03	24.65	199	F12	US
CARB-628	10.17	-4.41	26.32	200	F12	US
CARB-629	9.05	-5.70	24.99	201	F12	US
CARB-630	8.00	-6.27	24.40	202	F7	US
CARB-631	4.04	-5.87	24.81	203	F7	US
CARB-632	9.78	-3.90	26.84	204	F7	US
CARB-633	12.76	-6.07	24.60	205	F3	US
CARB-634	11.93	-4.76	25.96	206	F3	US
CARB-635	9.70	-6.01	24.66	207	F3	US
CARB-636	10.20	-4.31	26.42	208	F3	US
CARB-637	9.55	-4.78	25.93	209	F3	US
CARB-638	11.16	-4.03	26.70	210	F3	US
CARB-639	9.65	-5.64	25.04	211	F3	US
CARB-640	9.84	-4.71	26.00	212	F12	US
CARB-641	10.03	-6.33	24.33	212	F12	US
CARB-642	11.55	-4.14	26.59	213	F12	US
CARB-643	10.34	-5.23	25.47	214	F12	US
CARB-644	11.15	-5.58	25.11	215	F12	US
CARB-645	9.12	-6.22	24.45	216	F12	US
CARB-646	9.96	-4.65	26.07	217	F12	US
CARB-647	9.91	-5.59	25.10	218	F12	US
CARB-648	10.96	-4.07	26.67	219	F12	US
CARB-649	7.14	-5.96	24.71	220	F12	US
CARB-650	1.84	-5.37	25.32	221	F12	US
CARB-651	8.65	-5.17	25.53	222	F5	US
CARB-652	9.61	-4.58	26.14	223	F5	US
CARB-653	9.83	-4.41	26.31	224	F5	US
CARB-654	9.62	-4.54	26.18	225	F5	US
CARB-655	9.45	-4.98	25.72	226	F5	US
CARB-656	9.93	-4.98	25.73	227	F5	US
CARB-657	11.95	-4.94	25.77	228	F5	US
CARB-658	10.19	-5.29	25.41	229	F5	US
CARB-659	8.95	-6.10	24.57	230	F5	US
CARB-660	10.78	-5.77	24.91	231	F7	US
CARB-661	8.92	-6.13	24.54	232	F7	US
CARB-662	9.72	-6.32	24.34	233	F7	US

Amostra	$\delta^{13}\text{C}\text{\%}$	$\delta^{18}\text{O}\text{\%}$ VPDB	$\delta^{18}\text{O}\text{\%}$ SMOW	Posição na coluna	Fáries	Section
CARB-663	10.52	-6.63	24.02	234	F7	US
CARB-664	10.02	-6.89	23.75	235	F7	US
CARB-665	11.30	-6.05	24.62	236	F7	US
CARB-666	10.84	-5.97	24.70	237	F7	US
CARB-667	10.22	-6.04	24.64	238	F7	US
CARB-668	10.64	-5.43	25.26	239	F3	US
CARB-669	10.35	-6.88	23.77	240	F3	US
CARB-670	9.86	-7.06	23.58	241	F3	US
CARB-671	9.92	-7.52	23.11	242	F3	US
CARB-672	10.97	-4.71	26.01	243	F3	US
CARB-673	9.42	-4.90	25.81	244	F3	US
CARB-674	11.25	-6.54	24.12	245	F3	US
CARB-675	11.83	-5.75	24.93	246	F3	US
CARB-676	9.02	-6.61	24.05	247	F3	US
CARB-677	12.37	-7.10	23.54	248	F3	US
CARB-678	10.56	-5.39	25.30	249	F3	US
CARB-679	10.80	-5.80	24.89	250	F3	US
CARB-680	11.36	-5.45	25.25	251	F3	US
CARB-681	10.69	-5.96	24.71	252	F3	US
CARB-682	9.14	-6.08	24.59	253	F3	US
CARB-683	8.46	-5.22	25.48	254	F12	US
CARB-684	10.75	-4.74	25.97	255	F12	US
CARB-685	8.98	-6.29	24.37	256	F12	US
CARB-686	9.26	-5.40	25.29	257	F12	US
CARB-687	9.55	-5.17	25.53	258	F12	US
CARB-688	8.73	-5.42	25.27	259	F12	US
CARB-689	9.55	-6.85	23.80	260	F12	US
CARB-690	9.41	-6.26	24.41	261	F12	US
CARB-691	9.28	-5.55	25.13	262	F12	US
CARB-692	7.64	-4.29	26.44	263	F12	US
CARB-693	10.64	-4.49	26.23	264	F12	US
CARB-694	8.70	-4.26	26.47	265	F12	US
CARB-695	7.30	-5.81	24.88	266	F12	US
CARB-696	8.81	-5.42	25.27	267	F12	US
CARB-697	9.49	-5.22	25.48	268	F12	US
CARB-698	9.38	-6.19	24.48	269	F12	US
CARB-699	8.80	-5.51	25.18	270	F12	US
CARB-700	10.37	-5.77	24.92	271	F12	US
CARB-701	10.13	-4.29	26.44	272	F12	US
CARB-702	9.41	-3.91	26.83	273	F12	US
CARB-703	9.17	-6.15	24.52	274	F12	US
CARB-704	9.02	-6.65	24.00	275	F12	US
CARB-705	10.06	-5.47	25.22	276	F12	US
CARB-706	10.07	-3.68	27.06	277	F12	US

Amostra	$\delta^{13}\text{C}\text{\%}$	$\delta^{18}\text{O}\text{\%}$ VPDB	$\delta^{18}\text{O}\text{\%}$ SMOW	Posição na coluna	Fácies	Section
CARB-707	9.37	-5.02	25.68	278	F12	US
CARB-708	9.11	-4.45	26.27	279	F12	US
CARB-709	8.89	-6.56	24.10	280	F12	US
CARB-710	9.10	-6.21	24.46	281	F12	US
CARB-711	9.71	-4.73	25.99	282	F12	US
CARB-712	9.18	-6.44	24.22	283	F12	US
CARB-713	9.10	-5.83	24.85	284	F12	US
CARB-714	8.79	-5.92	24.76	285	F12	US
CARB-715	8.52	-5.37	25.32	286	F12	US
CARB-716	9.16	-4.35	26.37	287	F12	US
CARB-717	8.40	-6.31	24.35	288	F12	US
CARB-718	8.82	-4.57	26.14	289	F12	US
CARB-719	8.57	-4.19	26.54	290	F7	US
CARB-720	9.38	-3.37	27.39	291	F7	US
CARB-721	9.46	-3.21	27.55	292	F7	US
CARB-722	6.13	-4.12	26.61	293	F7	US
CARB-723	9.02	-4.38	26.35	294	F3	US
CARB-724	9.31	-4.48	26.24	295	F3	US
CARB-725	9.82	-3.79	26.95	296	F3	US
CARB-726	9.62	-5.30	25.40	297	F3	US
CARB-727	9.95	-5.73	24.96	298	F5	US
CARB-728	10.32	-5.50	25.19	299	F5	US
CARB-729	10.01	-5.89	24.79	300	F5	US
CARB-730	8.39	-6.38	24.28	301	F5	US
CARB-731	10.25	-5.44	25.25	302	F5	US
CARB-732	9.48	-6.02	24.65	303	F3	US
CARB-733	9.52	-5.95	24.72	304	F3	US
CARB-734	8.33	-6.27	24.40	305	F3	US
CARB-735	8.68	-6.10	24.57	306	F3	US
CARB-736	8.25	-6.32	24.35	307	F3	US
CARB-737	10.72	-6.25	24.41	308	F7	US
CARB-738	10.72	-6.51	24.15	309	F7	US
CARB-739	10.99	-5.55	25.14	310	F7	US
CARB-740	10.35	-6.59	24.07	311	F7	US
CARB-741	11.88	-6.00	24.68	312	F7	US
CARB-742-A	11.40	-6.31	24.36	313	F7	US
CARB-743-A	11.37	-6.16	24.51	314	F7	US
CARB-743-B	7.74	-6.53	24.13	314	F7	US
CARB-744	11.05	-6.53	24.13	315	F7	US
CARB-745	11.51	-6.34	24.33	316	F7	US
CARB-746-A	11.47	-6.21	24.45	317	F7	US
CARB-747	11.80	-6.55	24.11	318	F7	US
CARB-748	7.96	-3.39	27.36	319	F7	US
CARB-749	9.03	-3.16	27.61	320	F7	US

Amostra	$\delta^{13}\text{C}\text{\%}$	$\delta^{18}\text{O}\text{\%}$ VPDB	$\delta^{18}\text{O}\text{\%}$ SMOW	Posição na coluna	Fácies	Section
CARB-750	9.18	-4.34	26.39	321	F3	US
CARB-751	9.76	-3.76	26.98	322	F3	US
CARB-752	9.54	-4.03	26.71	323	F3	US
CARB-753	9.00	-6.13	24.54	324	F3	US
CARB-754-A	10.31	-5.51	25.18	325	F3	US
CARB-755	9.93	-3.89	26.85	326	F3	US
CARB-756	8.98	-3.72	27.03	327	F3	US
CARB-757	5.66	-3.79	26.96	328	F3	US
CARB-758	8.22	-4.97	25.74	329	F3	US
CARB-759	9.77	-3.79	26.96	330	F3	US
CARB-760-A	9.64	-4.12	26.61	331	F12	US
CARB-761	8.77	-5.02	25.68	332	F12	US
CARB-762	7.42	-3.21	27.55	333	F12	US
CARB-763	8.53	-6.82	23.83	334	F12	US
CARB-764-A	8.65	-6.13	24.54	335	F12	US
CARB-765	8.78	-6.42	24.25	336	F12	US
CARB-766-A	8.79	-6.42	24.24	337	F12	US
CARB-767	8.82	-5.85	24.83	338	F12	US
CARB-768	8.84	-6.49	24.17	339	F12	US
CARB-769	9.10	-5.85	24.83	340	F12	US
CARB-770	9.02	-6.12	24.56	341	F12	US
CARB-771	8.83	-6.54	24.12	342	F12	US
CARB-772	8.96	-6.11	24.56	343	F3	US
CARB-773	8.94	-7.03	23.61	344	F3	US
CARB-774	9.05	-6.36	24.30	345	F3	US
CARB-775	1.03	-6.46	24.20	1	F1	LS
CARB-776	0.71	-6.87	23.78	2	F1	LS
CARB-777	1.00	-6.63	24.02	3	F1	LS
CARB-778	1.42	-6.28	24.39	4	F1	LS
CARB-779	0.24	-6.88		5	F1	LS
CARB-780	0.62	-6.75	23.90	6	F1	LS
CARB-781	0.96	-6.22	24.45	7	F1	LS
CARB-782	0.79	-6.42	24.24	8	F1	LS
CARB-783	0.63	-6.27	24.40	9	F1	LS
CARB-784	0.89	-6.31	24.36	10	F1	LS
CARB-785	0.54	-6.99	23.65	11	F1	LS
CARB-786	0.82	-6.40	24.26	12	F1	LS
CARB-787	1.09	-6.42	24.24	13	F1	LS
CARB-788	1.24	-5.57	25.12	14	F1	LS
CARB-789	0.83	-7.53	23.10	15	F1	LS
CARB-790	0.46	-6.35		16	F1	LS
CARB-791	0.94	-6.79	23.86	17	F1	LS
CARB-792	2.05	-5.43	25.27	18	F1	LS
CARB-793	2.32	-5.42	25.28	19	F1	LS

Amostra	$\delta^{13}\text{C}\text{\%}$	$\delta^{18}\text{O}\text{\%}$ VPDB	$\delta^{18}\text{O}\text{\%}$ SMOW	Posição na coluna	Fácies	Section
CARB-794	2.32	-5.30	25.39	20	F1	LS
CARB-795	1.90	-5.03	25.68	21	F1	LS
CARB-796	3.17	-4.55	26.17	22	F1	LS
CARB-797	1.65	-5.76	24.92	23	F1	LS
CARB-798	0.75	-6.95		24	F1	LS
CARB-799	2.32	-5.31	25.39	25	F1	LS
CARB-800	2.62	-5.12	25.58	26	F1	LS
CARB-801	2.26	-5.31	25.38	27	F1	LS
CARB-802	0.57	-6.79		28	F1	LS
CARB-803	0.18	-6.62		29	F1	LS
CARB-804	1.74	-4.93	25.77	30	F6	LS
CARB-805	0.43	-6.68		31	F6	LS
CARB-806	0.87	-6.81		32	F6	LS
CARB-807	0.34	-6.85		33	F6	LS
CARB-808	0.56	-6.68		34	F6	LS
CARB-809	1.44	-6.02	24.65	35	F6	LS
CARB-810	0.61	-7.06	23.58	36	F1	LS
CARB-811	0.66	-6.97		37	F1	LS
CARB-812	0.86	-6.71		38	F1	LS
CARB-813	0.83	-6.89		39	F1	LS
CARB-814	2.06	-5.61	25.08	40	F1	LS
CARB-815	1.12	-6.24	24.43	41	F1	LS
CARB-816	0.66	-6.71		42	F1	LS
CARB-817	0.80	-6.79		43	F1	LS
CARB-820	0.82	-6.49		46	F6	LS
CARB-821	0.66	-6.71		47	F6	LS
CARB-822	0.54	-6.47		48	F6	LS
CARB-823	0.05	-6.64		49	F6	LS
CARB-824	0.64	-6.72		50	F6	LS
CARB-825	0.81	-6.42		51	F6	LS
CARB-826	0.49	-6.81		52	F6	LS
CARB-827	1.55	-4.84		53	F6	LS
CARB-828	1.84	-4.60		54	F6	LS
CARB-829	0.89	-6.66		55	F1	LS
CARB-830	0.90	-6.75		56	F1	LS
CARB-831	0.95	-6.65		57	F1	LS
CARB-832	1.31	-6.04		58	F1	LS
CARB-833	1.08	-6.54		59	F1	LS
CARB-834	0.98	-6.54		60	F1	LS
CARB-835	0.93	-6.53		61	F1	LS
CARB-836	0.84	-6.63		62	F1	LS
CARB-837	0.80	-6.58		63	F1	LS
CARB-838	0.94	-6.69		64	F1	LS
CARB-839	0.67	-5.77		65	F1	LS

Amostra	$\delta^{13}\text{C}\text{\%}$	$\delta^{18}\text{O}\text{\%}$ VPDB	$\delta^{18}\text{O}\text{\%}$ SMOW	Posição na coluna	Fáries	Section
CARB-840	0.53	-6.25		66	F1	LS
CARB-841	0.13	-6.23		67	F1	LS
CARB-842	0.55	-6.37		68	F1	LS
CARB-843	1.16	-6.05		69	F1	LS
CARB-844	0.47	-6.49		70	F1	LS
CARB-845	0.30	-6.39		71	F1	LS
CARB-846	0.63	-6.85		72	F1	LS
CARB-847	0.23	-6.78		73	F1	LS
CARB-848	0.45	-6.63		74	F1	LS
CARB-849	0.79	-6.69		75	F1	LS
CARB-850	1.32	-6.73		76	F1	LS
CARB-851	0.53	-6.55		77	F1	LS
CARB-852	0.51	-6.27		78	F1	LS
CARB-853	0.84	-5.93		79	F1	LS
CARB-854	0.78	-5.75		80	F1	LS
CARB-855	1.00	-6.40		81	F1	LS
CARB-856	0.72	-6.34		82	F1	LS
CARB-857	0.33	-6.11		83	F1	LS
CARB-858	1.01	-5.76		84	F1	LS
CARB-859	1.08	-5.14		85	F1	LS
CARB-860	1.12	-6.00		86	F1	LS
CARB-861	0.53	-6.47		87	F1	LS
CARB-862	1.05	-5.31		88	F1	LS
CARB-863	1.04	-5.27		89	F1	LS
CARB-864	0.73	-4.83		90	F1	LS
CARB-865	0.82	-1.57		91	F1	LS
CARB-866-A	-2.04	-2.90		92	F7	MS
CARB-867	-3.41	-3.37		93	F7	MS
CARB-868	0.51	-1.96		94	F7	MS
CARB-869	-1.37	-2.54		95	F7	MS
CARB-871	1.08	-1.58		97	F7	MS
CARB-872	-0.23	-2.61		98	F7	MS
CARB-873	0.94	-2.12		99	F7	MS
CARB-874	1.25	-1.91		100	F7	MS
CARB-875	0.26	-5.62		101	F7	MS
CARB-876	0.96	-2.25		102	F7	MS
CARB-877	-1.36	-3.55		103	F7	MS
CARB-878	0.28	-2.49		104	F7	MS
CARB-879	-0.25	-2.64		105	F7	MS
CARB-880	-0.79	-2.69		106	F7	MS
CARB-881	0.36	-1.02	29.81	107	F7	MS
CARB-882	1.38	-1.45	29.37	108	F7	MS
CARB-883	-0.27	-2.85	27.92	109	F7	MS
CARB-884	1.87	-1.05	29.78	110	F7	MS

Amostra	$\delta^{13}\text{C}\text{\%}$	$\delta^{18}\text{O}\text{\%}$ VPDB	$\delta^{18}\text{O}\text{\%}$ SMOW	Posição na coluna	Fácies	Section
CARB-885	1.02	-2.30	28.49	111	F7	MS
CARB-886	0.86	-2.58	28.20	112	F7	MS
CARB-887	2.35	-0.57	30.27	113	F7	MS
CARB-888	0.43	-1.09	29.73	114	F7	MS
CARB-889	0.06	-2.67	28.11	115	F7	MS
CARB-890	-0.33	-3.88	26.86	116	F7	MS
CARB-891	2.96	-0.53	30.31	117	F7	MS
CARB-892	-0.01	-2.02	28.78	118	F7	MS
CARB-893	0.78	-1.36	29.46	119	F7	MS
CARB-894	2.42	-1.55	29.26	120	F7	MS
CARB-895	1.36	-1.23	29.59	121	F7	MS
CARB-896	-0.86	-1.67	29.14	122	F7	MS
CARB-897	-1.01	-3.35	27.41	123	F7	MS
CARB-898	2.31	-2.56	28.22	124	F7	MS
CARB-899	2.87	-0.72	30.12	125	F7	MS
CARB-900	2.08	-3.24	27.52	126	F7	MS
CARB-901	2.57	-1.53	29.29	127	F7	MS
CARB-902	2.22	-1.78	29.02	128	F7	MS
CARB-903	1.81	-2.17	28.62	129	F7	MS
CARB-904	2.53	-2.35	28.44	130	F7	MS

ANEXO B – Dados de C e O dos plugs

Amostra	Carbonato			Posição (m)	feição
	V-PDB	V-PDB	V-SMOW		
	$\delta^{13}\text{C}\text{\%}$	$\delta^{18}\text{O}\text{\%}$ VPDB	$\delta^{18}\text{O}\text{\%}$		
CARB-0035-A	0.44	-4.01	26.72	126	host rock
CARB-0035-B	0.80	-2.34	28.44	126.00	host rock
CARB-0036-A	-0.47	-3.78	26.96	127.00	host rock
CARB-0036-B	0.13	-8.17	22.44	127	host rock
CARB-0037-A	-0.27	-6.52	24.14	129.50	host rock
CARB-0037-B	-2.51	-9.02	21.56	129.5	vein/fill
CARB-0038-X	0.72	-4.30	26.43	121.00	host rock
CARB-0039-A	2.64	-3.74	27.01	150.00	host rock
CARB-0039-B	2.47	-3.33	27.42	150	host rock
CARB-0040-A	1.99	-3.17	27.59	150.20	host rock
CARB-0040-B	-5.52	-8.58	22.02	150.20	vein/fill
CARB-0040-C	0.37	-5.58	25.11	150.20	vein/fill
CARB-0041-X	3.55	-3.68	27.06	156	host rock
CARB-0042-X	3.39	-2.69	28.09	155.5	host rock
CARB-0043-X	3.55	-3.68	27.07	160.00	host rock
CARB-0044-A	3.76	-4.01	26.73	152	host rock
CARB-0044-B	1.69	-5.21	25.49	152	vein/fill
CARB-0045-A	0.46	-1.75	29.06	130	host rock
CARB-0045-B	0.66	-2.71	28.06	130	host rock
CARB-0046-A	2.28	-3.28	27.48	151.5	host rock
CARB-0046-B	-8.68	-7.68	22.94	151.5	vein/fill
CARB-0046-C	-8.14	-7.75	22.87	151.5	vein/fill
CARB-0047-A	-4.41	-7.59	23.04	151	vein/fill
CARB-0047-B	1.48	-3.67	27.08	151	host rock
CARB-0048-A	2.28	-2.86	27.91	150.7	host rock
CARB-0048-B	-0.43	-4.43	26.30	150.7	vein/fill
CARB-0049-X	-0.41	-11.89	18.60	158.5	host rock
CARB-0050-X	8.98	-6.83	23.82	167.5	host rock
CARB-0051-X	6.62	-4.01	26.72	165.5	host rock
CARB-0052-A	-6.70	-7.22	23.41	183	vein/fill
CARB-0052-B	8.53	-6.10	24.57	183	host rock
CARB-0052-C	2.73	-7.06	23.58	183	vein/fill
CARB-0053-A	-3.43	-7.68	22.94	182	vein/fill
CARB-0053-B	8.96	-6.15	24.52	182	host rock
CARB-0054-A	9.31	-5.48	25.21	184	host rock
CARB-0054-B	-4.46	-8.10	22.51	184	vein/fill
CARB-0055-X	8.69	-6.30	24.37	186	host rock
CARB-0056-A	9.19	-4.64	26.08	197	host rock
CARB-0056-B	10.28	-4.69	26.02	197	host rock

Amostra	Carbonato				Posição (m)	feição
	V-PDB	V-PDB	V-SMOW			
	$\delta^{13}\text{C}\text{\%}$	$\delta^{18}\text{O}\text{\%}$ VPDB	$\delta^{18}\text{O}\text{\%}$ SMOW			
CARB-0057-A	9.27	-5.28	25.42	203	host rock	
CARB-0057-B	-1.71	-6.17	24.50	203	vein/fill	
CARB-0058-A	9.22	-6.70	23.95	220	host rock	
CARB-0058-B	-0.49	-6.77	23.88	220	vein/fill	
CARB-0059-X	2.50	-2.97	27.80	149	host rock	
CARB-0060-A	1.72	-3.29	27.47	150.5	host rock	
CARB-0060-B	1.29	-3.74	27.00	150.50	vein/fill	
CARB-0061-A	-9.08	-3.87	26.88	159	carste	
CARB-0061-B	-9.41	-2.61	28.17	159.00	carste	
CARB-0062-A	10.37	-6.30	24.36	159.2	host rock	
CARB-0062-B	6.42	-5.06	25.64	159.2	host rock	
CARB-0063-A	3.67	-5.33	25.37	158.00	host rock	
CARB-0063-B	0.84	-8.26	22.34	158.00	host rock	
CARB-0064-A	2.20	-5.13	25.57	150.00	host rock	
CARB-0064-B	-9.39	-9.13	21.45	150.00	vein/fill	
CARB-0065-A	3.90	-4.73	25.99	150.20	host rock	
CARB-0065-B	-6.38	-8.57	22.02	150.20	vein/fill	
CARB-0066-A	-6.61	-6.25	24.42	150.50	vein/fill	
CARB-0066-B	-3.24	-8.88	21.70	150.5	vein/fill	
CARB-0066-C	2.95	-3.60	27.15	150.50	host rock	
CARB-0067-A	-8.89	-9.29	21.29	150.00	vein/fill	
CARB-0067-B	-4.84	-8.64	21.95	150.00	vein/fill	
CARB-0067-C	2.30	-5.28	25.42	150.00	host rock	
CARB-0068-A	6.57	-6.99	23.65	241.00	host rock	
CARB-0068-B	8.11	-5.98	24.69	241.00	vein/fill	
CARB-0069-A	11.74	-6.00	24.68	242.00	host rock	
CARB-0069-B	9.85	-4.71	26.00	242.00	host rock	
CARB-0069-C	10.37	-7.46	23.16	242.00	vein/fill	
CARB-0070-A	9.56	-5.65	25.04	245.00	vein/fill	
CARB-0070-B	11.25	-4.79	25.92	245.00	host rock	
CARB-0070-C	10.83	-5.83	24.86	245.00	host rock	
CARB-0070-D	7.99	-6.72	23.93	245.00	vein/fill	
CARB-0071-A	9.98	-6.15	24.52	246.00	host rock	
CARB-0071-B	11.61	-4.78	25.93	246.00	host rock	
CARB-0071-C	9.32	-6.67	23.99	246.00	vein/fill	
CARB-0072-A	11.67	-5.51	25.18	246.50	host rock	
CARB-0072-B	4.48	-4.34	26.39	246.50	vein/fill	
CARB-0073-A	9.89	-5.62	25.07	247.00	host rock	
CARB-0073-B	-2.81	-6.62	24.03	247.00	vein/fill	

Amostra	Carbonato			Posição (m)	feição
	V-PDB	V-PDB	V-SMOW		
	$\delta^{13}\text{C}\text{\%}$	$\delta^{18}\text{O}\text{\%}$ VPDB	$\delta^{18}\text{O}\text{\%}$ SMOW		
CARB-0074-A	9.83	-4.06	26.67	251.00	host rock
CARB-0074-B	8.31	-4.69	26.03	251.00	host rock
CARB-0075-A	4.15	-2.97	27.80	158.00	host rock
CARB-0075-B	2.19	-4.82	25.89	158.00	host rock
CARB-0076-A	1.07	-3.32	27.44	142.00	host rock
CARB-0076-B	0.08	-9.28	21.29	142.00	vein/fill
CARB-0077-A	0.90	-1.83	28.98	121.00	host rock
CARB-0077-B	-0.23	-5.47	25.22	121.00	vein/fill
CARB-0074-A	9.83	-4.06	26.67	251.00	host rock
CARB-0074-B	8.31	-4.69	26.03	251.00	host rock
CARB-0075-A	4.15	-2.97	27.80	158.00	host rock
CARB-0075-B	2.19	-4.82	25.89	158.00	host rock
CARB-0076-A	1.07	-3.32	27.44	142.00	host rock
CARB-0076-B	0.08	-9.28	21.29	142.00	vein/fill
CARB-0077-A	0.90	-1.83	28.98	121.00	host rock
CARB-0077-B	-0.23	-5.47	25.22	121.00	vein/fill
CARB-0074-A	9.83	-4.06	26.67	251.00	host rock
CARB-0074-B	8.31	-4.69	26.03	251.00	host rock
CARB-0075-A	4.15	-2.97	27.80	158.00	host rock